

**Generation and Efficient Measurement of Single Photons
Using Superconducting Circuits**

by

W. F. Kindel

B.S., The Ohio State University, 2007

M.S., University of Colorado at Boulder, 2012

A thesis submitted to the
Faculty of the Graduate School of the
University of Colorado in partial fulfillment
of the requirements for the degree of
Doctor of Philosophy
Department of Physics

2015

This thesis entitled:
Generation and Efficient Measurement of Single Photons Using Superconducting Circuits
written by W. F. Kindel
has been approved for the Department of Physics

Konrad W. Lehnert

Prof. Murray Holland

Date _____

The final copy of this thesis has been examined by the signatories, and we find that both the content and the form meet acceptable presentation standards of scholarly work in the above mentioned discipline.

Kindel, W. F. (Ph.D., Physics)

Generation and Efficient Measurement of Single Photons Using Superconducting Circuits

Thesis directed by Prof. Konrad W. Lehnert

In this thesis, I demonstrate and evaluate an on-demand source of single propagating microwave photons. Working in the context of a quantum network, nodes are connected via propagating, nonclassical states of the electromagnetic field. As such, preparing and detecting propagating quantum states is an essential task. I work with one particular node consisting of a microfabricated, effective two level system coupled to a microwave resonator and study its ability to produce propagating nonclassical states, such as single photon states. In principle, states generated by this node could be sent to other such nodes. However, I send them into a Josephson parametric amplifier (JPA) to characterize the source.

In particular, I discuss how to design and couple the two components that form my source: a fixed frequency transmon qubit and a 3D superconducting waveguide cavity. I demonstrate the ability to control of the dynamics of this combined system and implement a single photon generation protocol, which utilizes a single microwave control field that is far detuned from the photon emission frequency. To characterize the generation, I perform tomography on the propagating photon state to determine its density matrix ρ . I perform repeated JPA-backed, linear measurements of the propagating state. Based on the histograms of my measurements, I infer a maximum single photon component $\rho_{11} = 0.36 \pm 0.01$. I characterize the imperfections of the photon generation and detection, including detection inefficiency and measurement backaction. I find that within uncertainty my measurements match my expectation.

Dedication

In memory of Ethan Townsend.

Acknowledgements

I would like to thank everyone who has helped, supported, advised, and learned alongside me throughout my time at the University of Colorado. To credit properly would take far too many pages than is allotted here, so can only highlight a few of the many acknowledgments due. I will start by thanking the two people who have worked directly with me the most: Hsiang-Sheng Ku and Michael Schroer. I started my first project with Hsiang-Sheng Ku. I thank him for his thoughtful questions and insights as we tried to understand quantum mechanics of the field, and all of his efforts completing that experiment. For my second project, this thesis work, I owe a great debt to Michael Schroer. His knowledge of hardware, software, physics, and his constant drive to make progress laid the groundwork for my photon measurements. It was a great pleasure working alongside both of you.

I would like that my advisor Konrad Lehnert. He gave me the opportunity complete this project while providing key insights into the physics of the experiment. He has supported the directions I wanted to take my research and has taken to time to teach me not just about the science, but also about how to communicate and work as a scientist. He has taken his role as a mentor seriously, to the benefit of myself and all his students and researchers. Thank you, Konrad.

Next, I would like to thank all of those whom I have worked with in the Lehnert Lab creating a productive, and yet at times silly, working environment. I thank all the current group members: Pete Burns, Ben Chapman, Xizheng Ma, Tim Menke, Dan Palken, Adam Reed, Eric Rosenthal, Lucas Sletten, Andrew Higginbotham, Maxime Malnou, Bad Moores, Jeremie Viennot and Juan Montoya– nearly all of whom help me edit this document in some capacity– and former members

who have worked by my side: Jennifer Harlow, Francois Mallet, Reed Andrews, Joe Kerckhoff, Gerwin Koolstra, Brad Mitchell, and Tauno Palomaki. I would like to thank Jennifer Harlow and Francois Mallet for teaching me about microwaves when I first stated. Jennifer, Adam Reed and Tauno Palomaki for the years together in lab and outside of lab exploring Colorado. Reed Andrews, as they say, it has been one heck of a ride. Ben Chapman, you are relatively new in lab, but you have championed the conquest of the JILA Cup. I trust it will not be lost under your tenure. Jeremie Viennot and Xizheng Ma, it has been fun playing with qubits in lab and learning the *ropes* of climbing outside. As for the rest of you, a thanks is due. Working with all of you, you have helped me with day to day problems and collective are truly the reasons I have made progress.

I would like to thank those who have supported me during my time in Boulder, of which there are far too many to name. And of course, thank you to my family for supporting me and putting up with me over these Boulder years.

Contents

Chapter	
1	Introduction 1
1.1	Thesis overview 3
1.2	Experiment overview 4
1.2.1	Photon source 4
1.2.2	Photon detection 5
1.3	Other single photon generation protocols 6
1.3.1	Photon like coherent states 6
1.3.2	Purcell limited decay 6
1.3.3	Frequency tunable qubits 7
1.3.4	Higher order transitions 8
2	Quantum mechanics of photon generation and measurement 9
2.1	Circuits as harmonic oscillators 9
2.1.1	Transmission line decay 10
2.1.2	Quadratures 11
2.1.3	States of the field 13
2.2	A two level system coupled to a cavity: CQED 15
2.2.1	Hamiltonian 15
2.2.2	Dispersive limit 16

2.2.3	System dynamics	17
2.3	Measuring a quantum state	21
2.3.1	Parametric amplifier measurements	21
2.3.2	Wigner function	23
2.3.3	Homodyne measurement of quantum states	25
2.3.4	Heterodyne measurement of quantum states	25
2.3.5	Inefficient measurement	27
3	Qubit and cavity design	30
3.1	The qubit	30
3.1.1	From linear to non-linear circuits	31
3.1.2	Cooper pair box	32
3.1.3	CPB dynamics in phase basis	36
3.1.4	CPB solutions in phase basis	37
3.1.5	Transmon qubit limit of the CPB	39
3.1.6	Transmon qubit design constraints	41
3.1.7	Qubit fabrication	43
3.2	Cavity	45
3.2.1	Idealized cavity modes	45
3.2.2	HFSS calculation of cavity modes	48
3.2.3	Cavity fabrication	48
3.2.4	Cavity input and output coupling	48
3.3	Coupled system	51
3.3.1	Effective dispersive Hamiltonian	53
3.3.2	Dipole coupling model	53
4	Qubit and cavity's characterization and dynamics	56
4.1	Cavity spectroscopy and qubit readout	56

4.1.1	Qubit readout	59
4.1.2	Two-tone spectroscopy of the qubit	60
4.1.3	Single shot readout	64
4.2	Control pulses	66
4.2.1	Qubit pulse	66
4.2.2	Blue sideband pulse	69
4.3	Qubit characterization	72
4.3.1	Qubit lifetime	72
4.3.2	Qubit dephasing	74
5	Photon generation and detection	78
5.1	Photon generation	79
5.1.1	Blue sideband measurements	79
5.1.2	Cavity photon detection with qubit	81
5.2	Heterodyne detection	84
5.2.1	Two quadrature filter and photon variance	85
5.2.2	Comparison to qubit state	88
5.2.3	Density matrix reconstruction	90
5.3	Optimized photon generation and homodyne detection	96
5.3.1	Protocol	97
5.3.2	Homodyne detection and tomography	100
5.3.3	Characterizing photon generation and efficient homodyne detection	108
6	Conclusions and outlook	115
6.1	Outlook	116

Bibliography	118
---------------------	-----

Appendix

A Description of photon generation and homodyne detection apparatus	124
--	-----

Tables

Table

Figures

Figure

2.1	The Wigner function for a single photon state ($n = 1$).	24
2.2	Homodyne measurement of a single photon: single quadrature probability distribution for the $n = 1$ Fock state.	26
2.3	Heterodyne measurement of a single photon: two quadrature probability distribution for the $n = 1$ Fock state.	28
3.1	The circuit schematic of a Cooper pair box (CPB).	33
3.2	The energy levels of the CPB in the large charging energy E_c limit ($E_J/E_c = 0.2$).	35
3.3	The energy levels of the CPB where $E_J = E_c$	39
3.4	The energy levels of the CPB in the transmon limit ($E_J/E_c = 50$).	40
3.5	The circuit schematic of a transmon qubit.	42
3.6	The center shows a 500 by 200 nm Josephson junction where two Aluminum layers overlap.	44
3.7	An image of the cavity used in the experiment.	46
3.8	The TE_{011} mode of a cavity.	48
3.9	Results from an HFSS calculation of the coupling rate for various pin lengths.	50
3.10	The reflection response and fit used in setting the coupling rate κ_1 of the cavity.	52
3.11	The qubit coupled to the cavity by placing it at the center of the cavity.	52
4.1	Transmission spectroscopy schematic.	57

4.2	The power dependent cavity spectra.	58
4.3	Two-tone spectroscopy schematic.	61
4.4	Two-tone spectroscopy on the state of the qubit.	63
4.5	Histograms of the measured readout tone's voltage (y-axis) at various readout tone powers (x-axis).	65
4.6	The results from the Rabi measurement adjusting pulse amplitude and frequency.	68
4.7	The results of the blue sideband measurement, as a function of pulse amplitude and frequency.	70
4.8	The results from the blue sideband measurement with fixed pulse amplitude.	71
4.9	Measurement of the qubit $ e\rangle$ state lifetime.	73
4.10	Ramsey measurement of the qubit dephasing as I adjust the pulse frequency.	75
4.11	Ramsey measurement of the qubit dephasing with the drive detuned 1 MHz.	76
5.1	Energy level schematic for photon generation with the blue sideband.	80
5.2	Excited state probability during a blue sideband drive (marks) fit to a offset exponentially decaying sinusoid (solid line).	82
5.3	Detecting cavity photons created by a blue sideband π -pulse using photon number dependent qubit π -pulses.	83
5.4	The two heterodyne filter functions $f_1(t)$ (red) and $f_2(t)$ (blue) along with their temporal profile $\sqrt{f_1^2(t) + f_2^2(t)}$ (black dotted line)	87
5.5	Measurement of $\text{var}(X_i)$ (above) and P_e (below) in response the a blue sideband pulse drive as the frequency and duration of the pulse is adjusted.	89
5.6	Histograms of two quadrature measurement of the photon state (top) and the vacuum state (bottom) plotted as the Q-function (probability density).	92
5.7	A line cut through the center of the measured single probability density (markers) with the best fit to density matrix elements (solid line).	94

5.8	Reconstructed density matrix elements $ \rho_{ij} $ of the measured photon state using heterodyne detection.	95
5.9	Simplified schematic for photon generation.	97
5.10	Energy level diagram for photon generation and calibration.	98
5.11	Timing diagram for the experiment.	99
5.12	Histogram of a quadrature measurement set of single photons (narrow blue bars) and the no-photon control (wide green bars) with the JPA gain at 29 dB.	103
5.13	Quantifying backaction.	105
5.14	Diagonal density matrix elements determined from fitting the quadrature histogram over a range of JPA gains from 17 dB to 33 dB.	107
5.15	The values of $g_2(0)$ computed from the density matrix elements.	109
5.16	Thermal sweep data for the JPA operated at 20 (green squares), 25 (blue circles) and 30 dB (red crosses) gains.	111
5.17	The measurement efficiency η_m is determined from a thermal sweep at three JPA gains (circles).	112
5.18	The fidelity of the measured density matrix with respect to: an ideal single photon (blue squares), and the density matrix I expect to measure given pure photon generation in the cavity (black points).	114
A.1	The microwave schematic for the experiment.	125

Chapter 1

Introduction

In this thesis, I address a quantum node, or building block in the framework of a quantum network. Specifically, I look at how these nodes transmit information. Many physical platforms exist for building nodes of a quantum network, from trapped ions [1, 2] to Nitrogen vacancy centers [3] and electron spins [4, 5]. In this chapter, I describe my experimental platform for realizing a quantum node, which is a particular type of superconducting circuit, and introduce the concept of a quantum network. Then, I provide an overview of the entire thesis. Lastly, I describe my experimental approach to address this problem and compare mine to other approaches with superconducting circuits.

With the advent of superconducting circuits used as quantum technologies, the prospect of processing quantum information has become less remote. In particular, the circuit quantum electrodynamics (CQED) concept has seen many recent successes. This architecture consists of a superconducting qubit strongly coupled to a cavity [6, 7]. The cavity is an electromagnetic resonator, which, in the absence of coupling to the qubit, acts as a harmonic oscillator. Experimentally, one can drive this cavity and the average number of photons increase linearly with drive power. Although the qubit can also be considered an electromagnetic oscillator, it behaves intrinsically differently than the cavity. When driven, its response is highly nonlinear. It can only absorb one unit of energy, or quanta. As its state can only be measured in two different values, it is a two-level system. This gives rise to two powerful properties. First, because it has only two possible states, it can be used to encode a bit of information. Furthermore, because it behaves quantum mechani-

cally, it can be prepared in a quantum superposition of these two states, and thus is referred to as a quantum bit (qubit) [8]. Second, its nonlinear response to an electromagnetic field drive can be used as a resource to prepare and readout nonclassical states of the cavity field (states of microwave light that go beyond a classical description). For example, the cavity has been prepared in states of quantum coherent superpositions of photon, with detectible interferences [9]. Moreover, quantum coherent superpositions of the classical coherent state have been prepared, called Schrodinger cat states in a nod to Schrodinger's notorious cat [10].

Together, these qubit-cavity systems can be viewed as a building block. In a broader context, one can think of a quantum network where qubit-cavity systems are nodes that perform elementary operations [11]. In order to have these nodes working together to process quantum information, one has to couple them coherently. In other words, one must have channels connecting the nodes to propagate quantum information among them. In a local approach, physically separated qubits communicate via a cavity bus [12]. Using this bus, the states of the two qubits can be tied together in what is known as entanglement. Harnessing this entanglement between two physically separated qubits, the quantum state of one qubit is destroyed and recreated in the second qubit without measurement, in a process known as quantum teleportation [13]. In the approach I consider, the communication channel takes the form of a transmission line along which electromagnetic waves can propagate. This approach allows for arbitrary connectivity among quantum modules such as QCED systems. Commutation among these nodes via propagating modes along transmission lines can entangle the nodes, forming a larger quantum system or quantum network [14].

In addition to their utility in establishing quantum networks, propagating non-classical states can be an interesting resource in various other contexts. In particular, in the field of quantum micro-mechanics, a current challenge is to prepare profoundly nonclassical states of motion, such a single phonon states or Schrodinger cat states. Mechanical systems can be coupled strongly to propagating microwave modes, enabling their preparation in coherent states [15, 16]. But by themselves, they lack sufficient intrinsic nonlinearity to evolve spontaneously into a profoundly nonclassical state. One path is to prepare a profoundly nonclassical propagating microwave field and transfer that

state to a mechanical oscillator.

Given the importance of these propagating modes in forming a quantum network and in creating non-classical states of motion, I focus on generating one of the simplest nonclassical states: a single photon. The core of this thesis studies how a single photon can be created in the cavity using the qubit, how this photon's wavefunction can slowly move out of the cavity and into the transmission line, and how I can detect this photon.

In the optical domain, photon detectors are available and routinely used to detect single photons. These detectors register the presence or absence of a photon with a binary output signal; i.e., they click as one photon is measured. At microwave frequencies, such detectors are not available because the energy carried by a single photon is too small to create an electron-hole pair in a semiconductor. What is available are voltage amplifiers or linear detectors. Due to the small power of these single photon signals, stringent noise requirements are placed on these detectors. Meeting these requirements is impossible with commercially available amplifiers. I therefore use a home-made amplifier that achieves near-quantum limited amplification¹. This amplifier is a parametric amplifier called the Josephson Parametric Amplifier (JPA).

1.1 Thesis overview

I begin by introducing the concept of photon generation and detection experiment within a modular architecture of a quantum network. In doing so, I introduce the two key elements of the experiment: the qubit-cavity system, which generates single propagating photons, and the JPA, which acts as a detector. I specifically discuss the concept of photon generation and detection and contrast my work with other photon generation experiments in superconducting circuits. In Chapter 2, I introduce a quantum mechanical formalism for circuits, including models for CQED system and their dynamics, and the quantum mechanics of measurement. In Chapter 3, I discuss designing a qubit-cavity system within the constraints of the photon generation demands. In Chapter 4 I experimentally characterize the qubit-cavity system and demonstrate its basic operations. In

¹ The added noise is close to what is required by quantum mechanics [17]

Chapter 5, I describe single photon generation and detection. Finally, in Chapter 6 I discuss extending my generation from single photons to flying qubits, and discuss integrating the photon generation with other quantum modules, such as mechanical systems.

1.2 Experiment overview

1.2.1 Photon source

In designing the photon source, I consider parameters such as the itinerant photon's frequency and bandwidth to ensure compatibility with the target module. So that I am not limited by qubit lifetimes, I choose to make the source module from most coherent, yet fixed frequency qubits. These systems consist of a transmon qubit embedded in the center of a superconducting cavity [18]. These so called 3D transmons are both simple to fabricate and have lifetimes ($T_1 \approx 100 \mu\text{s}$) compatible with narrowband modules such as: electromechanical devices [16, 19], microwave to optical convertors [20], and other 3D transmon systems; i.e., bandwidths (inverse lifetimes) that do not exceed 1 MHz. However, in this style of CQED system that I use, neither the qubit nor the cavity have tunable resonance frequencies; thus, the only controls available are microwave fields.

Because I am limited to control fields, I am interested in a single transition that creates a photon in the cavity. In CQED systems, the qubit or two level system breaks the harmonicity of transitions, and thereby allows deterministic photon generation protocols to be implemented by driving these transition [21]. The transition I am interest in is known as a blue sideband transition (Section 2.2.3.2). This transition can be used to generate a single photon while exciting the qubit. It is a two photon process, roughly at the average of the qubit and cavity frequency $\omega_{\text{blue}} \approx (\omega_c + \omega_q)/2$. Hence, this transition is off resonance with both the qubit and the cavity.

Experimentally, blue sideband pulses have been utilized in CQED systems, demonstrating their ability to generate cavity excitations or photons. The blue sideband transitions were initially spectroscopically studied in these QCED system [22]. Generating cavity excitations (photons) was indirectly demonstrated through an experiment that entangled two qubits [23]. In Ref. [23]'s

experiment, the blue sideband creates a photon as an intermediate step while entangling the two qubits. By verifying the entanglement between the two qubits indirectly, this work shows that blue sideband pulses can create photons in QCED systems.

Given the experimental demonstrations of the blue sideband pulse and long coherence times of QCED systems, I combine these two elements to form an elementary protocol for generating itinerant photons. First, I use a control field at the blue sideband transitions to generate a single photon in the cavity. Then, the photon in the cavity decays through a strongly coupled output port, creating the propagating photon.

1.2.2 Photon detection

Rather than using a second CQED module as the target, I use a quantum module which acts as a detector of the propagating photon: namely, the JPA. This quantum module performs a reversible and deterministic transformation on the propagating mode, amplifying one quadrature and deamplifying, or squeezing, the orthogonal quadrature [24, 25]. I choose the JPA because Josephson junction based parametric amplifiers (like the JPA) are among the most efficient microwave amplifiers and have been successfully integrated with QCED systems. Their development has enabled 30 fold efficiency improvements over the best commercial low noise amplifiers (HEMTs) because JPAs add only a small fraction of vacuum fluctuations on top of amplified signals [17]. JPAs are the natural choice for measuring the propagating, single photon state because they have been used to perform efficient measurement of propagating nonclassical states [26, 27, 28, 29]. Moreover, similar Josephson junction based parametric amplifiers have already been integrated with qubit-cavity systems to perform qubit readout [30, 31, 32, 33]. In these systems, the parametric amplifiers have improved qubit detection to nearly ideal quantum non-demolition (QND) [34]. Simultaneously demonstrating high efficiency and compatibility with CQED modules, they have been used to measure multiple quantum trajectories of a qubit [35].

A JPA is a nonlinear LC resonator that can act as an amplifier when pumped with strong rf power. The pump can either be at a single frequency that defines the center of the JPA band,

or it can consist of two tones where the average of the two defines the center of the JPA band. Additionally, JPAs can be operated in one of two modes (Section 2.3.1). In one mode, heterodyne mode, the JPA amplifies a tone regardless of the tone's phase. In the second mode, homodyne mode, the JPA is phase sensitive. The JPA amplifies one quadrature of signal that is in phase with a reference. For technical reasons, when I use the JPA as a homodyne detector, I double pump, and when I use the JPA as a heterodyne detector, I use one pump tone. To operate the JPA as a homodyne detector, the center of the JPA's band must be centered on the band of signal. In this case, I double pump the JPA because I do not want the strong pump to resonate with the cavity which defines the photon frequency. To operate the JPA as a heterodyne detector, the signal band is detuned from the center of the JPA's band. Because the single pump is already detuned, I use a single pump.

1.3 Other single photon generation protocols

1.3.1 Photon like coherent states

As a stepping stone to nonclassical communication between modules, communication between CQED modules has been studied using classically described coherent states. In Yin and Wenner's experiments [36, 37], the coupling between the cavity and the transition line is controlled dynamically. By adjusting the coupling, a propagating coherent state with an average photon number $\bar{n} = 1$ is captured in the cavity of a CQED module. The captured photon can be released and sent to another module. Though this work utilizes classical states, it demonstrates that CQED modules are capable of catching and releasing states whose energy is the same as nonclassical states such as single photon states.

1.3.2 Purcell limited decay

Initial work on photon generation using superconducting qubits by Houck [38] relied on coupling the qubit directly to an output mode. In this simple protocol, a pulse at the qubit frequency

excites the qubit. The qubit then decays through the output port creating a propagating photon at the qubit frequency. In this method, the pulse is at the same frequency as the photon and couples to the output mode. As a result, the photon and the pulse are neither spectrally or temporally isolated during the pulse. Therefore, the single photon cannot be completely distinguished from the control field, partially spoiling the single photon character of the generated state. Furthermore, because the pulse is at the same frequency as the photon, the large control pulse may also excite the target module.

Similar to Houck, my protocol for generating photons is simple in that it relies on a single calibrated control pulse. But, because I use a blue sideband pulse, the control field is detuned from the single photon. The photon is emitted at the cavity's resonance frequency ω_c , whereas the control pulse is approximately at the average between cavity and qubit $(\omega_q + \omega_c)/2$, giving the photon spectral isolation.

1.3.3 Frequency tunable qubits

There are several demonstrations of photon generation with qubit-cavity systems that do not use control fields, but rather rely on frequency tunable qubits [39, 36]. When the qubit is tuned to the cavity frequency, excitations oscillate between the the qubit and cavity [40, 6]. By controlling the interval that the two are on resonance, then excitation can be swapped from the qubit into the cavity. Thus, by preparing the qubit in the excited state with a qubit pulse, and then tuning the qubit to swap the excitation into the cavity, a single photon is created in the cavity. By strongly coupling the cavity to an output mode, a propagating photon is created. In one particular example, Eichler [39] generated propagating arbitrary superpositions of zero and one photon $\Psi = A|0\rangle + B|1\rangle$, which can be thought of as a propagating or flying qubit.

However, in the type of qubit-cavity system that I adopt and is discussed in Ref. [18], the qubit is not easily tunable. To create a more coherent qubit, this style of qubit-cavity system places the qubit in the center of a superconducting cavity making it difficult to apply the magnetic flux used to tune qubits because the superconducting cavity shields magnetic fields. Therefore,

protocols relying on frequency tunable qubits cannot be easily implemented.

My work is further distinguished by its detection. In Eichler's work [39], the photon generation protocol was repeated billions of times to overcome the inefficient HEMT measurements in order tomographically reconstruct to an inference of generated state. In my approach, I use an efficient JPA to measure the photon state. I perform the tomography on the measured state, without artificially removing the added noise of the measurement.

1.3.4 Higher order transitions

More recently, Pechal [41] has demonstrated photon generation using only control fields detuned from the photon. Thus, this protocol is compatible with 3D transmons. It used multiple transitions including higher level states of the qubit making it more complicated than my single pulse protocol. Pechal also removes the added noise from inefficient measurements, rather than implementing an efficient measurement of the photon state.

Chapter 2

Quantum mechanics of photon generation and measurement

To establish a mathematical language and a consistent notation with which to describe photon generation and detection experiments, I review a portion of the quantum optics formalism. Because I am interested in generating and measuring states of cavities (resonators) and transmission lines, I begin by discussing the quantum mechanics of these modes, which are harmonic oscillators. Then, I look at examples of common classical and nonclassical states of these modes. Next, I cover a simple quantum mechanical model for a qubit coupled to cavity, and discuss a method for photon generation in an ideal limit. Lastly, I cover the framework for representing and measuring these quantum states. I discuss both how to operate the JPA to measure states, and how to calculate the expected probability distribution of these measurements for particular quantum states.

2.1 Circuits as harmonic oscillators

Modes of cavities, resonators and transmission lines behave as harmonic oscillators. To understand these modes and the states of these modes, I start by writing the Hamiltonian of a harmonic oscillator

$$H_{\text{ho}} = \omega(a^\dagger a + 1/2) \tag{2.1}$$

in terms of the unitless raising a^\dagger and lowering a ladder operators. Here and for the rest of the document, I have omitted the \hbar 's. It is therefore understood that angular frequencies must be multiplied by \hbar to recover units of energy. The energy eigenstates called Fock states, or photon states, I label as $|0\rangle, |1\rangle, \dots |n\rangle$. These eigenstate have energy $\langle H_{\text{ho}} \rangle = \omega(n + 1/2)$ and thus form

a harmonic spectrum. The creation ladder operator a^\dagger acting on eigenstate state $|n\rangle$ results in

$$a^\dagger |n\rangle = \sqrt{n+1} |n+1\rangle. \quad (2.2)$$

Thus, some combinations of these ladder operators acting on the ground state, the vacuum state $|0\rangle$, can generate any pure quantum state. For a more detailed description of mode quantization, consult a Quantum Optics text book such as Gerry and Knight's [42].

2.1.1 Transmission line decay

In this experiment, I am interested in measuring states propagating down transmission lines that are generated by the cavity. Specifically, I want to think about: what propagating mode does that cavity evolve into. To understand this, I consider how incoming and outward propagating states of the transmission line relate to the internal state of the cavity. Because I can represent pure quantum states with combinations of ladder operators acting on the vacuum state, I consider how operators of the cavity a relate to operators of incoming and outward propagating states a_{in} and a_{out} , respectively. Considering a cavity coupled to a transmission line with power decay rate κ , these relations are:

$$\dot{a} = -\frac{\kappa}{2}a + \sqrt{\kappa}a_{in} \quad (2.3)$$

$$a_{out} = \sqrt{\kappa}a - a_{in} \quad (2.4)$$

according to input/output formalism [43]. Consequently, to find the cavity's output at all times, I must solve Eqn. 2.3:

$$a(t) = a(0)e^{-\frac{\kappa}{2}t} + \sqrt{\kappa}e^{-\frac{\kappa}{2}t} \int_0^t e^{-\frac{\kappa}{2}z} a_{in}(z) dz. \quad (2.5)$$

I am not interested in a continuum of output modes, but a single mode propagating down the transmission line. Therefore, I define a particular output mode by considering the temporal profile of excitations decaying out of the cavity. Because amplitude decays out of the cavity at a rate $\kappa/2$, I define the temporal profile as

$$f_{out}(t) = \sqrt{\kappa}e^{-\frac{\kappa t}{2}} \Theta(t) \quad (2.6)$$

in terms of the Heaviside step function $\Theta(t)$. With $f_{out}(t)$, I define the output mode as

$$A_{out} = \int f_{out}(t)a_{out}(t)dt = \int_0^\infty \sqrt{\kappa}e^{-\frac{\kappa t}{2}}a_{out}(t)dt \quad (2.7)$$

Using Eqns. 2.4 and 2.5, I write out the output mode as being equal to

$$A_{out} = a(0) \int_0^\infty \kappa e^{-\kappa t} dt + \int_0^\infty \gamma^{3/2} e^{-\kappa t} \int_0^t e^{-\frac{\kappa}{2}z} a_{in}(z) dz dt - \int_0^\infty \sqrt{\kappa} e^{-\frac{\kappa t}{2}} a_{in}(t) dt. \quad (2.8)$$

This equation simplifies to

$$A_{out} = a(0). \quad (2.9)$$

Thus, the state of the output mode A_{out} defined in Eqn. 2.7 is the same as the state of the cavity a at $t = 0$. Consequently, if the cavity is prepared in a single photon state at $t = 0$, then the output mode A_{out} is in the single photon state. Therefore, in this experiment, I am interesting in generating and measuring propagating modes similar to the mode A_{out} defined in Eqn. 2.7.

2.1.2 Quadratures

Next, I construct operators that are tied closely to linear measurement. I construct these quadrature operators Y_1 and Y_2 out of the ladder operators a and a^\dagger by forming linear superpositions. They are defined as

$$Y_1 = \frac{1}{2}(a + a^\dagger) \quad (2.10)$$

$$Y_2 = \frac{1}{2i}(a - a^\dagger). \quad (2.11)$$

This definition of Y_1 and Y_2 is in the lab frame. In this frame, the operators a and a^\dagger oscillate at ω as seen from the Heisenberg's equation

$$\dot{a} = i[H_{ho}, a] = -i\omega a. \quad (2.12)$$

Therefore,

$$a(t) = a(0)e^{i\omega t} \quad (2.13)$$

$$a^\dagger(t) = a^\dagger(0)e^{-i\omega t} \quad (2.14)$$

Because a and a^\dagger oscillate in the lab frame, Y_1 and Y_2 oscillate. I define quadratures X_1 and X_2 that do not oscillate by transforming into a frame that rotates at ω :

$$X_1 = \cos(\omega t)Y_1 + \sin(\omega t)Y_2 = \frac{1}{2}(a(0) + a^\dagger(0)) \quad (2.15)$$

$$X_2 = -\sin(\omega t)Y_1 + \cos(\omega t)Y_2 = \frac{1}{i2}(a(0) - a^\dagger(0)). \quad (2.16)$$

For the remainder of this document, quadratures refer to these quadratures in the rotating frame. Looking at the electric field operator of a mode, we can gain intuition about these two quadratures. At a particular location in the mode and aligned with the polarization, the electric field operator is [42]

$$\mathcal{E} = 2\mathcal{E}_0 (X_1 \cos(\omega t) + X_2 \sin(\omega t)), \quad (2.17)$$

where \mathcal{E}_0 is a constant with units of electric field. Thus, we can think of X_1 as the cosine and the X_2 as the sine component of an oscillating field.

These quadratures X_1 and X_2 are the operators that the JPA measures. When the JPA operates phase sensitively in homodyne mode, it measures X_1 , X_2 or a linear combination of the two

$$X_\theta = X_1 \cos(\theta) + X_2 \sin(\theta). \quad (2.18)$$

When the JPA operates phase insensitively in heterodyne mode, it measures both quadratures. However, both quadratures X_1 and X_2 cannot be determined with arbitrary accuracy because of their commutation relation

$$[X_1, X_2] = \frac{i}{2}. \quad (2.19)$$

The measurements of X_1 and X_2 have an uncertainty relationship

$$\langle(\Delta X_1)^2\rangle \langle(\Delta X_2)^2\rangle \geq \frac{1}{16}. \quad (2.20)$$

Thus, two-quadrature measurements must add noise.

2.1.3 States of the field

Having introduced the types of modes I am working with, and the operators I can measure, I highlight a few classes of classical and non-classical states that I work with. Additionally, I discuss some relevant properties of these states including quadrature expectation value and variance.

The state I want to generate and detect is the single photon state $|1\rangle$. It is one of the Fock states $|n\rangle$. These states have on average a quadrature value of

$$\langle X_\theta \rangle = 0 \quad (2.21)$$

for any $|n\rangle$. They have a quadrature variance

$$\text{var}(X_\theta) = \langle X_\theta^2 \rangle - \langle X_\theta \rangle^2 = \frac{1}{4}(2n + 1). \quad (2.22)$$

Thus, quadrature measurements of a photon states $|n\rangle$ can determine n through their variance (or higher cumulants), but not their average.

Another *state* I encounter in this experiment is a thermal distribution of states. This distribution, the thermal state, is a statistical mixture of pure Fock states characterized by a Boltzmann distribution. Because it is a statistical mixture of pure states, it must be described by a density matrix ρ rather than a single state vector. The density matrix for a thermal state $\rho_{th}(\bar{n})$ is parametrized in average photon occupation \bar{n} as

$$\rho_{th}(\bar{n}) = \sum_n \frac{\bar{n}^n}{(\bar{n} + 1)^{n+1}} |n\rangle \langle n|. \quad (2.23)$$

Here, the average photon occupation is

$$\bar{n} = \frac{1}{\exp(\hbar\omega/k_B T) - 1} \quad (2.24)$$

in terms of the temperature T and the Boltzmann constant k_B . Because the thermal state is not a pure photon or number state, it has nonzero number variance. Its number variance is

$$\text{var}(n) = \text{Tr}(\rho_{th}n^2) - \text{Tr}(\rho_{th}n)^2 = \bar{n} + \bar{n}^2. \quad (2.25)$$

Like the pure Fock states, the thermal state has an average quadrature value

$$\text{Tr}(\rho_{\text{th}} X_\theta) = 0. \quad (2.26)$$

Its quadrature variance is

$$\text{var}(X) = \text{Tr}(\rho_{\text{th}} X_\theta^2) = \frac{1}{4} + \frac{\bar{n}}{2}. \quad (2.27)$$

Quadrature measurements of thermal states also manifest themselves in the variance of the field, highlighting the need for a more sophisticated approach to distinguishing the $n = 1$ photon state for other states. Consequently in Subsections 2.3.3 and 2.3.4, I compute the probability distribution for one and two-quadrature measurement of the signal photon state.

The last major class of states I encounter in this experiment is the classically described coherent state. Quantum mechanically, I can generate a coherent state by taking the eigenvalues of the ladder operator a . Thus,

$$a |\alpha\rangle = \alpha |\alpha\rangle, \quad (2.28)$$

where $|\alpha\rangle$ is the coherent state and α is the coherent state's complex amplitude. In the Fock basis, the coherent state is

$$|\alpha\rangle = \sum_n e^{\frac{1}{2}|\alpha|^2} \frac{\alpha^n}{\sqrt{n!}} |n\rangle. \quad (2.29)$$

The coherent state has an photon number variance

$$\text{var}(n) = \bar{n}, \quad (2.30)$$

where

$$\bar{n} = \langle \alpha | n | \alpha \rangle = |\alpha|^2. \quad (2.31)$$

It has a quadrature variance

$$\text{var}(X_\theta) = \frac{1}{4} \quad (2.32)$$

equal to the vacuum state.

2.2 A two level system coupled to a cavity: CQED

The qubit is an important element for my photon generation experiment that is not described as a harmonic oscillator. Instead, it is a two level system. The qubit is coupled to a cavity to form the CQED system. To utilize and understand this system I must write out a quantum mechanical framework for it [21]. To do so, first I write out the Hamiltonian for the system including the direct coupling between the qubit and cavity. Then, I look at a useful limit, the dispersive limit, where the cavity and qubit affect each other, but do not spontaneously exchange excitations. Finally, I look at dynamics of the system including a method of photon generation.

2.2.1 Hamiltonian

By coupling a cavity mode to a qubit, I can create a system with richer dynamics. The qubit has resonant frequency ω_q and bare Hamiltonian

$$H_q = \omega_q \frac{\sigma_z}{2} \quad (2.33)$$

where σ_z is a Pauli matrix. It has two eigenstates labeled $|g\rangle$ and $|e\rangle$ for ground and excited, respectively. When an anharmonic 3 level system is considered, the third level is labeled $|f\rangle$.

Coupling the qubit to a cavity via the dipole interaction yields a coupling that is proportional to the \mathcal{E} field of the cavity dotted with that of the qubit. In other words,

$$H_{\text{int}} = g(\sigma_+ + \sigma_-)(a^\dagger + a), \quad (2.34)$$

where g is the coupling strength and a the field operator for the cavity. The Hamiltonian for the system becomes

$$H_{\text{Rabi}} = \omega_q \frac{\sigma_z}{2} + \omega_c a^\dagger a + g(\sigma_+ + \sigma_-)(a^\dagger + a) \quad (2.35)$$

known as the Rabi Hamiltonian.

2.2.2 Dispersive limit

I want to design the system so I can gain information about the qubit from the cavity mode's fields while minimally disturbing the qubit. Following Ref. [44], this condition can be achieved by going into the limit where the two level system's transition is detuned from the cavity mode by greater than the coupling between the two, that is

$$|\omega_q - \omega_c| = |\Delta| > g. \quad (2.36)$$

In this limit, called the dispersive limit, an excitation in the two level system shifts the frequency of the cavity, yet at the same time excitations do not exchange between the cavity and the qubit. In the dispersive limit, the Hamiltonian becomes

$$H_{\text{dis}} = \omega_q \frac{\sigma_z}{2} + \omega_c a^\dagger a + 2\chi \left(\frac{\sigma_z}{2} a^\dagger a \right), \quad (2.37)$$

where $\chi = \frac{g^2}{\Delta}$ and $\Delta = \omega_q - \omega_c$. The value of the dispersive shift 2χ can be determined by treating the interaction listed in Eqn. 2.33 as a perturbation using second order perturbation theory.

Regrouping the $a^\dagger a$ terms in Eqn. 2.38, I get an effective cavity frequency ω'_c that is a function of the qubit state

$$\omega'_c = \omega_c + 2\chi \frac{\sigma_z}{2}. \quad (2.38)$$

Therefore, the frequency of the cavity contains information about the state of the qubit. More specifically, detecting the 2χ dispersive shift of cavity resonances detects the state of the qubit. This dispersive shift forms the basis for a type of qubit readout I use in the my experiment. Similarly, I can regroup $\frac{\sigma_z}{2}$ terms to get an effective qubit frequency ω'_q that depends on the number of cavity photons

$$\omega'_q = \omega_q + 2\chi a^\dagger a. \quad (2.39)$$

Therefore, the frequency of the qubit contains information about the number of photons in the cavity.

2.2.3 System dynamics

Now, I describe a method of using oscillating fields to drive dynamics in the qubit-cavity system, and control the state of the qubit. First, I consider driving fields to effect the dynamics of the qubit. These fields alter the Hamiltonian of the qubit to drive transitions and allow us to perform arbitrary operations on the qubit itself. Then, I use a quantum mechanical treatment of the qubit-cavity system with drive fields to construct an effective Hamiltonian for the blue sideband transition, that jointly creates or destroys single excitation of the qubit and cavity.

2.2.3.1 Rabi oscillations

To control the qubit, I follow closely Ref. [42] and consider the qubit coupled to an oscillating drive through a dipole interaction. I treat the drive classically, where the drive adds an oscillating term to the Hamiltonian of the qubit. To understand the dynamics, I solve the equations of motion for the ground $|g\rangle$ and excited $|e\rangle$ states coefficients $C_g(t)$ and $C_e(t)$.

As result of the of the drive, I get an interaction Hamiltonian

$$H_{\text{int}}(t) = V_0 \cos(\omega_d t) \quad (2.40)$$

where $V_0 = -d(\sigma_- + \sigma_+)\mathcal{E}$ is the magnitude of coupling dipole energy, and ω_d is the drive frequency. The dipole moment of the qubit is d and the electric field of the drive is \mathcal{E} . In this case, the time dependent wavefunction for the qubit is

$$|\psi(t)\rangle = C_g(t)|g\rangle + C_e(t)e^{i\omega_q t}|e\rangle. \quad (2.41)$$

To arrive at the dynamics of the system I apply the Schrodinger equation

$$i|\dot{\psi}(t)\rangle = H(t)|\psi(t)\rangle \quad (2.42)$$

to $|\psi(t)\rangle$ listed in Eqn. 2.41. I use the two level system Hamilton with the interaction term in Eqn. 2.40. I get a set of two differential equations in terms of $C_g(t)$ and $C_e(t)$ listed as:

$$\dot{C}_g = -id\mathcal{E}\frac{1}{2}(e^{i(\omega_q+\omega_d)t} + e^{i(\omega_q-\omega_d)t})C_e \quad (2.43)$$

$$\dot{C}_e = -id\mathcal{E}\frac{1}{2}(e^{i(\omega_q+\omega_d)t} + e^{i(\omega_q-\omega_d)t})C_g. \quad (2.44)$$

Because I am driving a qubit near its resonance, the $\omega_q + \omega_d$ term oscillates much faster than the $\omega_q - \omega_d$ term. Due to the fast oscillations, the dynamics of the $\omega_q + \omega_d$ terms are averaged over, and I can therefore drop these terms in what is called the rotating wave approximation. Solving the differential Eqns. 2.43 and 2.44 with boundary conditions $C_g(0) = 1$ and $C_e(0) = 0$, I get

$$C_e(t) = \frac{i\mathcal{E}d}{\Omega_r} e^{i\Delta t/2} \sin\left(\frac{\Omega_r t}{2}\right), \quad (2.45)$$

where $\Delta = \omega_q - \omega_d$ and $\Omega_r = \sqrt{\Delta^2 + d^2\mathcal{E}^2}$. The excited state probability is $P_e(t) = |C_e(t)|^2$.

Therefore,

$$P_e(t) = \frac{(\mathcal{E}d)^2}{\Omega_r^2} \sin^2\left(\frac{\Omega_r t}{2}\right). \quad (2.46)$$

This simplifies when driving on resonance ($\Delta = 0$) to

$$P_e(t) = \sin^2\left(\frac{\Omega_r t}{2}\right). \quad (2.47)$$

Eqns. 2.47 and 2.45 demonstrate that a microwave drive can control the state of the qubit. Starting from any known pure state of the qubit, I can use an on resonance drive to prepare the qubit in any desired pure state $\Psi = A|g\rangle + B|e\rangle$.

2.2.3.2 Sideband drives

Now I consider the whole qubit-cavity system's response to drives that effect both the qubit and cavity states. I can drive transitions that jointly create excitations of the cavity and qubit, or swaps them. These transitions are named as if the qubit modulates the cavity frequency ($|\omega_c \pm \omega_q|$). The transition on the *blue* (higher frequency) side of the cavity ($\omega_c + \omega_q$), which jointly creates excitation in the cavity and qubit, is called the blue sideband. The transition on the *red* (lower frequency) side of the cavity ($|\omega_c - \omega_q|$), which swaps excitations between the cavity and qubit, is called the red sideband. For my style of qubit, the transmon qubit, these transitions can only occur as a two photon process. Therefore they are achieved by using two photons each of energy $|\omega_c \pm \omega_q|/2$.

To construct the sideband dynamics I closely follow Ref. [45]. I consider two drives acting on the qubit and add them into the Rabi Hamiltonian. I then perform three unitary transformations on

the Hamiltonian keeping only the lowest order terms to simplify the Hamiltonian. Finally, I set the drive frequency to the sideband transition $(\omega_c + \omega_q)/2$ and perform a rotating wave approximation to yield an effective Hamiltonian for the sideband drive. The effective, sideband Hamiltonian clearly shows the blue sideband transition.

To start, the two drives have a Hamiltonian

$$H_{\text{drive}} = \sum_{j=1,2} \Omega_j (a^\dagger + a) \cos \omega_{d,j} t. \quad (2.48)$$

I add the driving terms to the Rabi Hamiltonian (Eqn. 2.35) $H_{\text{Rd}} = H_{\text{Rabi}} + H_{\text{drive}}$. I then perform the first unitary transformation

$$H_{\text{QCD}} = U_{2d}^\dagger H_{\text{Rd}} U_{2d} - i U_{2d}^\dagger \dot{U}_{2d} \quad (2.49)$$

built from two displacements corresponding to the two drives

$$U_{2d} = \Pi_{j=1,2} D(\alpha_j(t)), \quad (2.50)$$

where $D(\alpha)$ is the displacement operator, with $\alpha_j(t)$ chosen to eliminate direct drive couplings by setting

$$\dot{\alpha}_j(t) = -i\omega_c \alpha_j(t) - i\Omega_j e^{-i\omega_{d,j} t}. \quad (2.51)$$

By applying a rotating wave approximation on the drive, the transformed Rabi Hamiltonian becomes

$$H_{\text{QCD}} = \omega_q \frac{\sigma_z}{2} + \omega_c a^\dagger a + g(\sigma_+ + \sigma_-)(a^\dagger + a) + \sum_{j=1,2} \Omega_j (\sigma_+ e^{-i\omega_{d,j} t} + \sigma_- e^{i\omega_{d,j} t}). \quad (2.52)$$

Next to remove the direct coupling between the qubit and drive, I apply a second unitary transformation on the Hamiltonian of the form $H' = U_\beta^\dagger H_{\text{QCD}} U_\beta - i U_\beta^\dagger \dot{U}_\beta$ with

$$U_\beta = \exp(\beta \sigma_- - \beta^* \sigma_+), \quad (2.53)$$

for

$$\beta = \frac{1}{2} \sum_{j=1,2} \frac{\Omega_j}{\omega_q - \omega_{d,j}} e^{i\omega_{d,j} t}. \quad (2.54)$$

Applying U_β to the Hamiltonian in Eqn. 2.52, I get the Hamiltonian

$$H' = \omega'_q \frac{\sigma_z}{2} + \omega_c a^\dagger a - g(\sigma_+ + \sigma_-)(a^\dagger + a) - g(\beta^* + \beta)(\sigma_z - \beta^* \sigma_+ - \beta \sigma_-)(a^\dagger + a). \quad (2.55)$$

Now, I perform the third and final unitary transformation on the Hamiltonian, the dispersive transformation

$$U_{\text{dis}} = \exp\left[\frac{g}{\omega_q - \omega_c}(a^\dagger \sigma_- - a \sigma_+)\right], \quad (2.56)$$

which eliminates spontaneous qubit-cavity transitions. By applying this transformation to the Hamiltonian in Eqn. 2.55, I get an effective Hamiltonian for a qubit cavity system with two off resonance drives

$$H_{\text{eff}} = \omega'_q \frac{\sigma_z}{2} + \omega_c a^\dagger a - g(\beta^* + \beta)\sigma_z + \sum_{k,k'=1,2} g \frac{\Omega_k}{\omega_q - \omega_k} \frac{\Omega'_k}{\omega_q - \omega'_k} (a + a^\dagger) \\ \times [(e^{i(\omega_k - \omega_{k'})t} + e^{-i(\omega_k + \omega_{k'})t})\sigma_- + (e^{-i(\omega_k - \omega_{k'})t} + e^{-i(\omega_k + \omega_{k'})t})\sigma_+]. \quad (2.57)$$

This Hamiltonian fully describes a qubit-cavity system that has two drives.

I now consider drives at the blue sideband transition to get the effective blue sideband Hamiltonian. I set both drives to the same frequency such that $2\omega_{k(\prime)} = \omega''_q + \omega_c$ in Eqn. 2.57. The frequency ω''_q is the shifted qubit frequency with value

$$\omega''_q = \omega_q + \frac{\Omega_1^2}{\omega_q - \omega_1} + \frac{\Omega_2^2}{\omega_q - \omega_2} + 2\chi \langle a^\dagger a \rangle. \quad (2.58)$$

Then, I perform two last rotating wave approximations on Eqn. 2.57 at the qubit and cavity frequency by performing rotations defined by $U_q = e^{-i\omega_q \frac{\sigma_z}{2} t}$ and $U_c = e^{-i\omega_c a^\dagger a t}$ and dropping the fast oscillating terms. At last, I get the Hamiltonian for the blue sideband transition

$$H_{\text{blue}} = \frac{\Omega_1^2}{\omega_q - \omega_1} \frac{\Omega_2^2}{\omega_q - \omega_2} \frac{g}{4} (a^\dagger \sigma_+ + a \sigma_-). \quad (2.59)$$

Written more simply

$$H_{\text{blue}} = \Omega_{\text{blue}} (a^\dagger \sigma_+ + a \sigma_-). \quad (2.60)$$

For the system starting in $|g, 0\rangle$ state (where the labels are |qubit state, cavity photon number)), H_{blue} causes the system to oscillate between $|g, 0\rangle$ and $|e, 1\rangle$ states at rate Ω_{blue} . Therefore, I can

drive the blue sideband transition to prepare the system in the $|e, 1\rangle$ state, and thus create a single photon in the cavity.

2.3 Measuring a quantum state

Now that I have introduced a quantum mechanical description of circuits and single photon generation, I discuss the framework for performing measurements on the photon state. I briefly describe the transformation that the JPA performs to amplify states. Then, I move on to the theory of measuring a quantum state. Before discussing specific measurements, I introduce a quadrature, or phase space, representation of quantum states called the Wigner function. I form expectations of single quadrature and two quadrature measurements of quantum states. Finally, I introduce a model that incorporates loss or inefficiency into these measurements.

2.3.1 Parametric amplifier measurements

The JPA is a microwave amplifier that amplifies propagating fields over a tunable frequency band. In an ideal sense, the JPA performs transformations of two incident quadratures $X_{1,\text{in}}^{\text{JPA}}$ and $X_{2,\text{in}}^{\text{JPA}}$ in a frame that rotates at the center frequency ω_{JPA} of the JPA's band. These transformations amplify one quadrature while deamplifying the other to create two outgoing quadratures. This amplification occurs on an arbitrary quadrature $X_{\text{in}}^{\text{JPA}}$ with phase set by the pump tone(s). After the quadrature is amplified in the ω_{JPA} frame, the measurement is completed by demodulating the JPA's output $X_{\text{out}}^{\text{JPA}}$ by ω_{JPA} . This demodulation turns measurements of $X_{\text{in}}^{\text{JPA}}$ in the rotating frame to measurements of $X_{\text{in}}^{\text{JPA}}$ in the lab frame which do not oscillate in time, and therefore can be directly digitized.

Regardless of whether the JPA operates in homodyne or heterodyne mode, in the ω_{JPA} frame the JPA's fundamental transformations are the same. By defining $X_{1,\text{in}}^{\text{JPA}}$ as the amplified

quadrature, the JPA's transformations are summarized as [24]

$$X_{1,\text{out}}^{\text{JPA}} = G_Q X_{1,\text{in}}^{\text{JPA}} \quad (2.61)$$

$$X_{2,\text{out}}^{\text{JPA}} = \frac{1}{G_Q} X_{2,\text{in}}^{\text{JPA}} \quad (2.62)$$

with quadrature gain G_Q .

The mode of operation (homodyne or heterodyne) is determined by whether or not the signals are at ω_{JPA} . For the JPA to operate in homodyne mode, the signal or the center of the signal's band must be at ω_{JPA} . In this case, the quadratures in the signal's frame X_1^{sig} and X_2^{sig} and the quadrature that describe the JPA's transformation X_1^{JPA} and X_2^{JPA} are in the same rotating frame, ω_{JPA} . Thus, when the JPA amplifies $X_{1,\text{in}}^{\text{JPA}}$, it directly amplifies X_1^{sig} . After demodulation at ω_{JPA} , the digitized output $V_m(t)$ is a direct measurement of the signal's quadrature X_1^{sig}

$$V_m(t) = G_Q X_1^{\text{sig}}. \quad (2.63)$$

For the JPA to operate in heterodyne mode, the signal must be detuned from ω_{JPA} . For detuning Δ , the quadratures that describe the signal X_1^{sig} and X_2^{sig} are in a frame rotating at $\omega_{\text{JPA}} + \Delta$. The JPA still performs its amplifying transformation on the quadratures in a frame that rotates at ω_{JPA} . In terms of the quadratures in the signal's frame, I write the JPA's input in the ω_{JPA} frame as

$$X_{1,\text{in}}^{\text{JPA}} = \cos(\Delta t) X_1^{\text{sig}} + \sin(\Delta t) X_2^{\text{sig}} \quad (2.64)$$

$$X_{2,\text{in}}^{\text{JPA}} = -\sin(\Delta t) X_1^{\text{sig}} + \cos(\Delta t) X_2^{\text{sig}}. \quad (2.65)$$

Then, the JPA's outputs are

$$X_{1,\text{out}}^{\text{JPA}} = G_Q(\Delta) \left(\cos(\Delta t) X_1^{\text{sig}} + \sin(\Delta t) X_2^{\text{sig}} \right) \quad (2.66)$$

$$X_{2,\text{out}}^{\text{JPA}} = \frac{1}{G_Q(\Delta)} \left(-\sin(\Delta t) X_1^{\text{sig}} + \cos(\Delta t) X_2^{\text{sig}} \right), \quad (2.67)$$

where $G_Q(\Delta)$ is the JPA's quadrature gain Δ from the center of the JPA's band. After demodulating the JPA's amplified quadrature at ω_{JPA} , I find the digitized output to be

$$V_m(t) = G_Q(\Delta) \cos(\Delta t + \phi) X_1^{\text{sig}} + G_Q(\Delta) \sin(\Delta t + \phi) X_2^{\text{sig}}. \quad (2.68)$$

Thus, the JPA's one amplified quadrature contains information about both of the signals quadratures. By fitting the output $V_m(t)$ to a function $C_1 \cos(\Delta t + \phi) + C_2 \sin(\Delta t + \phi)$ in terms of constants C_1 and C_2 , I can extract measurements of two quadratures X_1^{sig} and X_2^{sig} based on the values C_1 and C_2 , respectively.

By considering multiple rotating reference frames, we can understand the origin of the 1/2 quanta (one vacuua) of added noise heterodyne measurements must introduce. At the JPA's input, both fields oscillating at $\omega_{\text{JPA}} + \Delta$ and fields oscillating at $\omega_{\text{JPA}} - \Delta$ are amplified and demodulated at ω_{JPA} causing $V_m(t)$ to oscillate at Δ . Consequently, at best amplified vacuum noise (that oscillated at $\omega_{\text{JPA}} - \Delta$) is added to the amplified signal (that oscillated $\omega_{\text{JPA}} + \Delta$) in the digitized output $V_m(t)$, both oscillating at Δ . The amplified vacuum is then indistinguishable from the amplified signal. Thus at a minimum, vacuum noise is added to the amplified signal.

2.3.2 Wigner function

To visualize quantum states in phase space, I use a quasi-probability distribution function of the two quadratures called the Wigner function $W(X_1, X_2)$. If X_1 and X_2 were classical coordinates, then the Wigner function would become a true joint probability distribution of the quadratures. However, X_1 and X_2 are operators that have an uncertainly relation. They cannot be simultaneously measured without adding noise, therefore one cannot directly measure the Wigner function from quadrature measurements. Because $W(X_1, X_2)$ is not a classical probability distribution, it is possible for $W(X_1, X_2)$ to have negative values, further distinguishing it from a true probability distribution.

The Wigner function is a valid representation of the density matrix. From a density matrix ρ the Wigner function is calculated by

$$W(X_1, X_2) = \frac{1}{\pi \hbar} \int e^{-i2yX_2} \langle X_1 - y | \rho | X_1 + y \rangle dy. \quad (2.69)$$

As an example, I plot the Wigner function for a single photon (Fig. 2.1). The nonclassical nature of the single photon state is seen in the negative values of the Winger function at the origin. Now

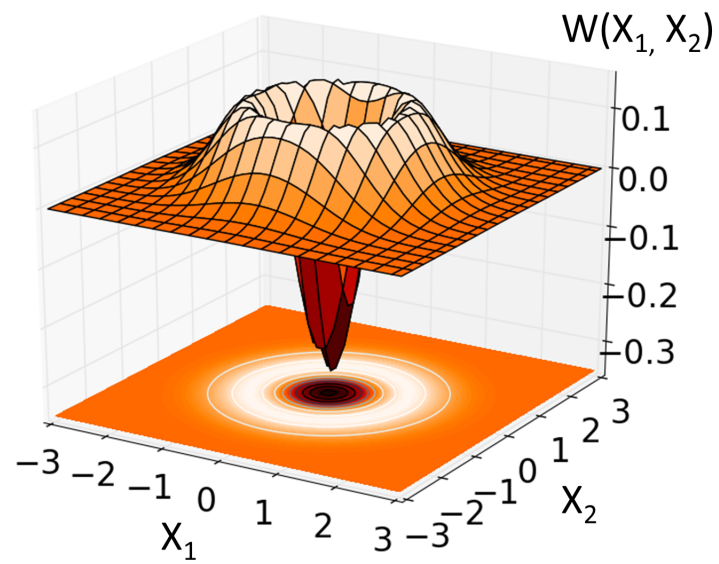


Figure 2.1: The Wigner function for a single photon state ($n = 1$).

that I have the Wigner function representation of quantum states, I can use it to calculate expected probability distributions for one and two quadrature measurements.

2.3.3 Homodyne measurement of quantum states

Because single quadrature, or homodyne, measurements can ideally be performed without the addition of noise, these can be directly calculated from the Wigner function without convolving any additional Gaussian noise. To calculate the single quadrature probability distribution of a quantum state, I integrate it's Winger function over the orthogonal quadrature

$$P(X_1) = \int W(X_1, X_2) dX_2. \quad (2.70)$$

As an example, I plot the $P(X_1)$ for a single photon state (Fig. 2.2). This probability distribution is non-Gaussian, which distinguishes it from Gaussian probability distributions created by vacuum, thermal, displaced thermal, squeezed, and coherent states. Therefore measuring these homodyne and heterodyne probability distributions can form a method for identifying the $n = 1$ photon state in this experiment.

2.3.4 Heterodyne measurement of quantum states

A two quadrature, or heterodyne, measurement adds at least vacuum noise because the two quadratures are canonically conjugate variables. The two-quadrature probability distribution can either be calculated by convolving the Wigner function with vacuum noise or calculated directly from ρ . To calculate directly, I can calculate the Husimi-Q function

$$P(X_1, X_2) = Q(X_1, X_2) = \langle X_1 + iX_2 | \rho | X_1 + iX_2 \rangle / \pi. \quad (2.71)$$

Alternatively, I can calculate the distribution from the Winger function by performing the convolution

$$P(X_1, X_2) = \frac{2}{\pi} \int W(Y_1, Y_2) e^{-2|X_1 + iX_2 - Y_1 - iY_2|} dY_1 dY_2. \quad (2.72)$$

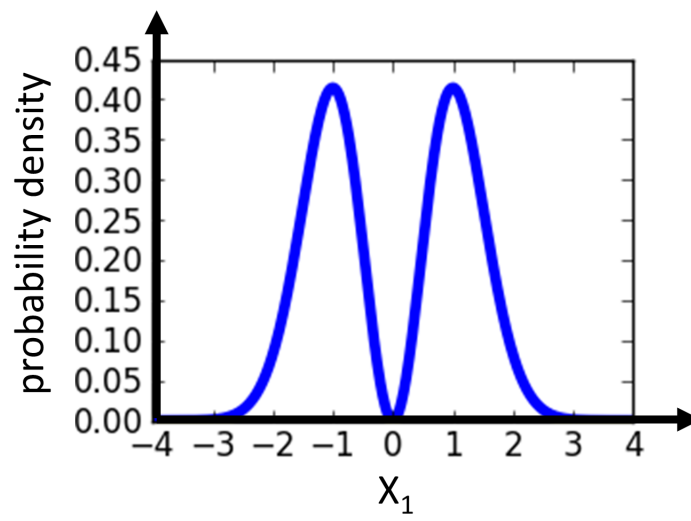


Figure 2.2: Homodyne measurement of a single photon: single quadrature probability distribution for the $n = 1$ Fock state.

As an example, I plot the $P(X_1, X_2)$ for a single photon state (Fig. 2.3). Just like the single quadrature measurements, this probability distribution is non-Gaussian, and therefore distinguishable from Gaussian probability distributions.

2.3.5 Inefficient measurement

Measurement inefficiency and loss can be incorporated by using a model where a beam splitter replaces some of the signal with vacuum fluctuations. In this model, one of the beam splitters inputs is the density matrix ρ_{in} that I am measuring and the other is the vacuum state $|0\rangle\langle 0|$. I measure one of the outputs, and the other output represents degrees of freedom I do not measure. The power transmission η of ρ_{in} to the measured output represents the efficiency of the measurement. To calculate the measured density matrix, I first perform a beam-splitter transformation on the input modes. Then, I sum over, or trace over, the mode I do not measure.

I define the beam splitter transformation in terms of two input modes labeled a_1^{in} and a_2^{in} and output modes labeled a_1^{out} and a_2^{out} . I inject my quantum state in input mode 1 and measure output mode 1. The beam splinter transformation is defined as

$$\begin{pmatrix} a_1^{\text{out}} \\ a_2^{\text{out}} \end{pmatrix} = \begin{bmatrix} \cos \vartheta & i \sin \vartheta \\ i \sin \vartheta & \cos \vartheta \end{bmatrix} \begin{pmatrix} a_1^{\text{in}} \\ a_2^{\text{in}} \end{pmatrix} \quad (2.73)$$

for a beams splitter with power transmission $\eta = \cos^2 \vartheta$. I can perform the beam splitter transformation by either directly substituting the ladder operators according to Eqn. 2.73, or by applying a unitary transformation operator

$$U_{\text{bs}} = e^{i\theta(a_1^\dagger a_2 + a_1 a_2^\dagger)}. \quad (2.74)$$

From the input modes (ρ_{in} in mode 1 and vacuum in mode 2), I apply the unitary transformation to get the output

$$\rho_{12}^{\text{out}} = U_{\text{bs}} \rho_1^{\text{in}} \otimes |0_2\rangle\langle 0_2| U_{\text{bs}}^\dagger. \quad (2.75)$$

Because I only measure output mode 1, I trace over output mode 2 to get the measured density

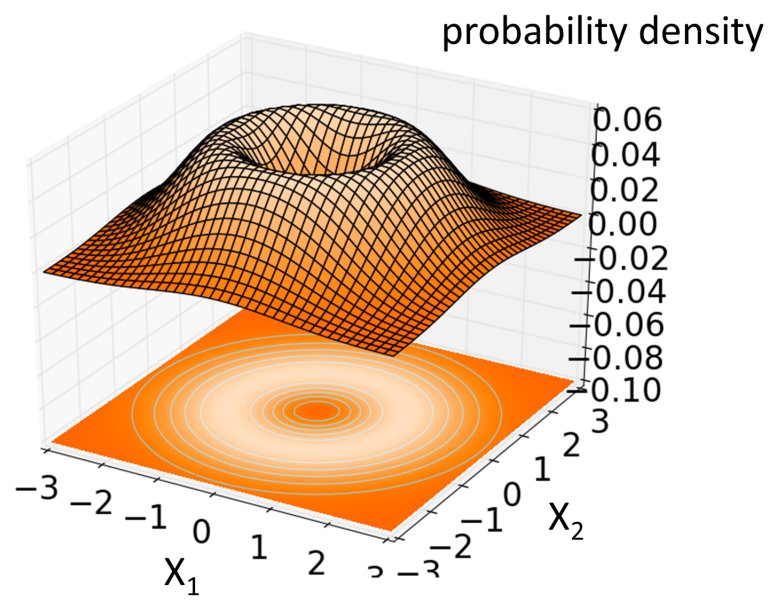


Figure 2.3: Heterodyne measurement of a single photon: two quadrature probability distribution for the $n = 1$ Fock state.

matrix

$$\rho_{\text{meas}} = \text{tr}_2(\rho_{12}^{\text{out}}) = \sum_{n_2} \langle n_2 | \rho_{12}^{\text{out}} | n_2 \rangle. \quad (2.76)$$

With this framework, I can calculate the density matrix for measuring a single photon with efficiency η . In this case

$$\rho_{\text{in}} = |1\rangle \langle 1|. \quad (2.77)$$

Then, the two-mode, output density matrix is

$$\rho_{12}^{\text{out}} = \eta |1, 0\rangle \langle 1, 0| - i\sqrt{\eta + \eta^2}(|1, 0\rangle \langle 0, 1| - |0, 1\rangle \langle 1, 0|) + (1 - \eta) |0, 1\rangle \langle 0, 1|. \quad (2.78)$$

After tracing over mode 2, I get the measured density matrix

$$\rho_{\text{meas}} = \eta |1\rangle \langle 1| + (1 - \eta) |0\rangle \langle 0|, \quad (2.79)$$

where $|1\rangle \langle 1|$ is the density matrix of a single photon. Thus, measuring a single photon with efficiency η yields a mixed state with a single photon component $\rho_{11} = \eta$. Probability distributions for homodyne and heterodyne measurements can be computed for ρ_{meas} using Eqns. 2.70 and 2.72.

Chapter 3

Qubit and cavity design

The central resource for photon generation is the qubit-cavity system. To experimentally realize this idealized system, I create and couple two elements. The first element is a nonlinear LC circuit, which acts as the qubit. The second element, the cavity, is a single mode of a 3D waveguide cavity. In this Chapter, I first discuss the design and fabrication of the individual pieces, then discuss the details of combining and coupling them.

3.1 The qubit

The qubit is an LC circuit that contains a strong nonlinear element. The qubit is formed by connecting a structure known as a Josephson junction to a capacitor. The Josephson junction is an electrically nonlinear inductor, thus forming the LC circuit. In superconducting circuits, Josephson junctions are the only means of implementing a strong nonlinearity with low dissipation [24, 46]. They form the basis of all types of superconducting qubits (flux, phase, charge, transmon) [47, 48, 49, 50]. A Josephson junction is formed by weakly connecting two regions of superconductivity [51].

The strength of the nonlinearity is set by a single parameter: the junctions critical current I_0 , which is the maximum supercurrent that can tunnel across the junction. The nonlinearity of the Josephson junction can be seen through its Hamiltonian

$$H_J = E_J \left(1 - \cos \frac{\Phi}{\Phi_0}\right), \quad (3.1)$$

where Φ is the flux through the junction. The constant $\Phi_0 = \frac{\pi\hbar}{e}$ is the magnetic flux quantum,

where e is the charge of an electron, and

$$E_J = \frac{I_0 \Phi_0}{2\pi} \quad (3.2)$$

is the Josephson energy [52]. Because the H_J depends on the cosine of Φ , this term is nonlinear. Thus, I_0 sets E_J and therefore the strength of nonlinearity. I can show H_J specifically corresponds to a nonlinear inductance by Taylor expanding $\frac{\Phi}{\Phi_0}$ to get

$$H_J = E_J \left[\left(\frac{\Phi}{\Phi_0} \right)^2 - \left(\frac{\Phi}{\Phi_0} \right)^4 + \dots \right]. \quad (3.3)$$

In comparison, the Hamiltonian of a linear inductor is

$$H_L = E_L \left(\frac{\Phi}{\Phi_0} \right)^2, \quad (3.4)$$

where $E_L = \Phi_0/(2L)$. Therefore, H_J is the Hamiltonian of an inductor with higher order $\frac{\Phi}{\Phi_0}$ terms.

3.1.1 From linear to non-linear circuits

In order for the nonlinear LC circuit to act as a qubit, it must be an effective two level system that I can control. To create an effective two level system from a non-linear circuit, the circuit resonance frequency shift per excitation must be larger than the circuits linewidth or decay rate [53]. As a starting point, let's first consider a linear circuit. In a linear LC resonator, the Hamiltonian is

$$H_{LC} = E_C(Q^2) + E_L \left(\frac{\Phi}{\Phi_0} \right)^2, \quad (3.5)$$

where Q is the charge, and E_C is the charging energy. This Hamiltonian is equivalent to a harmonic oscillator

$$H_{LC} = \sqrt{2E_C E_L} \left(a^\dagger a + \frac{1}{2} \right), \quad (3.6)$$

with energy levels spaced $\sqrt{2E_C E_L}$. Because all the transitions are harmonic, it is impossible to address a single transition without inadvertently addressing other transitions, and therefore, it cannot act as a two level system. If I introduce a weak non-linear term that shift the frequency by K for each exciton added to the circuit, the Hamiltonian becomes

$$H_{JPA} = \omega \left(a^\dagger a + \frac{1}{2} \right) - K a^\dagger a a^\dagger a. \quad (3.7)$$

If the circuit has a linewidth that is larger than the non-linearity term ($\kappa > K$), then the circuit changes its resonance frequency by more than the linewidth only when there are many excitations in the circuit (as is the case for the JPA). Therefore, it is impossible to address single transitions because the difference in adjacent energy levels is smaller than their linewidths.

By using a strong nonlinearity, I enter a regime that is fundamentally different. For my qubit, the non-linearity is quantified by the difference between the first transition $|g\rangle$ to $|e\rangle$ and the next transition $|e\rangle$ to $|f\rangle$, which is $|\alpha_K| = 0.25$ GHz. The linewidth is $\kappa_q = 26$ kHz. Because $|\alpha_K|$ is much greater than κ_q , it is possible to treat this system as a two level system. Moreover, I can drive the qubit with a fast pulse and not excite any higher order transitions as long as the pulse's spectral width is smaller than $|\alpha_K|$. Thus, $|\alpha_K|$ sets how fast I can control the system's dynamics with it still behaving as an effective two level system [54].

3.1.2 Cooper pair box

My qubit combines a Josephson junction and capacitor to form what is called a Cooper pair box (CPB). Specifically, I work in a special case of the CPB that is insensitive to charge noise called a transmon qubit. The CPB is formed by taking a Josephson junction and connecting it in parallel to a capacitor. A gate is capacitively coupled to the CPB to provide tunability of the system. If an explicit gate is not present in the design, parasitic capacitance still forms an effective gate [52, 55, 47, 56]. A circuit diagram is shown in Fig. 3.1, where the cross indicates a Josephson junction.

I form the CPB Hamiltonian by combining the Hamiltonian for a Josephson junction (Eqn. 3.2) with the Hamiltonian for a capacitor with a gate to control its charge. The CPB Hamiltonian is then

$$H_{\text{CPB}} = 4E_c(n - n_g)^2 - E_J \cos \phi. \quad (3.8)$$

The first term is the charging energy, corresponding to the energy stored in the capacitors. The capacitors and Josephson junction form an island as shown in Fig. 3.1. The dimensionless charge $(n - n_g)$ on the island is set by the the dimensionless gate voltage n_g and the operator n corre-

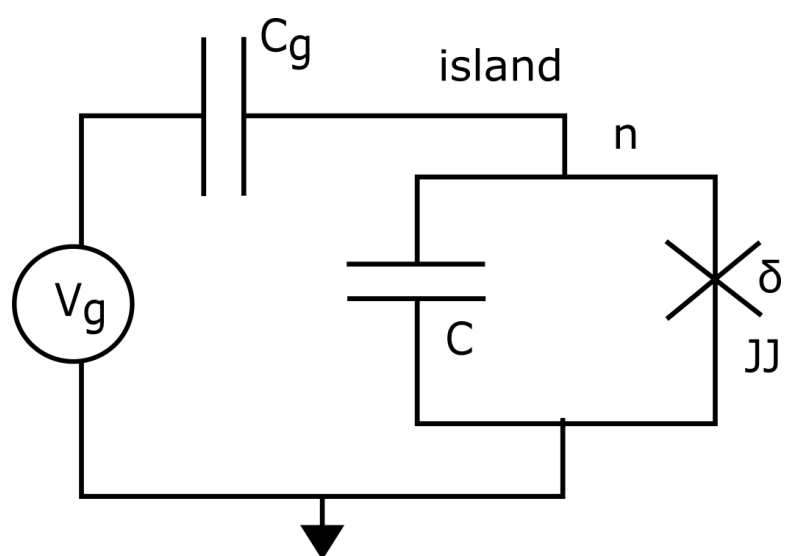


Figure 3.1: The circuit schematic of a Cooper pair box (CPB).

sponding to the number of Cooper pairs on the island. One unit of dimensionless charge (in units $2e$ corresponding to one Cooper pair) with total capacitance C_Σ has a charging energy equal to

$$4E_c = \frac{(2e)^2}{2C_\Sigma}. \quad (3.9)$$

The second term, the energy of the Josephson junction, is written in terms of the macroscopic phase difference across the junction $\phi = \frac{\Phi}{\Phi_0}$. Because the number of Cooper pairs on the island changes when they tunnel across the junction, phase and number operators are dependent. The phase and number operator have a commutation relation

$$[\phi, n] = i, \quad (3.10)$$

which allows the CPB Hamiltonian (Eqn. 3.8) to be solved in either number n , or phase ϕ basis.

Before I go into the phase basis to understand the transmon limit, I briefly look at the number basis to gain some intuition about the solutions. In the number basis, we think of the solutions as number eigenstates with a coupling term introduced by the Josephson energy. I can write the Josephson energy term as, $H_j = -\frac{E_J}{2} \sum_n (|n\rangle \langle n+1| + |n+1\rangle \langle n|)$. In this basis, the CPB Hamiltonian becomes

$$H_{\text{CPB}} = 4E_c(n - n_g)^2 - \frac{E_J}{2} \sum_n (|n\rangle \langle n+1| + |n+1\rangle \langle n|) \quad (3.11)$$

[52]. For large E_c/E_J , the left term (E_c) dominates the Hamiltonian. As a consequence, the number states form parabolas over gate voltage as shown in Fig. 3.2 as dashed lines. These number states are coupled by E_J causing the charge eigenstates to couple near degeneracies. Thus, the H_{CPB} 's eigenstates form oscillatory bands shown as the solid color lines.

The transitions are anharmonic and can form an effective two level system or qubit. As shown in Fig. 3.2, the $|g\rangle$ (red) to $|e\rangle$ (blue) transition has a different energy than the $|e\rangle$ (blue) to $|f\rangle$ (green) transition for nearly every value of n_g . By tuning the gate voltage, I can tune these transitions, therefore tune the frequency of the qubit. However, as a direct consequence of the qubits tunability with gate voltage, fluctuation in gate voltage or charge will cause the qubit frequency to fluctuate, thus dephasing the qubit.

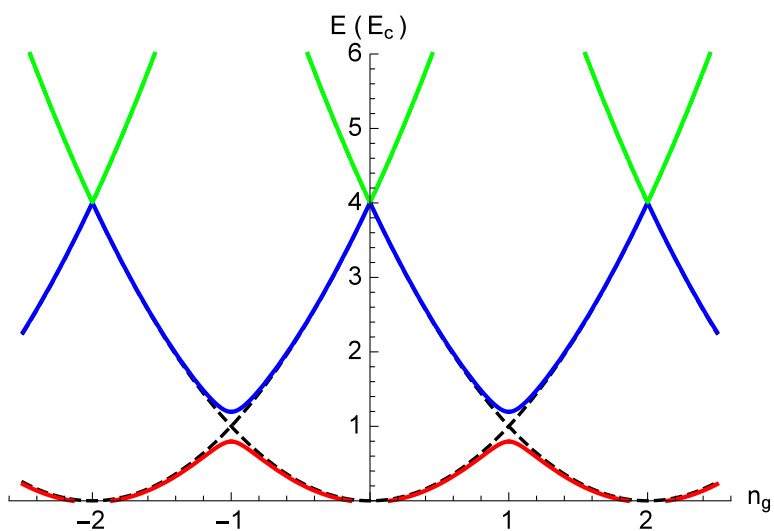


Figure 3.2: The energy levels of the CPB in the large charging energy E_c limit ($E_J/E_c = 0.2$). The charging energy states of Cooper pair number state (black dash lines) are coupled by the Josephson energy E_J , forming the system eigenstates (solid lines).

3.1.3 CPB dynamics in phase basis

Because the CPB is potentially sensitive to charge noise, I consider the transmon limit where the eigenstates become insensitive to charge at the expense of decreasing the anharmonicity. To understand this charge insensitive limit, I closely follow Ref. [57]. I first write the equations that describe the dynamics of the CPB in the phase basis. Next, I cast the equation of motion in a form with analytic solutions. Then I write the energy eigenstates in terms of a characteristic equation for these differential equations using the CPB parameters. Lastly, I look at these solutions in the charge insensitive limit.

I solve for the eigenstates by solving the Schrodinger equation in the phase basis. Because of the commutation relation in Eqn. 3.10, I can write the number operator as $n = -i\frac{\partial}{\partial\phi}$. Then, the Hamiltonian becomes

$$H_{\text{CPB}} = 4E_c(-i\frac{\partial}{\partial\phi} - n_g)^2 - E_J \cos \phi. \quad (3.12)$$

Then, the Schrodinger equation is

$$[4E_c(-i\frac{\partial}{\partial\phi} - n_g)^2 - E_J \cos \phi]\Psi(n, \phi) = E_{\text{CPB}}\Psi(n, \phi) \quad (3.13)$$

I cast this equation in the form of a particular differential equation known as the Mathieu equation, which has the form:

$$\frac{d^2y}{dx^2} + [a - 2q \cos(2x)]y = 0. \quad (3.14)$$

Because the solutions of the Mathieu equation are known in terms of special functions, then the eigenstates and energies of the differential equation are also known in terms of these special functions.

I begin by changing variables in the Schrodinger equations (Eqn. 3.13) to suppress its n_g dependence. I write the equation in terms of $h(\phi)$ with $\Psi(\phi) = h(\phi)e^{in_g\phi}$. So, then

$$4E_c e^{in_g\phi}(-i\frac{\partial}{\partial\phi})^2 h(\phi) - E_J \cos \phi e^{in_g\phi} h(\phi) = E_{\text{CPB}} e^{in_g\phi} h(\phi). \quad (3.15)$$

By canceling $e^{in_g\phi}$ and simplifying I get:

$$\frac{\partial^2}{\partial^2\phi} h(\phi) + \left(\frac{E_{\text{CPB}}}{4E_c} + \frac{E_J}{4E_c} \cos \phi \right) h(\phi) = 0. \quad (3.16)$$

To write the simplified differential equation (Eqn. 3.16) as a Mathieu equation, I start by substituting $2x = \phi$, noting that $\frac{\partial}{\partial \phi} = \frac{\partial x}{\partial \phi} \frac{\partial}{\partial x} = \frac{1}{2} \frac{\partial}{\partial x}$. Thus,

$$\frac{\partial^2}{\partial^2 x} h(2x) + \left(\frac{E_{\text{CPB}}}{E_c} + \frac{E_J}{E_c} \cos 2x \right) h(2x) = 0. \quad (3.17)$$

Lastly, I substitute $h(2x) = g(x)$, so then

$$\frac{\partial^2}{\partial^2 x} g(x) + \left(\frac{E_{\text{CPB}}}{E_c} + \frac{E_J}{E_c} \cos 2x \right) g(x) = 0. \quad (3.18)$$

In the standard form, this becomes:

$$\frac{\partial^2}{\partial^2 x} g(x) + (a - 2q \cos 2x) g(x) = 0 \quad (3.19)$$

where,

$$\Psi(\phi) = \Psi(2x) = g(x) e^{i2n_g x} = g(\phi/2) e^{in_g \phi}, \quad (3.20)$$

$$a = \frac{E_{\text{CPB}}}{E_c}, \quad (3.21)$$

and

$$q = -\frac{E_J}{2E_c}. \quad (3.22)$$

In Eqn. 3.19, I have written the CPB Hamiltonian and equations of motion in terms of Mathieu equations [57, 58]. Next, I solve this equation to find the system's eigenenergies.

3.1.4 CPB solutions in phase basis

By solving the Mathieu equation, I arrive at the solution of the CPB for all values of charging energy E_c , Josephson energy E_J , and dimensionless gate voltage n_g . The Mathieu equation has eigenvalues a parametrized by q , defined for the CPB in Eqns. 3.21 and 3.22, respectively. Additionally, the eigenvalues are parametrized in terms of a constant ν (not found in the Mathieu equation), which sets the periodicity or phase gained from a π offset of the corresponding eigenstate. The constant ν is written formally as $g(x + \pi) = e^{i\nu\pi} g(x)$. These eigenvalues, Mathieu characteristic value, are conventionally expressed as $a_\nu(q)$. The values of $a_\nu(q)$ are tabulated for ν and q and built into computational software such as Mathematica.

Because $E_\nu^{\text{CPB}}(q) = E_c a_\nu(q)$ and $q = -\frac{E_J}{2E_c}$, then the CPB's energy eigenstates are

$$E_{\text{CPB}} = E_c a_\nu\left(-\frac{E_J}{2E_c}\right)$$

Because I know E_J and E_c , my task is to find ν . I start by stating that the wavefunction Ψ is periodic in ϕ and note the restrictions it places on ν .

$$\Psi(\phi + 2\pi) = \Psi(\phi) = \Psi(\phi)e^{i(-l2\pi)}$$

where l is an integer. Changing variables from ϕ to x ($\phi = 2x$), I find

$$\Psi(2x + 2\pi) = \Psi(2x)e^{i(-l2\pi)}.$$

Writing Ψ in terms of $g(x)$ from Eqn. 3.20 ($\Psi(2z) = g(z)e^{2n_g z}$), I have

$$g(x + \pi)e^{2n_g(x+\pi)} = g(x)e^{2n_g x} e^{i(-l2\pi)}.$$

So then,

$$g(x + \pi) = g(x)e^{-2\pi(n_g+l)}.$$

Comparing with the definition of ν , I find that

$$\nu = -2(n_g + l) \tag{3.23}$$

where l is an integer. For a given n_g , the ground state is whichever state corresponds to the value of l that minimizes the eigenvalue. Please note that $\pm\nu$ yield identical eigenvalues. Combining these, I find CPB's energy eigenvalues

$$E_{\text{CPB}} = E_c a_\nu(q) = E_c a_{-2(n_g+l)}\left(-\frac{E_J}{2E_c}\right) \tag{3.24}$$

in terms of the standard solutions to the Mathieu equation. Here in Eqn. 3.24, I have the energy levels for a CPB for any Josephson energy E_J , charging energy E_c and gate voltage n_g [57, 58].

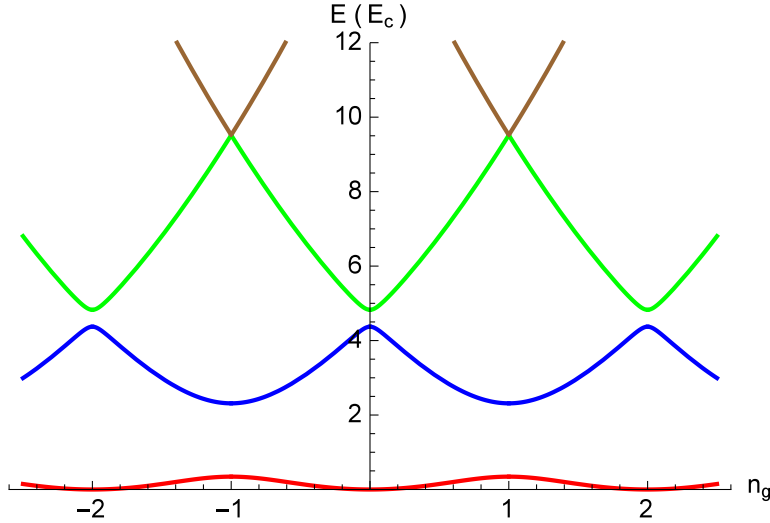


Figure 3.3: The energy levels of the CPB where $E_J = E_c$. Here, the system is largely anharmonic and the energy transitions depend on the gate charge.

3.1.5 Transmon qubit limit of the CPB

Now that I solved the CPB eigenenergies in terms of E_J , E_c and n_g , I investigate the eigenenergy values. Specifically, I look at an eigenenergy's charge dependence and anharmonicity for a variety of values of E_J/E_c . I find that as the ratio of E_J/E_c increases, the energy levels become less anharmonic, and depend less on the value of gate charge n_g . In particular, I find that the charge dependence falls faster than the anharmonicity. The relative reductions allow for a parameter regime ($E_J/E_c \approx 50$) where the charge dispersion is effectively eliminated, while some anharmonicity remains. A CPB in this regime is called a transmon qubit [57].

From the CPB solution (Eqn. 3.24), I can write out the energy levels as a function of gate charge for various ratios E_J/E_c . The energy levels are plotted in Fig. 3.3 for a ratio $E_J/E_c = 1$. We see that the energy of the transitions are both anharmonic and depend on the gate charge n_g . For comparison, when $E_J/E_c = 50$ the charge dispersion has completely disappeared as shown in Fig. 3.4. The anharmonicity has decreased, but is still clearly present. For example, using the values for $E_J/E_c = 50$ shown in Fig. 3.4, a charging energy of $E_c = 2\pi \times 0.23$ GHz gives a qubit frequency of $E_{01} = 2\pi \times 4.4$ GHz and have anharmonicity of $E_{12} - E_{01} = \alpha_K = -2\pi \times 0.25$ GHz.

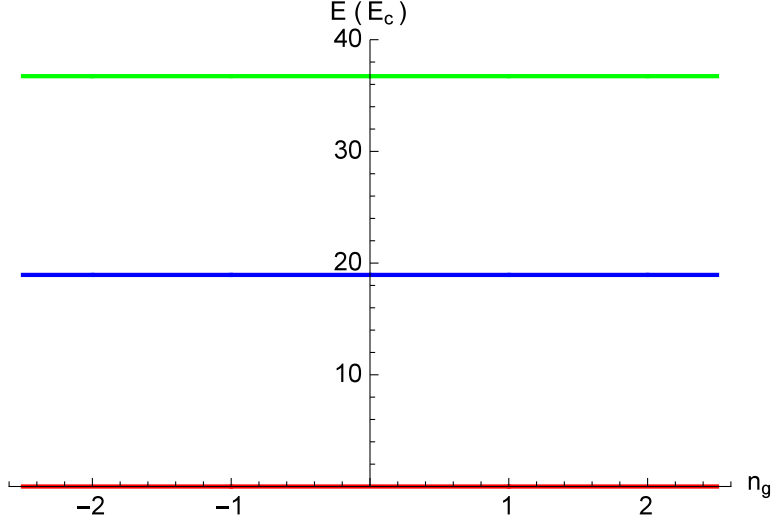


Figure 3.4: The energy levels of the CPB in the transmon limit ($E_J/E_c = 50$). Here, the system is less anharmonic and the energy transitions do not depend on the gate charge.

At this anharmonicity, the system is an effective two level system for dynamics happening slower than characteristic time $\tau = 1/(2\pi|\alpha|) = 0.6$ ns. Because this style of qubit is insensitive to charge, it does not dephase in the presence of charge noise. Considering these advantages, I use a transmon style qubit in my qubit-cavity system.

For all values of the charging energy E_c and Josephson energy E_J , I can use the Mathieu characteristic value $a_\nu(q)$ (Eqn. 3.24), to calculate the qubit frequency and anharmonicity. To avoid calculations using Mathieu characteristic value, I list some approximations from Refs [57, 58]. In the transmon limit, the anharmonicity is approximated by the charging energy

$$\alpha_K \simeq -E_c. \quad (3.25)$$

Also in this limit, the qubit frequency is approximated by the geometric mean of the charging energy and Josephson energy

$$E_{01} \simeq \sqrt{8E_cE_J}. \quad (3.26)$$

3.1.6 Transmon qubit design constraints

Just like the Cooper pair box, the transmon qubit is a nonlinear LC resonator with the nonlinearity arising from a Josephson junction. Since the transmon's large E_J/E_c ratio means it is insensitive to static charge, then the gate is removed to simplify the circuit schematic to just two elements as shown in Fig. 3.5. Here, the capacitor plays two roles: it provides capacitance for the nonlinear LC circuit, and it gives this qubit mode a dipole moment, which allows the qubit to couple to a cavity.

In addition to being a transmon, there are several constraints on the design of the qubit. First, I want the qubit to be compatible with JPAs and other microwave devices that operate in the 4 to 8 GHz range, so

$$2\pi \times 4 \text{ GHz} < E_{01} \simeq \sqrt{8E_c E_J} < 2\pi \times 8 \text{ GHz}. \quad (3.27)$$

Second, I want the performance of the system to be robust to fast dynamics on the order of a nanosecond so,

$$E_c > 2\pi \times 100 \text{ MHz}. \quad (3.28)$$

Third, the values of the charging energy and Josephson energy should be compatible with state of the art qubit fabrication techniques [59]. Lastly, the qubit should be designed with a significant dipole moment so it can be strongly coupled to a cavity. As the qubit is located in a cavity that forms a pristine microwave environment, the dipole only couples to the modes of the cavity and does not radiate into the continuum of free space.

Satisfying all of these constraints, I use a qubit that has $E_c = 2\pi \times 288 \text{ MHz}$ or total capacitance $C_\Sigma = 67 \text{ fF}$ (from Eqn. 3.9). The qubit has a Josephson energy $E_J = 2\pi \times 9.60 \text{ GHz}$ or a critical current $I_0 = 0.019 \mu\text{Amps}$ (from Eqn. 3.2). These values E_J and E_c are determined from the qubit spectroscopy described in Section 4.1.2. This Josephson energy corresponds to a linear inductance of $L_{j0} = 17 \text{ nH}$ (From Eqn. 3.4). From the Mathieu characteristic value $a_\nu(q)$ (Eqn. 3.24), these energies give the qubit a frequency of $E_{01} = 4.4 \text{ GHz} \times 2\pi$, anharmonicity of $\alpha_K = -2\pi \times 350 \text{ MHz}$ and a ratio $E_J/E_c = 33$. Note that $|\alpha_K|$ converges to $-E_c$ in the limit of

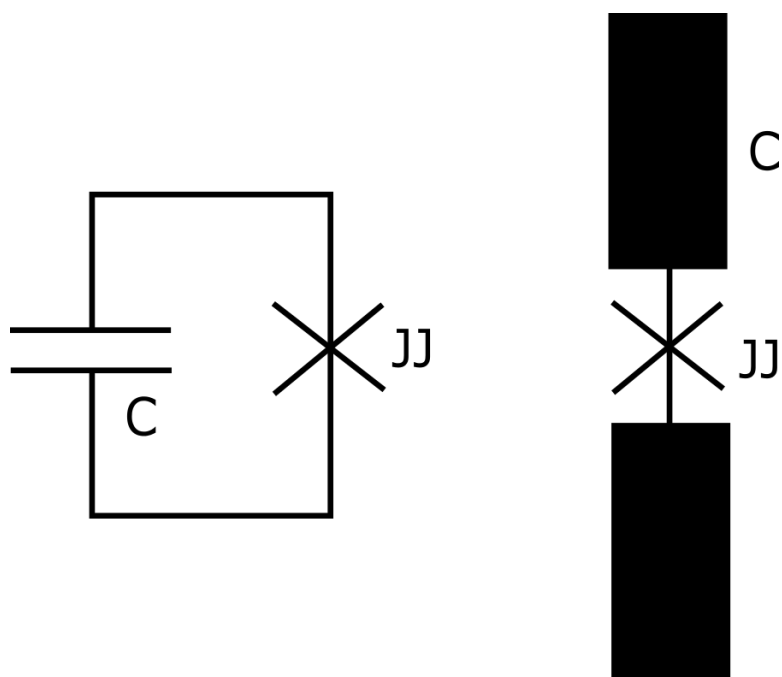


Figure 3.5: The circuit schematic of a transmon qubit.

large E_J/E_c . For the ratio $E_J/E_c = 33$, the Mathieu characteristic values (Eqn. 3.24) are necessary to accurately calculate the transmon transitions.

To achieve these qubit parameters, the qubit is laid out according to Fig. 3.5, with a planar capacitor paddle forming a dipole antenna and a junction in the center. Each half of the paddle is a $400 \mu\text{m}$ by $400 \mu\text{m}$ planar square of conductor forming half of the capacitor. These two halves are separated by $100 \mu\text{m}$. The junction is located along the conductor connecting the two halves of the capacitor. As seen in Eqn. 3.1 and 3.2, an ideal junction is singularly parametrized by the critical current I_0 . In practice, the critical current is determined during fabrication.

3.1.7 Qubit fabrication

The qubit was fabricated and designed by Martin Sandberg in David Pappas' group at NIST Boulder labs. The superconducting qubit is a hybrid TiN/Al design fabricated on high resistivity, intrinsic silicon ($\rho > 20 \text{ k}\Omega\text{-cm}$). The qubit's capacitors are titanium nitride (TiN), which are fabricated from TiN grown on silicon substrates. The growth process results in a buffer region of SiN in between the Si substrate and the titanium nitride which is believed to help suppress undesirable microscopic two level systems at the interface. The only component not made out of TiN is the Josephson junction which is an aluminum-aluminum oxide junction fabricated using shadow evaporation techniques [59].

To make the Josephson junction, two regions of aluminum are overlaid over some junction area with a thin layer of aluminum oxide in between, separating them and forming a tunnel barrier. The junction is formed by depositing a layer of aluminum in vacuum, then oxidizing the aluminum surface by letting oxygen in the vacuum chamber. Lastly, a second layer of aluminum is deposited on top of the first, forming a junction. An image of a 500 by 200 nm Josephson junction fabricated by the author in the JILA Clean Room is shown in Fig 3.6.

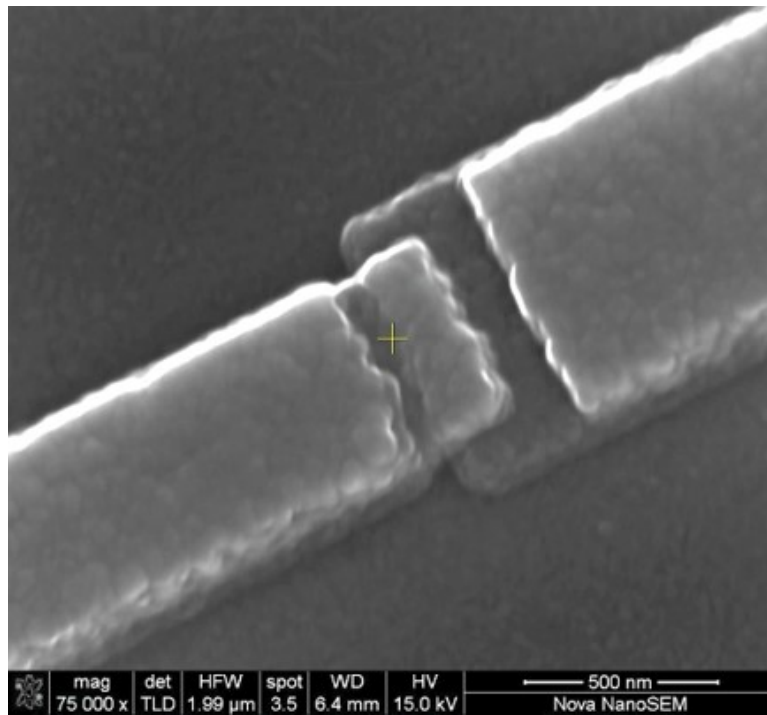


Figure 3.6: The center shows a 500 by 200 nm Josephson junction where two Aluminum layers overlap.

3.2 Cavity

The second element required for the qubit-cavity system is the cavity. In my case, the cavity is a hollow rectangular box with superconducting (Aluminum 6061) boundaries as shown in Fig. 3.7. The cavity has many modes, but I am only interested in coupling to the fundamental mode, while keeping the higher order modes spectrally distant from the qubit, allowing those modes to be ignored.

The cavity is essential for the experiment as it provides inputs and outputs to the system. Moreover, the cavity is critical to itinerant photon generation by providing a temporary mode for the photon and by defining the photon's coupling to the microwave lines which sets the photon's bandwidth. I want to operate the qubit-cavity system in the dispersive regime (Section 2.2.2) so that the qubit can be indirectly measured and controlled, while at the same time, cavity excitations do not cause qubit excitation. This indirect coupling via the cavity isolates the qubit from the continuum of modes in the transmission line. In the dispersive limit, the detuning between the qubit and the cavity is much larger than their coupling. I would like strong coupling ($g \approx 2\pi \times 100$ MHz), therefore the detuning must be $|\Delta| \gg 100$ MHz. Because I know the qubit is at 4.4 GHz, I design the cavity to have a resonance frequency at roughly 5.8 GHz.

3.2.1 Idealized cavity modes

To understand how to design the cavity with the correct resonance frequency and how its fields will couple to the qubit, I analytically solve an idealized model of the cavity that ignores the qubit and the coupling ports. The modes are solutions to the electromagnetic wave equation

$$(\nabla^2 + \mu\epsilon \frac{\partial^2}{\partial t^2})\mathcal{E} = 0, \quad (3.29)$$

where μ is the permeability, ϵ is the permittivity and \mathcal{E} is the electric field. The solutions are subject to boundary condition of a perfect conductor. In other words, the parallel component of the electric field is zero $\mathcal{E}^{\parallel} = 0$ at the boundary of the box cavity. The cavity is aligned in Cartesian coordinates with dimensions l_x , l_y and l_z (for the respective axes) with a corner of the cavity at

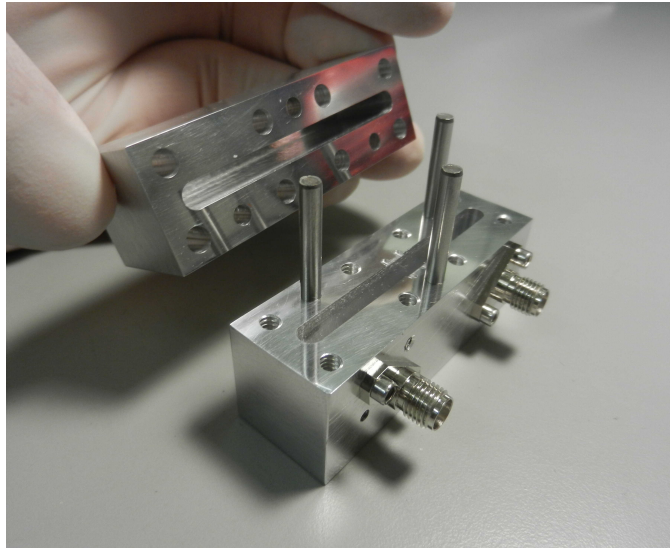


Figure 3.7: An image of the cavity used in the experiment.

the origin. To solve this case, I align the cavity with l_x as the smallest dimension. Because l_x is the smallest dimension, I start by assuming the solutions are separable with the field polarized in the \hat{x} direction. I can write the electric field \mathcal{E} as

$$\mathcal{E} = E_x(x)E_y(y)E_z(z)E_t(t)\hat{x}. \quad (3.30)$$

I solve for \mathcal{E} with perfectly conducting boundaries in planes defined at $x = 0, l_x$, $y = 0, l_y$ and $z = 0, l_z$. Solving Eqn. 3.29 for \mathcal{E} , I get the \hat{x} polarized solutions:

$$\mathcal{E} = \tilde{\mathcal{E}}_0 \cos\left(\frac{m_x\pi}{l_x}x\right) \sin\left(\frac{m_y\pi}{l_y}y\right) \sin\left(\frac{m_z\pi}{l_z}z\right) e^{-i\omega t}\hat{x}, \quad (3.31)$$

where

$$\omega = c\pi \sqrt{\left(\frac{m_x}{l_x}\right)^2 + \left(\frac{m_y}{l_y}\right)^2 + \left(\frac{m_z}{l_z}\right)^2}. \quad (3.32)$$

Here, c is the speed of light, and m_x , m_y and m_z are indices. The indices m_y and m_z are integers ≥ 1 , and the index m_x is an integer ≥ 0 . Using these indices, the modes are labeled $E_{m_x m_y m_z}$. The fundamental mode is TE₀₁₁ and has frequency

$$\omega_{011} = c\pi \sqrt{\left(\frac{1}{l_y}\right)^2 + \left(\frac{1}{l_z}\right)^2}. \quad (3.33)$$

The cavity used in the experiment and shown in Fig. 3.7. has $l_x = 4.0$ mm (0.157"), $l_y = 48.26$ mm (1.90") and $l_z = 28.85$ mm (1.136"). According to this simplified model that ignores the qubit, $\omega_{011} = 2\pi \times 6.057$ GHz. From room temperature measurements of the cavity without the qubit chip, the cavity resonance is $\omega_{011} = 2\pi \times 6.052$ GHz. I use this fundamental mode to couple to the qubit. According to Eqn. 3.31, the fundamental mode is polarized in the narrow (\hat{x}) dimension and has no variation across that dimension. Because I want to couple the qubit as a dipole to the cavity's electric field, I align the qubit's dipole moment with the electric field (\hat{x}) to maximize the coupling. In the y and z dimensions (the two larger ones of the cavity), the field is maximum at the center and vanishes at the edges. Accordingly, I place the qubit in the center of the cavity in the y - z plane to maximize the qubit-cavity coupling.

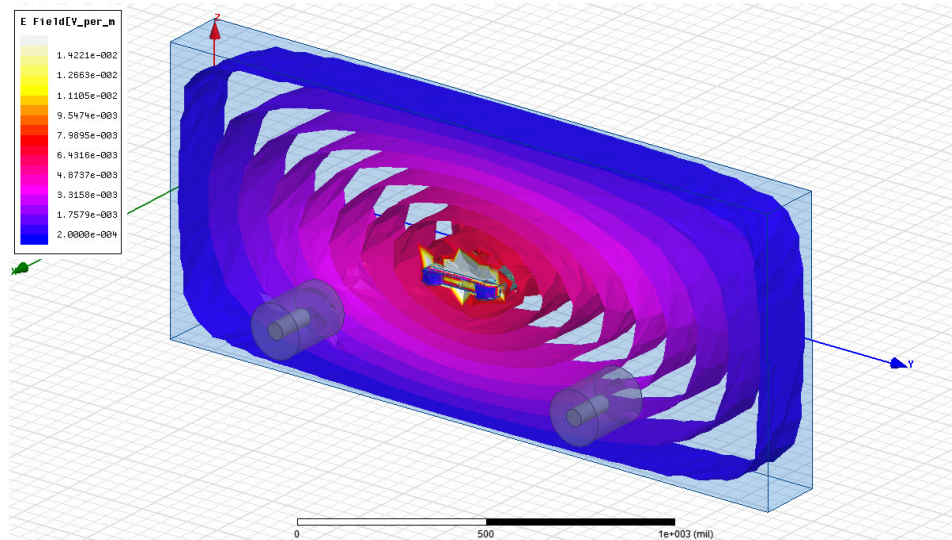


Figure 3.8: The TE₀₁₁ mode of a cavity. The equipotential contours of the mode are shown.

3.2.2 HFSS calculation of cavity modes

The exact solution of an ideal cavity works well for describing an empty cavity, but a more sophisticated method is needed to account for qubit and coupler perturbations. A 3D high frequency field solver called HFSS is used to calculate the modes in this more realistic case. The electric field contours of fundamental mode TE₀₁₁ is shown in Fig. 3.8.

3.2.3 Cavity fabrication

The cavity is formed by milling out two pieces of Aluminum 6061 which are shown in Fig. 3.7. The two halves come together at a seam defined by the plane of the qubit chip. The cavity used in this experiment was machined by the author in the JILA Staff Shop. The cavity includes a slot used to hold the qubit chip in its center along with openings to mount couplers.

3.2.4 Cavity input and output coupling

I add two couplers to create an input and an output. The combination of both allows for transmission spectroscopy of the system and readout of the qubit state. The input coupler allows an input drive to control the dynamics of the qubit-cavity system. Of critical importance, the

output coupler facilitates the decay of a cavity photon into the propagating photon I desire. The cavity's decay rate κ sets the bandwidth of the propagating photon, whereas the ratio of output decay rate to total cavity decay rate κ_{out}/κ sets the likelihood the cavity photon decays through the output coupler.

There are several considerations to choosing the output coupling rate. I want the photon bandwidth to be smaller than the JPA's bandwidth of around 1 MHz at around 25 dB of gain. Conversely, I want the coupling to be large enough so that the decay to the output mode is the dominant decay rate. That is, the output coupling rate is much larger than the internal loss rate and input coupling rate. However, the input coupling rate cannot be arbitrarily small because I use this port to control the system. Considering all of these factors, I chose 300 kHz as the target for the output coupling, dominating over the 30 kHz target for the input.

I couple into the cavity by inserting pins into the cavity aligned with the electrical field polarization. For each coupler, its center pin is connected to the center conductor of microwave co-axial cables. The cavity coupling is estimated by HFSS simulations but is set experimentally by adjusting the length of coupling pins until the desired coupling is measured.

In HFSS, I estimate the coupling rate of a cavity (similar to the cavity used in the experiment) to pins connected to a coplanar waveguide. Specifically, I calculate the loss rate of the cavity's eigenmode when the only source of loss is coupling to the transmission line. In this case, the calculated loss rate is the coupling rate. I compute the coupling for a variety of pin lengths to understand how the coupling rate scales. The pins are positioned to match the polarization of the electric field, and 1/4 up the cavity's height l_z and 1/4 across l_y the cavity's width as indicated in Figs 3.7. Thus the coupling is lower than if their couplers were at the field maximum in the center, but should not affect the scaling with pin length. Though the exact value of the coupling depends on the location of the coupler, the scaling with pin length can be applied to many cavity geometries.

The results of the calculation are plotted in Fig. 3.9. Here, positive pin length corresponds to the distance that the pin extends into the cavity. Negative distance corresponds to the distance

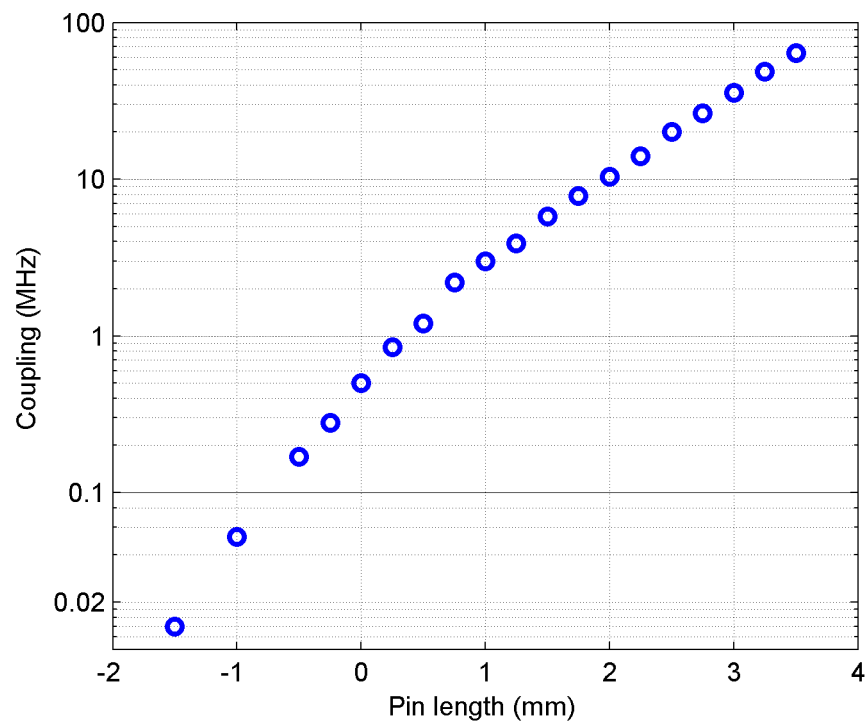


Figure 3.9: Results from an HFSS calculation of the coupling rate for various pin lengths.

the pin is recessed from the cavity's wall. Because I want a strongly coupled output that sets the cavity's decay rate to be in the hundreds of kHz along with a much weaker input, I am interested in the coupling from tens to hundreds of kHz. These couplings correspond to a pin recessed from the cavity wall approximately 0.5 mm to 2.5 mm. In this range of pin length, the coupling scales exponentially with the coupler length by an order of magnitude with every mm of pin length.

Using my knowledge of the coupling's scaling gained from the HFSS calculation, I adopt a procedure where I iteratively measure the coupling rate and adjust the length of the pins. The coupling is determined by measuring the the frequency response in reflection (S_{11}), and then fitting the response in terms of the coupling rate κ_1 and total decay rate κ . For the fit I use

$$|S_{11}|^2 = 1 - \frac{1 - \left(\frac{\kappa - 2\kappa_1}{\kappa}\right)^2}{1 + \left(\frac{2\Delta}{\kappa}\right)^2}, \quad (3.34)$$

where Δ is the detuning from resonance.

Adopting this procedure, I set the output coupling to $\kappa_{out} = 2\pi \times 301$ kHz as shown in Fig. 3.10. From measurements of the cavity when it superconducts, it has a total linewidth $\kappa = 2\pi \times 410$ kHz. Thus, a photon in the cavity decays through the output modes, $\kappa_{out}/\kappa = 73\%$ of the time. The input coupler is measured to be $\kappa_{in} = 2\pi \times 30$ kHz and is located as close to the center of the cavity as possible to maximize the cavity mode coupling to the qubit.

3.3 Coupled system

To complete the qubit-cavity system I couple the qubit to the cavity in the dispersive limit (Section 2.2.2). In this limit, the qubit cavity coupling sets how much the state of the qubit pulls the cavity frequency (2χ in Eqn. 2.37), which is used in qubit readout. Additionally, the it sets the ability to drive the blue sideband which is used to generate photons (Eqn. 2.60). I place the transmon qubit at the center of the cavity so the dipole moment length of the qubit (set by its capacitors) lines up with the polarization of the fundamental mode TE_{011} , thus causing strong dipole coupling. The qubit chip placement is shown in Fig. 3.11.

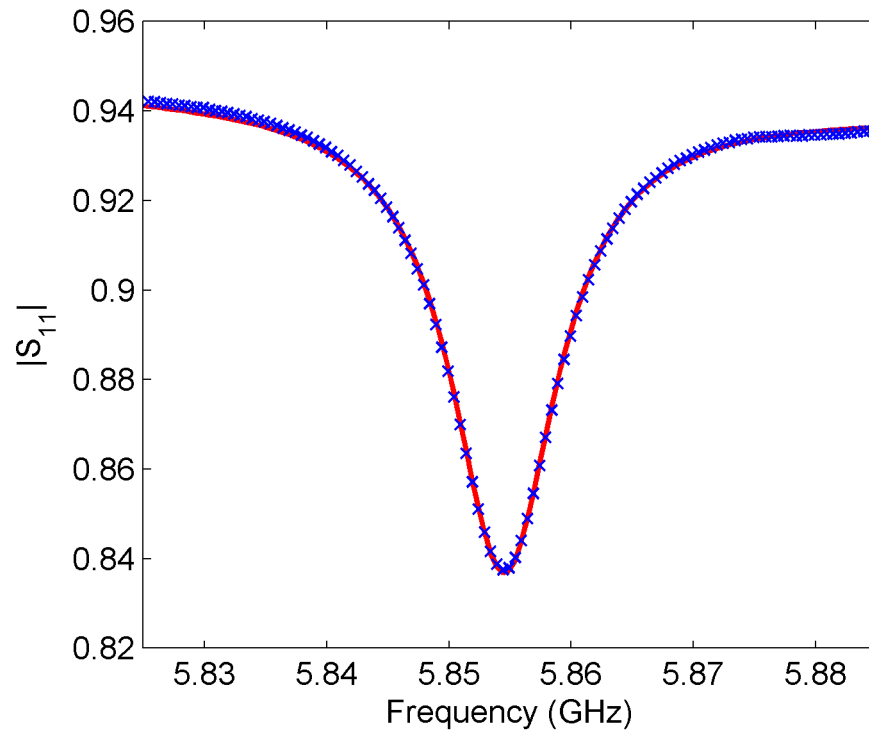


Figure 3.10: The reflection response and fit used in setting the coupling rate κ_1 of the cavity.

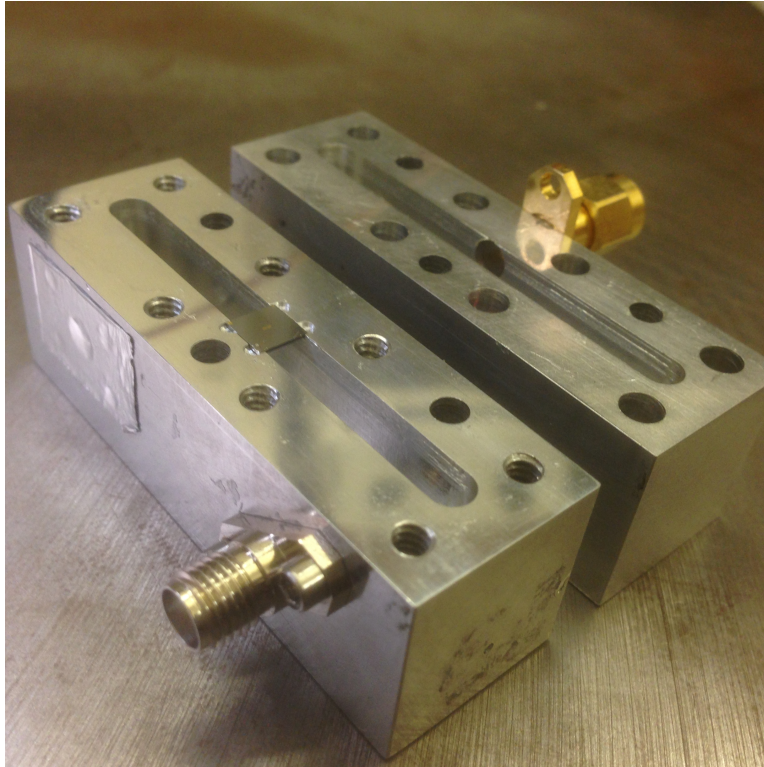


Figure 3.11: The qubit coupled to the cavity by placing it at the center of the cavity.

3.3.1 Effective dispersive Hamiltonian

The coupling of a transmon qubit to a cavity is more complicated than the coupling of a true two level system (as described in Section 2.2) because of the many levels of the transmon. Each of the many transmon energy levels transitions (not just the $|g\rangle$ to $|e\rangle$) couple to the cavity and pull the cavity frequency. Fortunately, it is possible to map the system onto a model based on an ideal two level system (Eqn. 2.38).

To get the mapping, I take the results from Ref. [57], which treat the transmon as a three level system, and ignores the $|g\rangle$ to $|f\rangle$ transition. The mapping to the two level systems model depends on the qubit's coupling of the $|e\rangle$ to $|f\rangle$ transition g_{ef} to the cavity modes, in addition to the coupling of the $|g\rangle$ to $|e\rangle$ transition g_{ge} . The mapping is:

$$\chi = \chi_{ge} - \chi_{ef}/2, \quad (3.35)$$

for effective dispersive shift χ due to

$$\chi_{ij} = \frac{g_{ij}^2}{\omega_{ij} - \omega_c}, \quad (3.36)$$

qubit transitions ω_{ij} , coupling g_{ij} and shifted cavity frequency

$$\omega_c = \omega_{c0} - \chi_{ef}/2, \quad (3.37)$$

where ω_{c0} is the undressed cavity frequency. Therefore, χ depends on the two detunings: $(\omega_{ge} - \omega_c)$ and $(\omega_{ef} - \omega_c)$, and the two couplings: g_{ge} and g_{ef} . Because I know the frequencies of the cavity and the qubit's first two transitions, I need to estimate the coupling of the qubit transitions to the cavity to determine the effective dispersive shift of the system (2χ).

3.3.2 Dipole coupling model

The qubit couples to the cavity as an electric dipole in the cavity's electric field. I consider a simplified toy model to calculate a simple analytic expression for the coupling. I start by writing

$$g^{\text{toy}} = U_{dipole} = -d \bullet \mathcal{E}_{rms} \quad (3.38)$$

where d is the dipole moment of the qubit and \mathcal{E}_{rms} is the root-mean-squared electric field due to the vacuum state. The dipole moment is specific for each transmon transition leading to distinct coupling energies for each transition. That is g_{ge} and g_{ef} are calculated from d_{ge} and d_{ef} , respectively. I approximate the dipole moment's magnitude by treating the length of the transmon's capacitor paddles l (Section 3.1.6) as the effective length of the dipole. This treatment overestimates the dipole moment because it is only valid for charges at the end of the capacitor, separated by l . In reality there is a distribution of charge along the capacitor, which decreases the dipole coupling. The charge used in the dipole is computed from the transmon's change in charge (which is $2e \times n$ for n Cooper pairs) due to making the transition. Thus, the dipole moment for the i to j transition is

$$d_{ij}^{\text{toy}} = l \langle i | 2e\hat{n} | j \rangle. \quad (3.39)$$

The dipole moment can be solved by taking results from Ref [57],

$$|\langle j+1 | \hat{n} | j \rangle| \approx \sqrt{\frac{j+1}{2}} \left(\frac{E_J}{8E_c} \right)^{1/4} \quad (3.40)$$

for a transmon qubit. I calculate the electric field by setting the time averaged energy stored in the fields equal to the energy of the vacuum state. That is,

$$\frac{1}{2} \hbar \omega_c = \frac{1}{2} \int_V \epsilon \mathcal{E}^2 dV \quad (3.41)$$

where \mathcal{E} is given by Eqn. 3.31 for the TE₀₁₁ mode, and V is the volume of the cavity. Solving this equation, I get the rms value for the electric field at the center of the cavity

$$\mathcal{E}_{rms} = \sqrt{\frac{2\hbar\omega_c}{\epsilon V}}. \quad (3.42)$$

I calculate the dipole coupling (Eqn. 3.38) of the transmon transitions by combining Eqns. 3.39, 3.40 and 3.42. I express the coupling in units of angular frequency by dividing by \hbar . For the qubit transition I get

$$g_{ge}^{\text{toy}} \approx el \sqrt{\frac{\omega}{\hbar \epsilon V}} \left(\frac{2E_J}{E_c} \right)^{1/4}. \quad (3.43)$$

For the next transition I get

$$g_{ef}^{\text{toy}} \approx \sqrt{2} g_{ge}^{\text{toy}}. \quad (3.44)$$

With my system's values ($d = 0.9$ mm, $V = 4.0$ mm \times 48.26 mm \times 28.85 mm, $E_J/E_c = 34$ and $\omega = 2\pi \times 5.8$ GHz) the calculated couplings are $g_{ge}^{\text{toy}} = 2\pi \times 138$ MHz and $g_{ef}^{\text{toy}} = 2\pi \times 195$ MHz. I determine the observed coupling rate from qubit spectroscopy (Section 4.1) getting $g_{ge} = 2\pi \times 82$ MHz and $g_{ef} = 2\pi \times 141$ MHz. As expected, the toy model overestimates the coupling.

Chapter 4

Qubit and cavity's characterization and dynamics

Before I can use the qubit-cavity system to produce photons, I need to characterize it to determine if it is suitable for photon generation. Additionally, I need to demonstrate and calibrate operations, which control the dynamics of the system in order to implement a photon generation protocol. Both fully characterizing the system and calibrating control operations depend on reading out the state of the qubit. To begin, I perform a power dependent spectroscopy on the cavity. This spectroscopy lets me calculate some of the system parameter, and form the basis of qubit readout. With the qubit readout, I can further characterize the system and calibrate control pulses.

4.1 Cavity spectroscopy and qubit readout

As the starting point for understanding the system, I look at the cavity's power dependent spectrum. From this spectrum, I can confirm that I have an effective two level system dispersively coupled to the cavity. Additionally, I can determine the terms in the system's effective dispersive Hamiltonian (Eqn. 2.38), which forms the basis for measuring and projecting the state of qubit.

As shown in Fig. 4.1, I inject a probe tone into the cavity and measure the transmitted probe's amplitude with the amplifier chain. Because the cavity acts as a filter, I see a peak in transmission at the cavity's resonance. By adjusting the power and frequency of the probe tone, we see the cavity resonance corresponding to the $|g\rangle$, $|e\rangle$ and $|f\rangle$ states of the transmon and the power dependence of the cavity frequency (Fig. 4.2). The spectrum is plotted as the scattering parameter $S_{21} = V_{out}/V_{in}$ in terms of the injected V_{in} and measured voltages V_{out} . If we ignore the faint $|f\rangle$

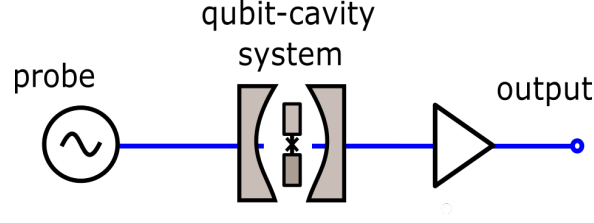


Figure 4.1: Transmission spectroscopy schematic. The cavity has two ports. I inject a coherent tone in one port and measure the transmitted tone with the second port.

state, at low power the system is well described by the dispersive Hamiltonian (Eqn. 2.38), which describes a cavity frequency that depends on the state of a two level system. From rearranging the terms in Eqn. 2.38, I get the effective cavity frequency in terms of the qubit state as

$$\omega'_c = \omega_c + 2\chi \frac{\sigma_z}{2}. \quad (4.1)$$

From the figure, the system has a dispersive shift of $\chi = -2\pi \times 1.0$ MHz and $\omega_c = 2\pi \times 5.866$ GHz.

The dispersive Hamiltonian considers a two level system coupled to a cavity. In reality, I have at least a three level system where I treat the $|g\rangle$ and $|e\rangle$ states as forming a two level system. The presence of the three levels shifts the cavity frequency from the undressed cavity $f_0 = 5.8655$ GHz at high power to the dressed cavity $f_c = 5.8705$ GHz at lower power. Moreover, the effective dispersive shift 2χ , is set by the parameters of the three level system coupled to the cavity as I described in Section 3.3.1 in Eqns. 3.35, 3.36 and 3.37. I can account for the cavity dressing and effective dispersive shift by writing out

$$\chi = \frac{g_{ge}^2}{\omega_{ge} - \omega_c} - \frac{g_{ef}^2}{2(\omega_{ef} - \omega_c)} = -2\pi \times 1.0\text{MHz}, \quad (4.2)$$

and

$$\Delta\omega_c = -\frac{g_{ef}^2}{2(\omega_{ef} - \omega_c)} = 2\pi \times 5.5\text{MHz} \quad (4.3)$$

in terms of the three level system (transmon) parameters. In order to solve for all of the dispersive three level system parameter described in Eqns. 4.2 and 4.3, I need to implement a more sophisticated spectroscopy to determine the qubit frequency and anharmonicity. Once I have these values, I can use these relation to determine the qubit-cavity couplings (g_{ge} and g_{ef}).

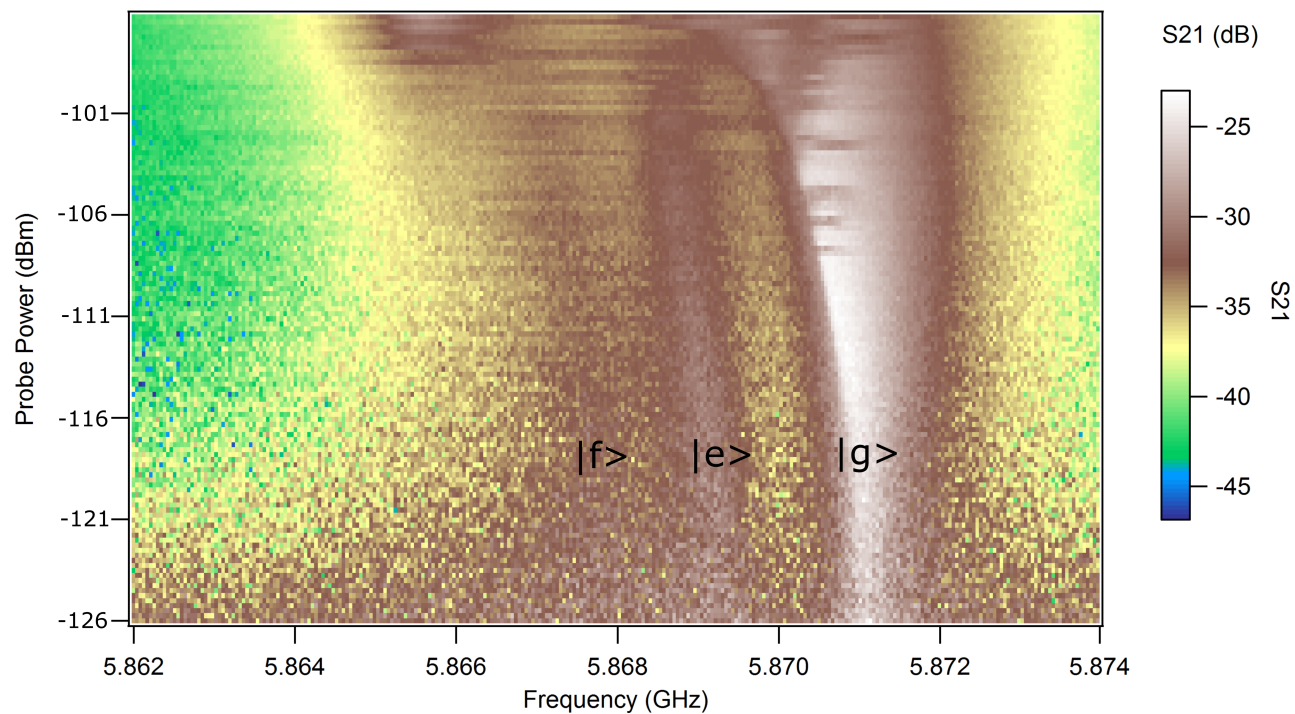


Figure 4.2: The power dependent cavity spectra. The cavity transmission is measured adjusting a CW probe tone's frequency and powers. The probe tone's power is listed as the approximately power at the cavity's input. Low power shows the dispersive shift of the cavity frequency depending on the state of the transmon. Because the transmon is not well thermalized, the $|f\rangle$ states resonate frequency is visible in addition to the $|g\rangle$ and $|e\rangle$ states. At high power, undressed cavity resonance $f_0 = 5.8655$ GHz is visible.

4.1.1 Qubit readout

There are two types of qubit readouts I can implement based on the power dependent cavity spectrum. One is based on the cavity's dispersive shift [60]. The second is based on the transmon's three levels altering the cavity frequency. From the dispersive Hamiltonian, the cavity has one of two frequencies depending on the state of the qubit (Eqn. 4.1). Because the resonance frequency of the cavity is determined by the state of the qubit, measuring the resonance frequency of the cavity, in effect, measures the state of the qubit. I can use a single tone to measure the cavity's resonance frequency either as a transmission amplitude measurement or phase measurement, depending on the frequency of the readout signal [21, 61].

In transmission dispersive measurement, I place a readout tone at one of the cavity's resonance states. Then, the readout tone will be on resonance (and thus transmit) depending on the state of the qubit. For example, if a readout tone is injected at the cavity's excited state resonance frequency, then it will transmit only if the qubit is in the excited state. If the qubit is in the ground state or any other higher level transmon state, then the tone will not transmit. Thus, I realize a qubit readout by measuring the transmission of the injected tone. Likewise, by injecting the readout tone at the ground state, I can make a measurement that is dependent on the population of the ground state.

Alternatively, I can measure the phase shift of the probe tone in order to measure the cavity's resonance frequency, and thus infer the state of the qubit. By placing a tone in between the two resonant states of the cavity, the phase of the tone is determined by whether the tone is above or below the cavity's resonant state determined by the qubit. Therefore, by measuring the phase of the probe tone, I measure the state of the qubit [62, 31, 32, 63]. In this case (where the dispersive shift is much greater than the cavity decay rate $|2\chi| \gg \kappa$ and $\chi < 0$) if the qubit is in the $|g\rangle$ state, then the tone is below resonance and there is approximately no phase shift. When the qubit is in the $|e\rangle$ state, the tone is above resonance and there is approximately a π phase shift. By constructing the measurement so that I am sensitive to this π phase shift in the probe tone, I can

realize a qubit readout.

As an alternative to the dispersive readout, I can form a measurement based on whether the qubit dresses (shift) the bare frequency of the cavity. As seen from the spectroscopy (Fig. 4.2) the bare frequency of the cavity emerges at 5.8655 GHz when the probe tone is greater than -97 dBm at the cavity's input. Whereas, at lower power the cavity has a frequency $f_c \pm \chi/2\pi = 5.8705 \pm 0.001$ GHz. It turns out that the presences of the undressed cavity state depends on both the readout tone's power and qubit state. When the qubit is in the $|e\rangle$ state, the undressed cavity emerges at a higher power than when the qubit is in the $|g\rangle$ state. I realize an undressed cavity readout by first setting the readout tone at the undressed cavity state frequency. Second, I set the power so that the cavity will not transmit if the qubit is in the ground state, and will transmit if the qubit is in the excited state, or bright state. Thus, I have realized an additional readout called the bright state readout [64].

The readout can either measure an instantaneous realization of the state of the qubit or average over multiple realizations depending on the duration of the measurement compared to the qubit's lifetime. When performing a measurement much longer than the lifetime of the qubit, the measurement reflects the average state of the qubit over the duration of the measurement rather than at any single instance. This type of measurement is called continuous wave (CW) measurement. When the measurement is shorter than the lifetime of the qubit and each measurement distinguishes the qubit (or cavity) state, then measurement reflects the instantaneous state of the qubit and is called single shot readout.

4.1.2 Two-tone spectroscopy of the qubit

To detect the qubit transitions, I perform a type of spectroscopy where I use one tone to excite the qubit and the second to detect the change in the qubit state (Fig. 4.3). The readout tone is tuned to the undressed cavity resonance frequency (bright state), which transmits power when the qubit is excited (Section 4.1.1). I sweep the frequency and power of the other tone, drive tone, to detect the qubit transition. I perform this two-tone spectroscopy in CW mode. Because

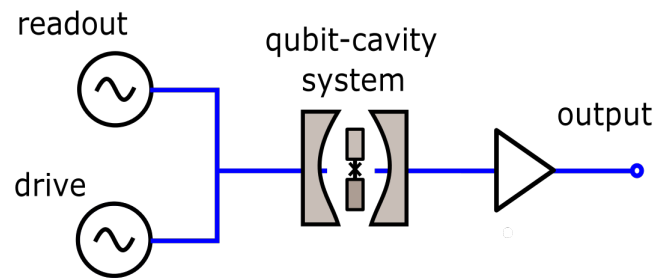


Figure 4.3: Two-tone spectroscopy schematic. Like the transmission spectroscopy, I inject power in one port and measure the transmission with the second port. In addition to the readout tone, I inject a drive tone to excite the qubit.

I am performing a CW measurement, transmission increases according to the probability that the qubit is in the excited state. When the drive tone is at the qubit transition, then the qubit will oscillate the excited and ground state. If the rate of oscillations, or Rabi rate, is much larger than the qubit decay rate, then the qubit will be excited half of the time and I will see a larger signal. If I decrease the Rabi rate (amplitude of the drive tone) to be comparable to or less than the qubit decay rate, then the excited state probability decreases with the Rabi rate (Section 2.2.3.1), and I see a decrease of signal with drive amplitude.

The results of the two-tone spectroscopy are shown in Fig. 4.4. I use a poorly thermalized cavity different from the one used in photon generation. I see an increased transmission of the readout tone when the drive is at 4.37 GHz. Thus, the qubit frequency is $f_{ge} = 4.37$ GHz. Because the qubit is poorly thermalized, we can see the $|e\rangle$ to $|f\rangle$ transition. The poorly thermalized transmon has a non-negligible probability of being in the $|e\rangle$ state $P_e \approx 15\%$. If the transmon is in the $|e\rangle$, then driving the the $|e\rangle$ to $|f\rangle$ transition populates the $|f\rangle$ state, and thereby increase the time it takes to decay down to the $|g\rangle$ state. As a consequence, driving the $|e\rangle$ to $|f\rangle$ transition decreases the probability of being in the $|g\rangle$ state and therefore increases the signal transmission. From this spectroscopy, we see that the $|e\rangle$ to $|f\rangle$ transition is at $f_{ef} = 4.04$ GHz. Using the spectroscopy with the cavity used in the experiment, the qubit frequency is determined to be $f_{ge} = 4.398$ GHz and the $|e\rangle$ to $|f\rangle$ transmission is $f_{ef} = 4.052$ GHz. These frequencies give a measurement of anharmonicity $\alpha_k = \omega_{ge} - \omega_{ef} = -2\pi \times 346$ MHz.

I can use the results of the two-tone spectroscopy to finish solving for the dispersive transmon parameters and the solve for the E_c and E_J in the CPB Hamiltonian. Combining the results of the qubit, two-tone spectroscopy with power dependent cavity spectra earlier in this section, I can solve for the cavity coupling to the $|g\rangle$ to $|e\rangle$ transition g_{ge} and the coupling to the $|e\rangle$ to $|f\rangle$ transition g_{ef} . From Eqns. 4.2 and 4.3, I find $g_{ge} = 2\pi \times 82$ MHz and $g_{ef} = 2\pi \times 141$ MHz.

Using the solution for the transmon qubit in terms of the Mathieu characteristic function (Eqn. 3.24) I solve for the values of E_J and E_c . From $f_q = 4.398$ GHz and $f_{ef} = 4.052$ GHz and

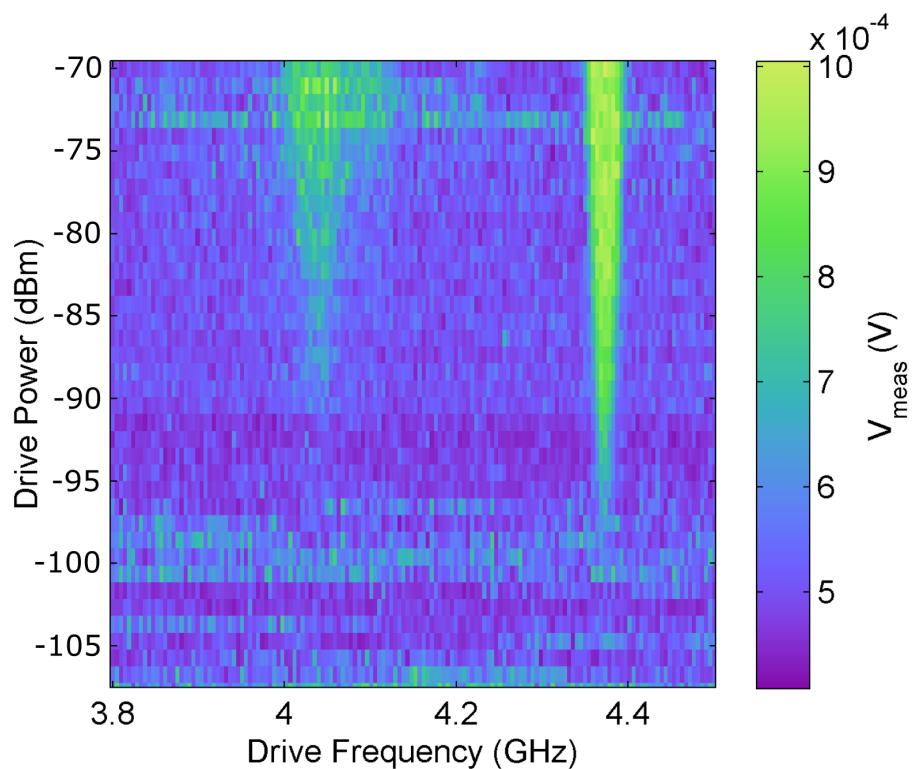


Figure 4.4: Two-tone spectroscopy on the state of the qubit. The transmission of the readout tone is measured while adjusting the frequency and power of a drive tone. The drive power is specified at the microwave source. From the spectrum, I see $f_q = 4.37$ GHz and $f_{ef} = 4.052$ GHz.

assuming negligible charge dispersion, I numerically solve for E_J and E_c by minimizing

$$\mathcal{J} = \left[E_c a_{-3} \left(-\frac{E_J}{2E_c} \right) - E_c a_{-1} \left(-\frac{E_J}{2E_c} \right) - \omega_{ge} \right]^2 + \left[E_c a_{-5} \left(-\frac{E_J}{2E_c} \right) - E_c a_{-3} \left(-\frac{E_J}{2E_c} \right) - \omega_{ef} \right]^2 \quad (4.4)$$

from Eqn. 3.24. Because the transmon is insensitive to n_g , an arbitrarily chosen $n_g = 0.5$ is used. I get $E_J = 2\pi \times 9.60$ GHz and $E_c = 2\pi \times 288$ MHz. These values give us a ratio $E_J/E_c = 33.2$, which is below the ideal transmon ratio of 50. As we see later in this Chapter, these values still give us a lifetime and dephasing rate suitable for photon generation.

4.1.3 Single shot readout

For two reasons the photon generation protocol benefits greatly from single-shot QND readout. First, single shot readout has the greatest possible readout contrast facilitating the calibration qubit control pulses with high accuracy. Second, a QND measurement projects the system into the measured state, allowing the system to be prepared in the ground state by measurement and post-selection [65, 66, 67].

Single shot readout can be achieved when the readout's duration is less than the lifetime of the qubit, and has the contrast to resolve the two states of the qubit. Given a certain cavity response depending on the state of the qubit, these requirements place joint constraints on the qubit lifetime, probe power and measurement efficiency. I can demonstrate the conditions used to achieve single shot readout by measuring a qubit that has a steady state excited state probability. The measurement is an excited state transmission measurement. The qubit measurement is pulsed for 1 μ s, and a JPA is used as a homodyne detector that measures a single quadrature value. As shown in Fig. 4.5, I adjust the readout power and plot histograms along the y-axis of single quadrature measurements of the readout tone. At the lowest power, it is impossible to resolve instances that the cavity transmits because the qubit is excited from those instances when the qubit is in the ground state. We see a single Gaussian distribution of measured readout tone values along the y-axis. As the readout tone's power is increased to -125 dBm at the cavity, we can start to resolve a two Gaussian peaks. One corresponds to instances the cavity transmits because the qubit

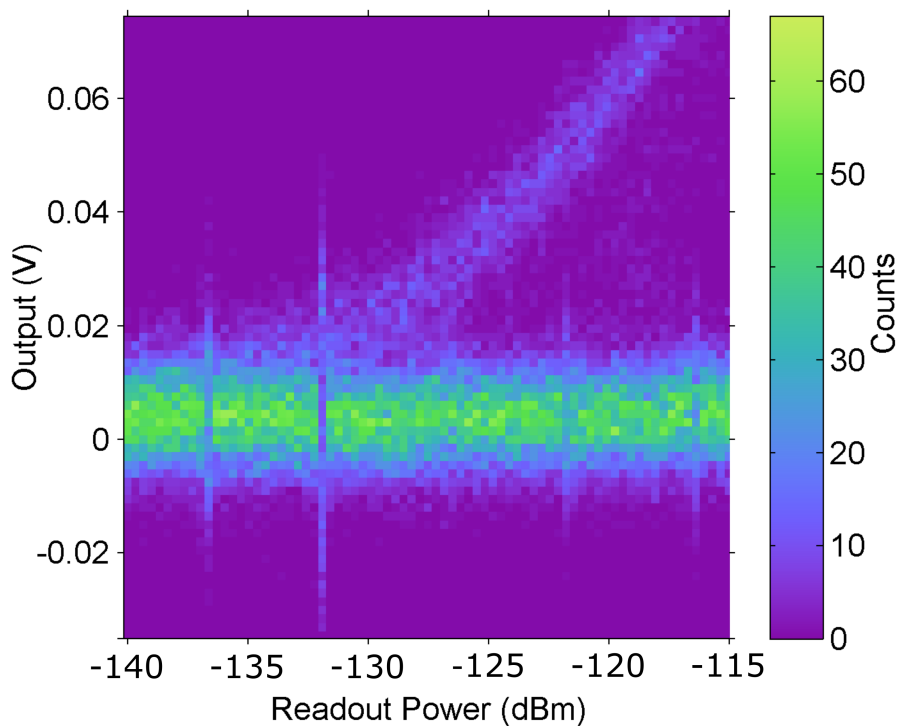


Figure 4.5: Histograms of the measured readout tone's voltage (y-axis) at various readout tone powers (x-axis). At low power these single shot voltages for a Gaussian distribution set by the noise floor of the measurement. Above -125 dBm of readout power at the cavity, we can resolve the transmitted distribution associated with the $|e\rangle$ state apart from the $|g\rangle$ state. By thresholding at a voltage between the two distribution, I can realize single shot readout.

is in the excited state. The other corresponds to instances when the qubit is in the ground state. In the ground state, the cavity does not transmit and we see a Gaussian peak corresponding to the noise floor of the measurement. I can set up a single shot readout of the qubit state by choosing a readout tone power where there are two resolvable distributions and then set a threshold quadrature measurement between the two. If a measurement of the readout tone above the threshold, then I assign that measurement to the $|e\rangle$ state. If below, then the $|g\rangle$ state. The success of the single shot readout is demonstrated in the next section when Rabi oscillations and control pulses are discussed.

4.2 Control pulses

Now that I can perform single shot readout on the state of the qubit, I can observe coherent control of the qubit-cavity system. I demonstrate driving Rabi oscillations, and I calibrate pulses that drive the qubit transition (Section 2.2.3.1), which are used for characterizing the system. Then, I demonstrate driving coherent oscillations on the blue sideband transition (Section 2.2.3.2), which creates photons. Like two-tone spectroscopy (Section 4.1.2), I use both a drive and a readout tone (Fig. 4.3). Rather than operating both the readout and drive tones in CW mode, as for two-tone spectroscopy, I sequentially pulse the two tones. First, I pulse the drive tone at a particular frequency and amplitude for a set amount of time. Then, I pulse the readout tone to perform the single shot on the qubit.

4.2.1 Qubit pulse

Driving the qubit transition creates oscillations between the ground and excited state (Rabi oscillations). This is a direct demonstration that our system is a controllable effective two level system. Moreover, the drive on the qubit allows preparation of the qubit into arbitrary states and can facilitate measurements of the qubit's lifetime T_1 and dephasing time T_2 . When I drive the qubit transition, the qubit state will oscillate between ground state $|g\rangle$ and excited state $|e\rangle$ [62]. Starting in the ground state, the excited state probability after being driven for a time t_d oscillates

according to

$$P_e(t_d) = \frac{V_d^2}{\Delta^2 + V_d^2} \sin^2 \left(\frac{t_d \sqrt{\Delta^2 + V_d^2}}{2} \right) \quad (4.5)$$

from Eqn. 2.46, where Δ is the drive's detuning from the qubit transition and V_d is the amplitude of the drive.

I demonstrate these Rabi oscillations by repeating a protocol where I first drive the qubit for a certain amount of time with a certain power and then, perform a single shot readout. After the measurement, I wait for the qubit to relax before starting the protocol again. I repeat this protocol 640 times at each power and time to measure the probability of the qubit being in the excited state (Fig. 4.6). I see P_e oscillate according to Eqn. 4.5. Observing Rabi oscillations confirms the frequency of the qubit transition and is a clear demonstration that I am controlling an effective two level system.

4.2.1.1 Calibrating pulses

By measuring these oscillations I can calibrate pulses. A pulse which lasts for half the period of a Rabi oscillation swaps the qubit state from $|g\rangle$ to $|e\rangle$, or $|e\rangle$ to $|g\rangle$. This pulse is called a π pulse because it constitutes π radians worth of Rabi oscillations. A control pulse lasting for $\pi/2$ radians worth of Rabi oscillations is call a $\pi/2$ pulse and pulse will turn a $|g\rangle$ into a $(|g\rangle + e^{i\phi} |e\rangle)/\sqrt{2}$ state with the phase ϕ set by the phase of the pulse.

From a plot of Rabi oscillations similar to Fig. 4.6, I can calibrate a π -pulse by choosing the duration and amplitude that maximizes the swap of the first oscillation. Similarly, I can calibrate a $\pi/2$ -pulse, by keeping that same frequency and choosing the duration such that half the population has swapped. These pulses are important tools because both π and $\pi/2$ -pulses on the qubit are used to characterize the qubit's lifetime and dephasing. Furthermore, π -pulses on both the qubit and blue sideband transition are used to in the photon creation protocol.

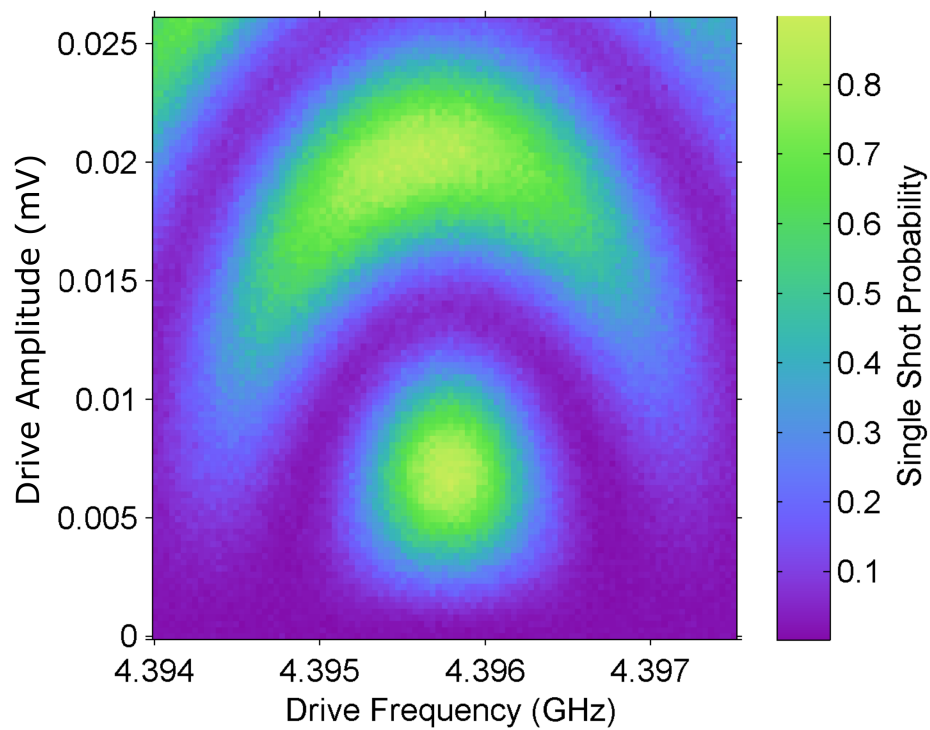


Figure 4.6: The results from the Rabi measurement adjusting pulse amplitude and frequency. The pulse amplitude is specified at the microwave source. Rabi oscillations can be seen at the qubit transition.

4.2.2 Blue sideband pulse

Pulses on the blue sideband are used to create photons in the cavity, and are therefore critical to the photon generation experiment. As we saw in section 2.2.3.2, when I drive the qubit cavity system at $(f_q + f_c)/2$ I get the effective Hamiltonian for the blue sideband drive that couples the $|N, g\rangle$ state and the $|N + 1, e\rangle$ state. (The notation convention is |cavity photon number, qubit state>). Because of this coupling, a drive on the blue sideband will cause oscillations between the $|N, g\rangle$ and $|N + 1, e\rangle$ state. These oscillations are analogous to Rabi oscillations between the $|g\rangle$ and $|e\rangle$ states for the qubit drive.

I demonstrate these oscillations by using an identical protocol to the Rabi oscillations in the previous subsection (4.2.1). Starting in the ground state with no photons in the cavity, the system oscillates between the $|0, g\rangle$ and $|1, e\rangle$ states. I can therefore perform a single shot readout on the state of the qubit to see the blue sideband oscillations. I adjust the drive frequency and amplitude to see Rabi like oscillation in Fig. 4.7. Additionally, I see a drive amplitude dependent shift in the blue sideband frequency. It arises because I populate the cavity with photons and Stark shift the qubit frequency as seen in the dispersive Hamiltonian (Eqn. 2.38). Because the blue sideband frequency depends on the frequency of the qubit [$f_{bs} = (f_q + f_c)/2$], the blue sideband transition Stark shifts along with the qubit.

The oscillations become more clearly similar to Rabi oscillation by fixing the amplitude of the drive and adjusting both the frequency and duration of the drive (Fig 4.8). In a similar manner to the previous section, I can define and calibrate a π pulse on the blue sideband. Starting in the ground state of the system $|0, g\rangle$, this blue sideband π pulse will create a photon, putting the system in the $|1, e\rangle$ state. Thus, the blue sideband π pulse creates a single photon while exciting the qubit.

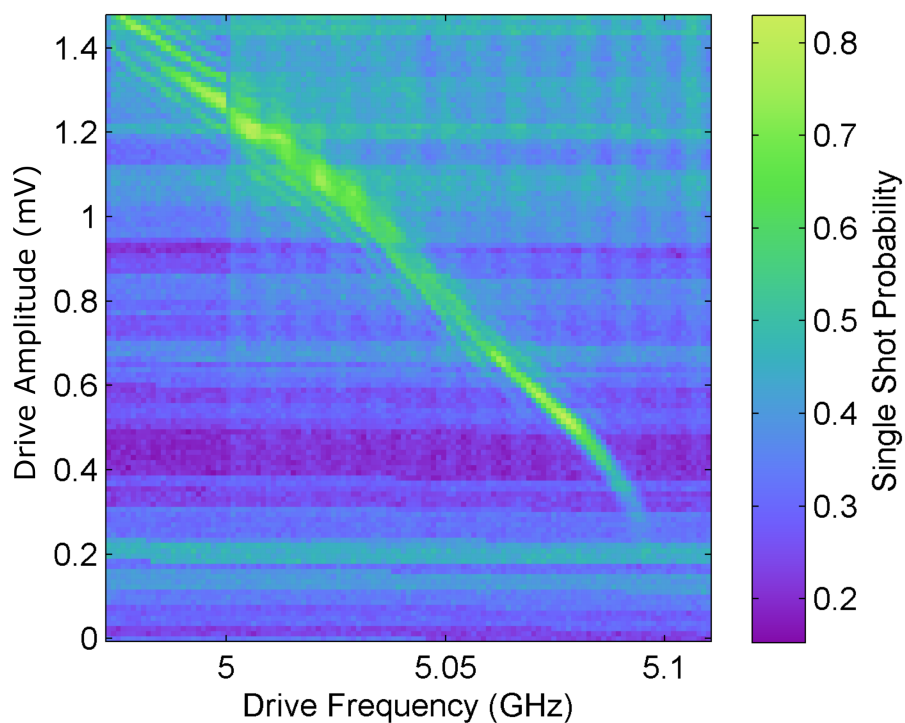


Figure 4.7: The results of the blue sideband measurement, as a function of pulse amplitude and frequency. The pulse amplitude is specified at the microwave source. Rabi-like oscillations can be seen at the blue sideband transition frequency. These oscillations are distorted by the power dependence of the blue sideband transition, or Stark shift.

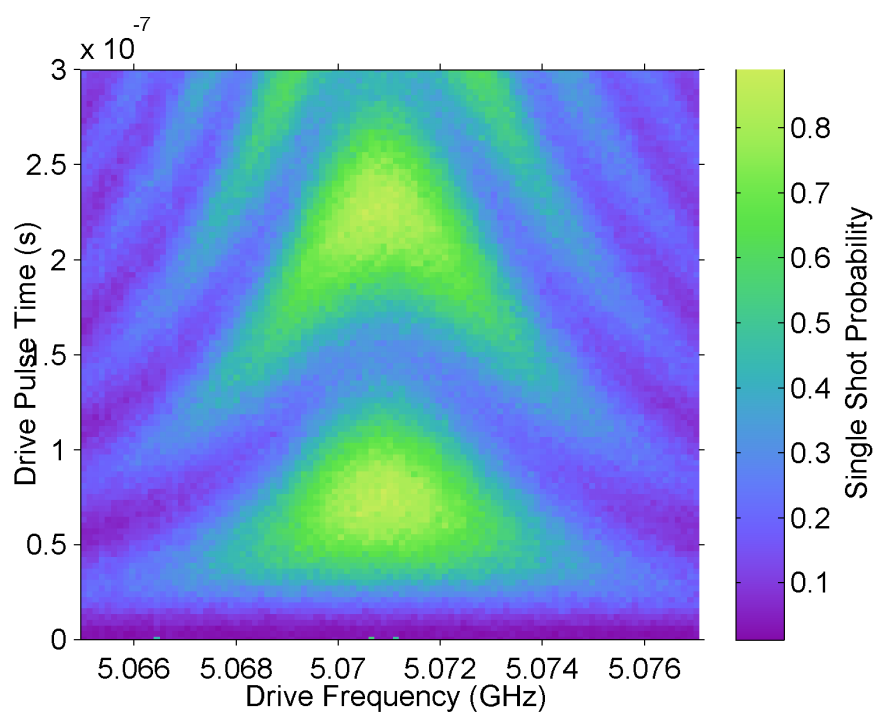


Figure 4.8: The results from the blue sideband measurement with fixed pulse amplitude. I adjust pulse duration and frequency seeing Rabi-like oscillations at the blue sideband transition frequency.

4.3 Qubit characterization

Combining the calibrated drive pulses with the single shot readout, I can implement protocols that determine the lifetime T_1 and dephasing time T_2 of the qubit. The lifetime is the characteristic time for the qubit to decay from the $|e\rangle$ state to the $|g\rangle$ state. The dephasing rate $\Gamma = 1/T_2$ describes how fast the phase ϕ in $|g\rangle + e^{i\phi}|e\rangle$ is lost. These parameters must be sufficiently large for a successful implementation of the photon generation protocol.

The photon creation protocol places constraints on the lifetime of the qubit T_1 because it relies on a blue sideband π pulse. When I create a photon in the cavity with a blue sideband, I also excite the qubit. Changing the state of the qubit changes the frequency of the cavity and its excitations due to the dispersive Hamiltonian. Because I do not want the photon frequency to change, I want the qubit to stay in the $|e\rangle$ state until the photon has decayed out of the cavity. As a result, I want the qubit to have a lifetime that is much longer than the cavity decay time $T_1 \gg 1/\kappa$. For the system $\kappa = 2\pi \times 410$ kHz, therefore I desire $T_1 \gg 0.39 \mu\text{s}$.

The dephasing time is another important characteristic of the qubit. The dephasing time T_2 must be much longer than the duration of any control operation on the qubit for that operation to have high fidelity. For the 150 ns pulse length I implement in the photon generation experiment, $T_2 \gg 0.15 \mu\text{s}$ is necessary for the qubit's phase to be well defined over the duration of the qubit pulse. Additionally, determining T_2 is important in the photon generation experiment, because I use the change in the dephasing time to quantify measurement backaction.

4.3.1 Qubit lifetime

I can measure the lifetime T_1 of the qubit by implementing a three-step protocol. Starting in the $|g\rangle$ state, the protocol begins by first exciting the qubit with a π pulse. Then, I wait some time t_w before I perform single shot readout on the state of the qubit. By repeating this protocol several times at each t_w , I extract the probability that the qubit is in the excited state. By measuring this probability over a range of wait times, we can see the probability that the qubit is in the

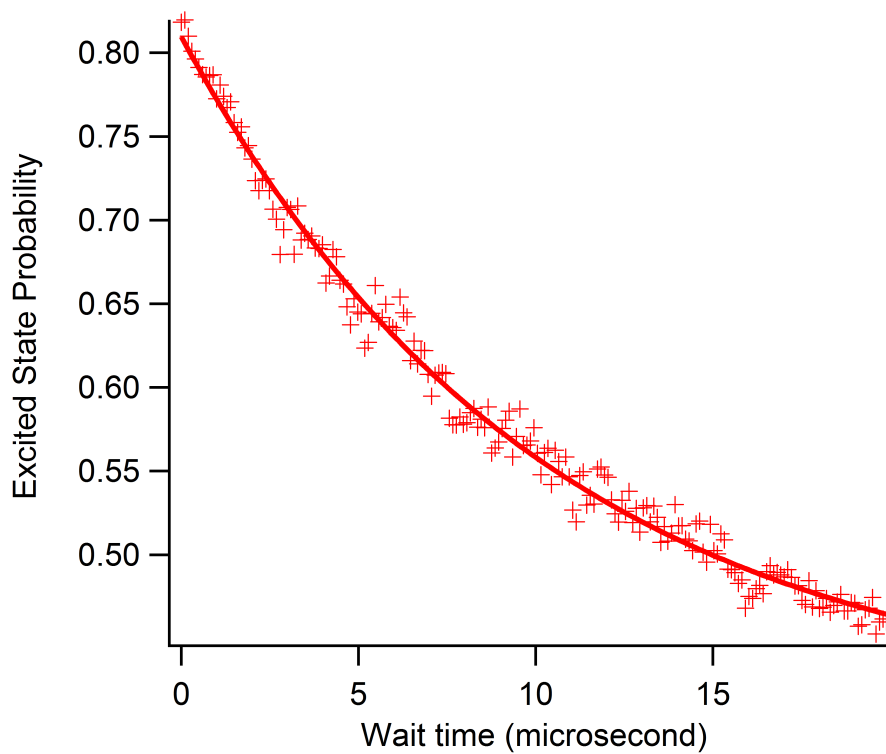


Figure 4.9: Measurement of the qubit $|e\rangle$ state lifetime. I excite the qubit and observe it decay. From the fit, the qubit lifetime is $T_1 = 10.2 \pm 0.3 \mu\text{s}$.

excited state P_e decays over time. By fitting the decaying excited state probability to a decaying exponential

$$P_e(t_w) = P_e(0)e^{-t_w/T_1}, \quad (4.6)$$

I can extract the lifetime T_1 for the qubit [68]. I implement this T_1 measurement (Fig. 4.9). From fitting the excited state probability to Eqn. 4.6, I get a qubit lifetime $T_1 = 10.2 \pm 0.3 \mu\text{s}$. Indeed, $T_1 \gg 0.39 \mu\text{s}$ as I desire for the photon generation protocol.

4.3.2 Qubit dephasing

I can measure the characteristic time T_2 for the phase ϕ of a coherent superposition $|g\rangle + e^{i\phi}|e\rangle$ to drift or dephase by implementing a four-step Ramsey spectroscopy protocol. When the dephase time T_2 is measured this way it is denoted as the T_2^* time. In this protocol, I prepare the $|g\rangle + e^{i\phi}|e\rangle$ state and observe the stability of its phase ϕ . In the first step of the protocol, a $\pi/2$ qubit pulse rotates the $|g\rangle$ state to the $\Psi(0) = |g\rangle + e^{i\phi_0}|e\rangle$ state, where the phase ϕ_0 is set by the $\pi/2$ pulse. In the second step, I wait some amount of time t_w during which the phase may undergo some random walk or dephase. The last two steps amount to measuring the overlap between this state at $t = t_w$ and the state at $t = 0$, or measuring $|\langle\Psi(0)|\Psi(t_w)\rangle|$. The third step rotates $\Psi(0)$ to the $|e\rangle$ state by applying a second $\pi/2$ pulse with the same phase as the first. Lastly, a readout is performed on the qubit state [68, 62].

When there is no dephasing during the wait time, the two $\pi/2$ pulses have the effect of a single π pulse. In this case, I expect the qubit to be in the $|e\rangle$ state. In the other extreme the qubit completely dephases. In this case, the second $\pi/2$ pulse is just as likely to rotate the qubit to the $|e\rangle$ state as the $|g\rangle$ state. I expect the excited state probability to be $P_e = 50\%$. Thus, as I increase waiting time, I expect P_e to decrease from 100% to 50% as the qubit dephases. Or written explicitly, $P_e = P_0 + P_1 e^{-t_w/T_2^*}$ with constants $P_0 = P_1 = 0.5$ for the ideal case.

Now, I consider an off resonant drive. When there is no qubit dephasing during the wait step, the phase of the drive rotates relative to the phase of the qubit at a frequency set by the difference between the drive frequency and qubit Δ_{t_2} . In this generalized T_2^* sequence, the rotating

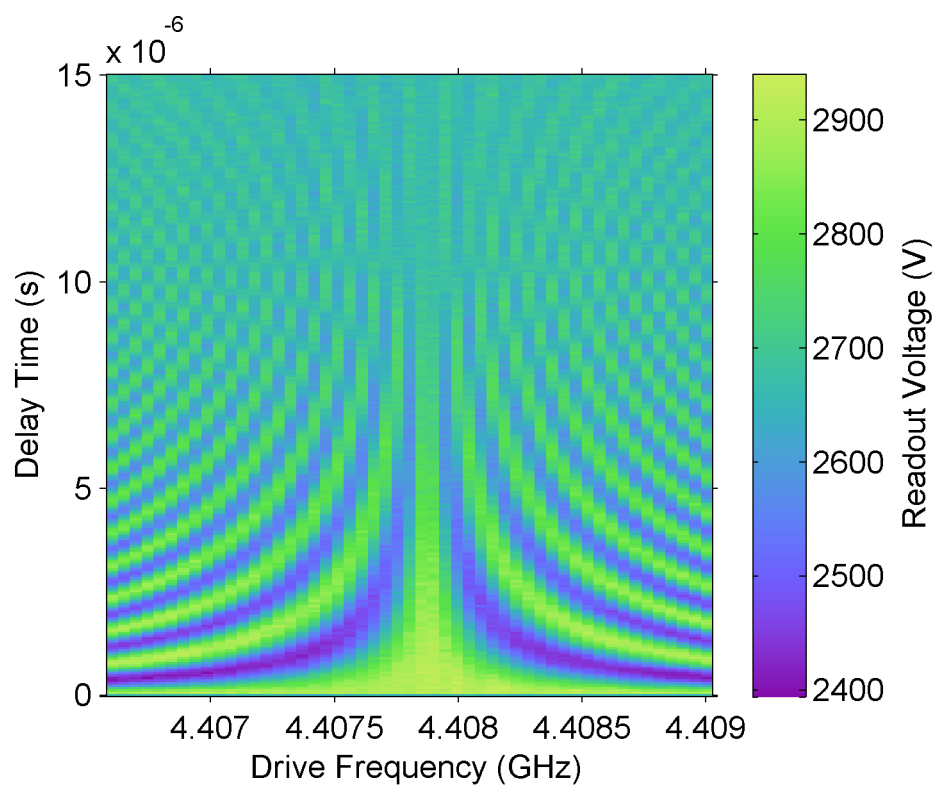


Figure 4.10: Ramsey measurement of the qubit dephasing as I adjust the pulse frequency. As the qubit dephases at large time, the excited state probability saturates and the contrast in the fringes is lost.

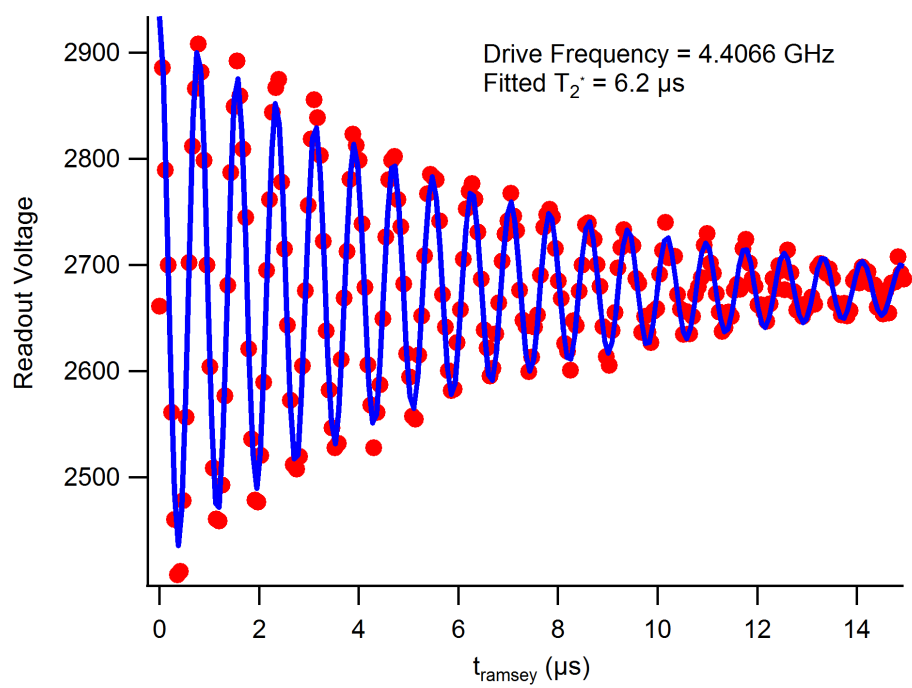


Figure 4.11: Ramsey measurement of the qubit dephasing with the drive detuned 1 MHz. As the qubit dephases the coherent oscillations washout.

phase causes P_e to oscillate at that difference frequency. As a result, I expect the excited state probability to both be decaying and oscillating. Written explicitly, the excited state probability is

$$P_e(t_w) = P_0 + \cos(\Delta_{t_2} t_w) P_1 e^{-t_w/T_2^*}, \quad (4.7)$$

where the constant P_0 is the steady state excited state probability and $P_0 + P_1$ is the initial excited state probability. For the ideal case, the constant $P_0 = P_1 = 0.5$.

I implement this T_2^* measurement by adjusting the wait time t_w and the $\pi/2$ pulse's frequency (and therefore Δ_{t_2}) in order to measure the qubit dephasing time T_2^* (Fig. 4.10). Most of my Ramsey measurement are conducted at only a few values of Δ_{t_2} . To demonstration the Ramsey fringes, the measurement shown in Fig. 4.10 is conducted at 51 values of Δ_{t_2} . However, this particular measurement was performed before implementing the high contrast single shot readout. Here, I do not threshold the single shot measurement voltages to assign the each instance in either the ground or excited state. Instead, I average the raw single shot measurements to plot the average voltage at each t_w and frequency. I fit a subset of data with $\Delta_{t_2} = 1$ MHz to Eq. 4.7 where constants P_0 and P_1 take on values of voltages (Fig. 4.11). I extract the dephasing time $T_2^* = 6.2 \mu\text{s}$. Thus, $T_2 \gg 0.15 \mu\text{s}$. Therefore, the qubit is coherent enough for the photon generation protocol.

Chapter 5

Photon generation and detection

I now reach the heart of the experiment. In this Chapter, I discuss single photon generation and detection using a superconducting transmon qubit coupled to a cavity. I use the blue sideband transition of the qubit cavity system to create photons. To analyze the photons, I operate the JPA in heterodyne (two quadrature) and homodyne (single quadrature) modes. For both detection methods, I quantify the single photon generation and detection by performing state tomography, which estimates the density matrix ρ .

To initially verify photon generation, I implement a measurement apparatus designed to protect and isolate the qubit-cavity system from the amplifiers at the cost of measurement efficiency. In these measurement, I see several signatures of photon generation and perform tomography on the propagating photon state using heterodyne detection. Limited by both detection inefficiency and generation fidelity, I infer a mixed state that corresponds to a single photon 12% of the time ($\rho_{11} = 0.12$) of the propagating mode, correcting for heterodyne detection's 1/2 quanta of added noise.

Working to optimize photon detection, I implement a homodyne detection scheme that minimizes the loss between the photon source and the JPA. In this case, I reconstruct a mixed state that is a single photon 36% of the time ($\rho_{11} = 0.36$). In this scheme, I quantify a JPA's backaction on the qubit-cavity system. I independently estimate the density matrix of the propagating photon state and the efficiency of my amplifier chain. I find that my photon measurements agree with my expectations within uncertainty using state fidelity as a metric.

5.1 Photon generation

I generate single propagating photons by first generating them in the cavity, and then letting them decay into a strong coupling output mode. I create the photons in the cavity by performing a calibrated π pulse on the blue sideband transition of the qubit cavity system, which excites the qubit and creates a photon in the cavity (Fig. 5.1). Once the photon is created in the cavity, it is strongly coupled to an output mode and decays, creating a propagating photon. I start by investigating the blue sideband pulse because it is the key step in the generation protocol.

5.1.1 Blue sideband measurements

I use the dynamics of the qubit-cavity system to confirm that I am addressing the blue sideband transition. The simplest check I can perform is to look at the Rabi-like oscillation of the blue sideband transition. During a blue sideband drive, the system oscillates between the $|0, g\rangle$ and $|1, e\rangle$ state (Fig. 5.1). Consider the situation when photons decay much faster than the qubit. If the photon decays when the system is in the $|1, e\rangle$ state, then the system will be in the $|0, e\rangle$. Until the qubit decays, the system no longer oscillates because the system does not have a photon to lose when the qubit flips to the $|g\rangle$ state, and the qubit will be stuck in the $|e\rangle$ state.

In my system, cavity photons decay much faster than the qubit. Photons decay in $1/(2\pi \times 410 \text{ kHz}) = 0.39 \mu\text{s}$, whereas the qubit decays in $T_1 = 10.2 \mu\text{s}$ (Section 4.3). Under a continuous blue sideband drive, the qubit cavity system decays to the $|0, e\rangle$ at a rate set by the cavity decay rate $\kappa = 2\pi \times 410 \text{ kHz}$. At larger times, the qubit can decay causing the system to saturate into a mixed state with the qubit excited half of the time [23]. I measure the excited state probability as a function of blue sideband pulse length (Fig. 5.2). This measurement protocol is nearly identical to Rabi oscillation (Section 4.2.1), where I drive the blue sideband transition for a certain time then perform single shot readout. From fitting these results to an exponentially decaying sinusoid, the oscillations between ground and excited state decay to the excited state at rate $\kappa_{\text{BS}} = 2\pi \times (370 \pm 10) \text{ kHz}$. This behavior is consistent with creating decaying single photons. However, I would like a more

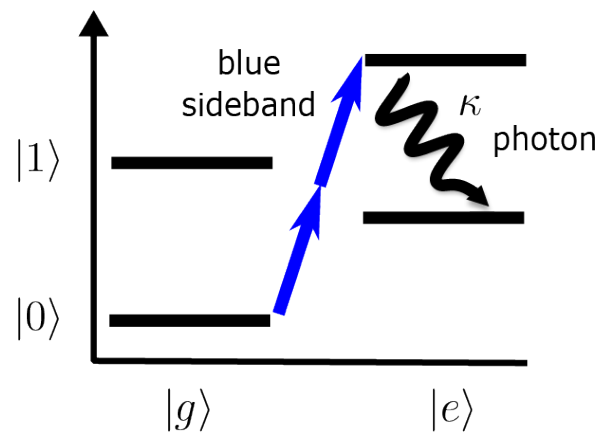


Figure 5.1: Energy level schematic for photon generation with the blue sideband.

rigorous confirmation that the blue sideband π -pulses are creating single photons.

5.1.2 Cavity photon detection with qubit

Now that I have seen indirect evidence that I am creating photons with the blue sideband drive, I use the system to directly detect cavity photons [69, 70]. Just like the dispersive Hamiltonian allows the cavity to be used for qubit readout, it also allows the qubit to be used to perform cavity photon number readout. I use the fact that the qubit frequency depends on the number of cavity photons to observe photons decaying out of the cavity following a blue sideband π -pulse. From the dispersive Hamiltonian (Eqn. 2.37), I can write the qubit frequency in terms of photon number

$$\omega'_q = \omega_q + 2\chi n. \quad (5.1)$$

as in Eqn. 2.39. Because the qubit frequency depends on photon number, I can calibrate π -pulses that are contingent on photon number. For example, a π -pulse whose frequency is $\omega_{q,1} = \omega_q + 2\chi$ is only a π -pulse when there is one photon in the cavity. To make qubit π -pulses contingent on cavity photon number, these pulses must be spectrally narrow compared with the qubit photon number splitting (2χ). A complete description of this approach can be found in Ref. [71].

To achieve photon number detection, I must do three things: first, I must know the qubit initial qubit state, then, I apply a photon number dependent π -pulse, lastly, I perform a single shot readout on the state of the qubit. If the qubit changed state, then a photon number corresponding to the qubit π -pulse is detected. For example, starting with the qubit in the $|e\rangle$ state, I apply a qubit π -pulse at the single photon qubit frequency ($\omega_q + 2\chi$). If I measure the qubit in the $|g\rangle$ state, then the π -pulse was successful and there was one photon in the cavity. Otherwise, if the qubit is measured in the $|e\rangle$ state, then the cavity does not have one photon.

To detect the decay of photons created by the blue sideband transition out of the cavity, I implement the following sequence. First, I apply a blue sideband π -pulse to create a photon in the cavity. Then, I wait for some delay time. Next, I apply a spectrally narrow qubit drive pulse at some frequency. If this pulse is at the correct frequency, then it will be a π -pulse contingent

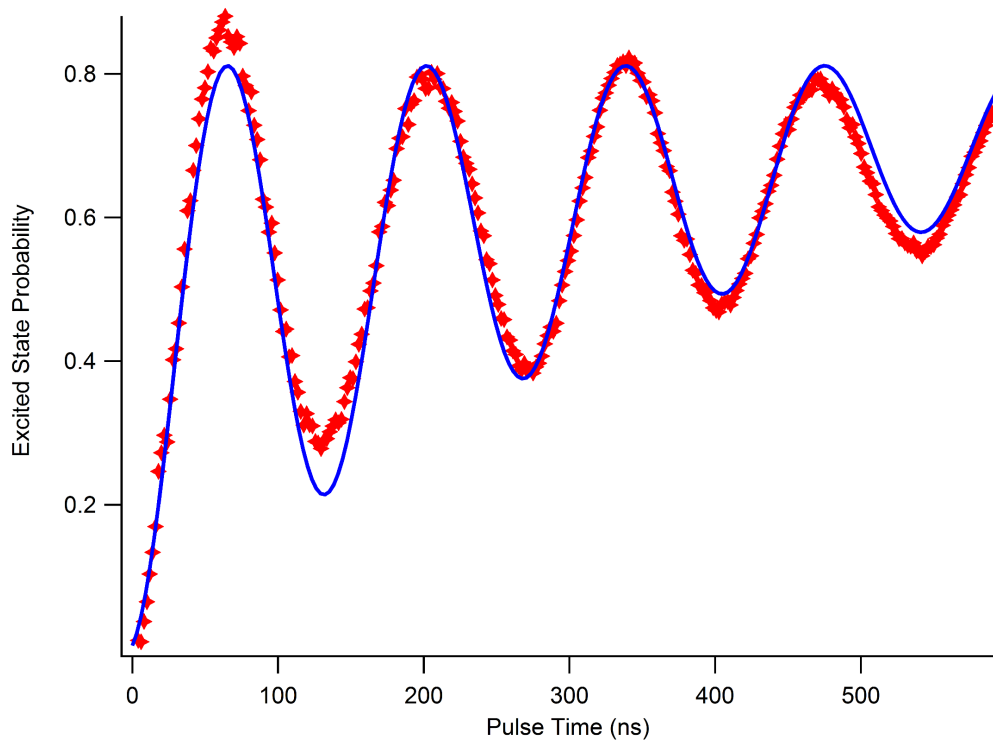


Figure 5.2: Excited state probability during a blue sideband drive (marks) fit to a offset exponentially decaying sinusoid (solid line). During a blue sideband drive, the qubit oscillates between the $|g\rangle$ and $|e\rangle$ state. As a photon decays from the cavity, the systems saturates to the $|e\rangle$ state.

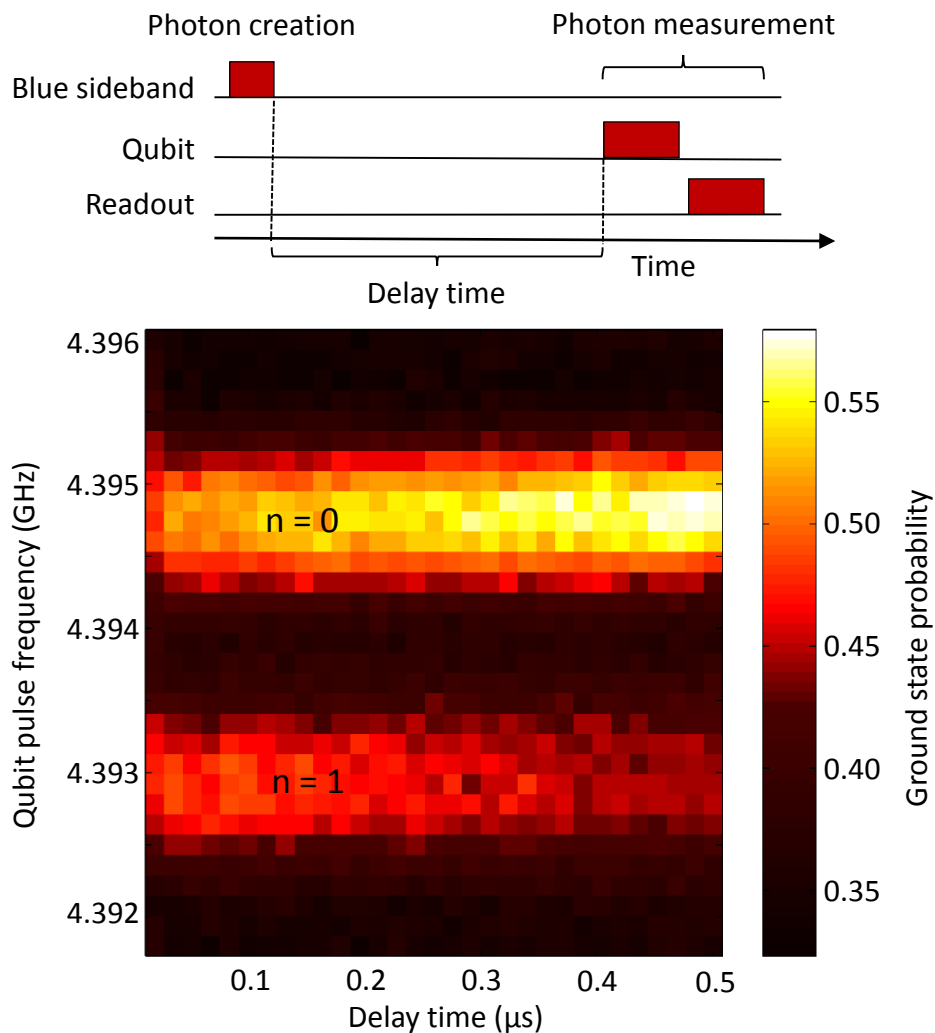


Figure 5.3: Detecting cavity photons created by a blue sideband π -pulse using photon number dependent qubit π -pulses. The $|g\rangle$ state probability is plotted following a second pulse (a qubit pulse) adjusting the qubit pulse's frequency and delay after the blue sideband pulse. When the pulse is at 4.3948 GHz or 4.3929 GHz, the pulse is π -pulse contingent on zero or one photon in the cavity, respectively. Because these pulses rotate the qubit to the $|g\rangle$, measuring the $|g\rangle$ state measures the respective photon number state (when the π -pulse is at 4.3948 GHz for $n = 0$ and 4.3929 GHz for $n = 1$). As the delay time increases the photon created by the blue sideband pulse decays to the $n = 0$ state.

on cavity photon number. Lastly, I perform a single shot readout on the qubit. I repeat this procedure roughly 10^3 times for each combination of delay time and drive frequency to build up statistics (Fig. 5.3). I adjust the drive frequency across the zero photon and single photon qubit frequency to detect the $|1\rangle$ state decay to the $|0\rangle$ state. I measure over a range of delay times to observe the photon decay out of the cavity. At drive frequencies 4.3948 GHz and 4.3929 GHz, I can resolve the $|0\rangle$ and $|1\rangle$ π -pulses, respectively. With increased delay time, the single cavity photon probability decreases and the probability of there being zero photon increases. From this measurement, I directly observe that the blue sideband π -pulse creates a photon in the cavity, and I see these photons decay.

5.2 Heterodyne detection

To detect the propagating photon, I connect the strongly coupled output to the JPA. The JPA is operated as a two quadrature, or heterodyne, detector by centering the JPA's gain $\Delta = -2\pi \times 1$ MHz detuned from the photon's frequency. The photon's frequency is set by the cavity's frequency when the qubit is in the excited state ($\omega_c + \chi$). The center of the JPA's gain is set by the frequency of the strong pump tone. As a result of operating the JPA as heterodyne detector the strong pump tone is 1 MHz detuned from the cavity's resonance. Because the cavity has a linewidth of $\kappa = 2\pi \times 410$ kHz, the the pump is filtered by the cavity.

This measurement strategy minimizes undesirable interaction between the qubit-cavity system and the JPA, but at the cost of reduced measurement efficiency. As a result, the JPA operates with modest measurement efficiency. In between the cavity and the JPA, there are reactive and attenuation lower pass filters designed to suppress photons whose frequency are above the cavity's resonance leaking into the cavity. Additionally, there are 3 non-reciprocal elements called circulators or isolators, which prevents the JPA's output from leaking back into the cavity. Because of all these elements, there is 4.6 dB of loss between the cavity and the JPA as measured at room temperature. As a result, a photon should be absorbed in transit approximately 65% of the time. In other words, the loss in between the cavity and JPA limits the measurement efficacy to roughly

$\eta_m \leq 0.35$. Additionally, intrinsic measurement inefficiency and cavity loss further reduces η_m .

5.2.1 Two quadrature filter and photon variance

As a photon decays out of the cavity, the JPA's measurement yields a time trace $V_m(t)$. As discussed in Section 2.3.1, a quadrature in a frame rotating at ω_{JPA} (the center of the JPA's band) is amplified and demodulated to yield the time trace $V_m(t)$. If the input signal were at ω_{JPA} , then $V_m(t)$ would contain a sequence of single quadrature measurements of the signal. In my case, the signal is at $\omega_{JPA} + \Delta$. The quadratures in the frame of the signal oscillate at a rate Δ with respect to the quadrature that the JPA measures. Consequently, an input $V_{in} = V_0 \sin((\omega_{JPA} + \Delta)t)$ going into the JPA becomes a measured time trace $V_m(t) = GV_0 \sin(\Delta t + \phi_0)$, where G is the heterodyne gain at $\omega_{JPA} + \Delta$, and ϕ_0 is a static phase shift in amplification and demodulation process.

In the photon measurements, this time trace $V_m(t)$ must be processed to achieve the two-quadrature measurement. I extract the values of X_1 and X_2 using two orthogonal filter function oscillating at Δ . For measurements of a steady oscillating field using the JPA as a heterodyne detector, the choice of the two filter functions is straightforward. Consider that signal V_{in} . Its output $V_m(t)$ oscillates at Δ . For this case, I can construct the two quadrature filters $f_{x1} = N_1 \cos(\Delta t)$ and $f_{x2} = N_2 \sin(\Delta t)$ corresponding to the X_1 and X_2 quadratures, respectively. The normalization constants N_i are set so that filter function is normalized over the measurement time interval from t_0 to t_1 . Or,

$$\int_{t_0}^{t_1} f_i^2(t) dt = 1. \quad (5.2)$$

Just like the corresponding quadratures, for long measurement intervals the two filter function are orthogonal, or

$$\int_0^\infty f_1(t) f_2(t) dt = 0. \quad (5.3)$$

As long as the measurement interval is long compared to the period of oscillations, then the finite measurements are approximately orthogonal. Using these filter functions, the values of the

measured quadratures then become

$$X_i = \int_{t_0}^{t_1} f_i(t) V_m(t) dt. \quad (5.4)$$

Capturing the pulsed photon signal with a heterodyne measurement adds additional requirements. In addition to having two orthogonal filter function with a phase $\pi/2$ radians apart, the filter function must match the temporal envelope of the photon decaying from the cavity. Specifically, for a pulse which has some temporal power profile $\mathcal{P}(t)$, I want $f_1^2(t) + f_2^2(t) = \mathcal{P}(t)$ for efficient measurement. The temporal profiles is similar the output mode A_{out} defined in Eqns. 2.6 and 2.7 with one major exception. It is distorted by the JPA's finite bandwidth.

Shown in Fig. 5.4, are the two quadrature filters matching the X_1 and X_2 quadratures that I use in my heterodyne measurements. Taken together, these two filter functions match the power profile of a state leaking out of the cavity and measured by the JPA. [For comparison to the measured temporal profile of the power leaking out of the cavity due to photon creation, see Fig. 5.11(c).] The two filter functions are formed by starting with two decaying sinusoids $f_1'(t) = e^{-\kappa/2t} \cos(\Delta t + \phi)$ and $f_2'(t) = e^{-\kappa/2t} \sin(\Delta t + \phi)$ for $t \geq 0$, both similar to A_{out} (Eqn. 2.6) oscillating at Δ . The decay κ is set to the cavity's decay rate and the detuning $\Delta = -1$ MHz. The phase ϕ sets the phase of the quadrature filters. To account for the bandwidth of the JPA, the two sinusoids are low pass filtered with the cutoff frequency set by the JPA bandwidth (1 MHz for the filter functions shown). A low pass filter h is used rather than a bandpass because the signal is demodulated at ω_{JPA} . The results are the filter functions shown in Fig. 5.4 and listed below:

$$f_1(t) = h(\omega_{\text{LPF}}, t) * \Theta(t) e^{-\kappa t} \cos(\Delta t + \phi) \quad (5.5)$$

$$f_2(t) = h(\omega_{\text{LPF}}, t) * \Theta(t) e^{-\kappa t} \sin(\Delta t + \phi). \quad (5.6)$$

Here, $\Theta(t)$ is the Heaviside step function and $h(\omega_{\text{LPF}}, t)$ is a low pass filter's impulse response with cutoff frequency equal to half the bandwidth of the JPA $\omega_{\text{LPF}} = 2\pi \times 0.5$ MHz. The symbol $(*)$ denotes convolution.

Well defined quadrature filter functions should be orthogonal over their range as defined in Eqn. 5.3. A sine and a cosine functions are approximately orthogonal over a span of many

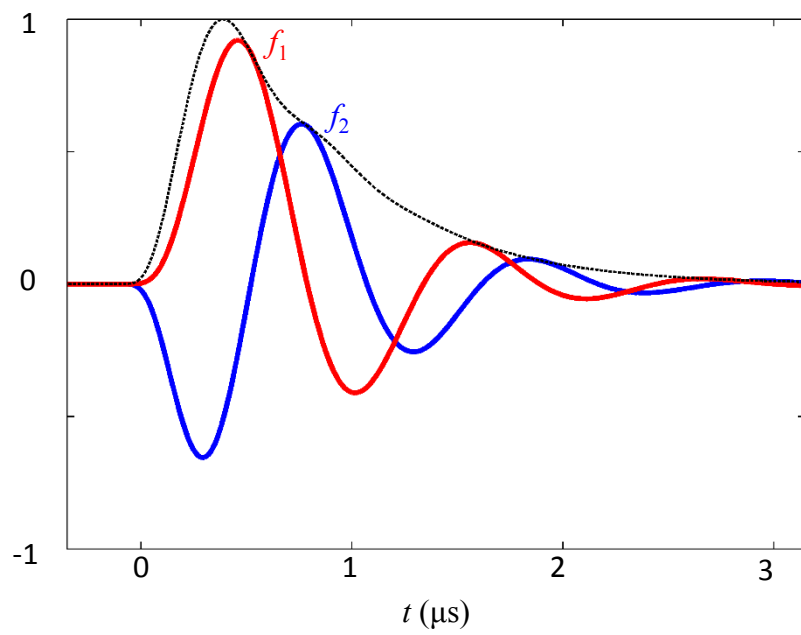


Figure 5.4: The two heterodyne filter functions $f_1(t)$ (red) and $f_2(t)$ (blue) along with their temporal profile $\sqrt{f_1^2(t) + f_2^2(t)}$ (black dotted line)

oscillations (without being constrained to an integer number of periods). Unfortunately for filter functions listed in Eqn. 5.5 and 5.6 and shown in Fig. 5.4, there are only few oscillations before the filter decays. Viewed in the frequency domain, this occurs because, the detuning $|\Delta|$ is not much larger than the cavity decay rate κ . As a consequence the two functions are not orthogonal for an arbitrary phase ϕ . Fortunately, there is a particular phase ϕ which makes an orthogonal pair of filter functions. Because the convolutions in the filter function are performed numerically, I numerically solve for the orthogonal ϕ . I use this orthogonal pair of filter functions $f_1(t)$ and $f_2(t)$ (Fig. 5.4) for my heterodyne photon detection with the JPA.

For well behaved arbitrary two-quadrature filter functions, $|\Delta| \gg \kappa$. Because $|\Delta|$ is limited by the JPA bandwidth BW_{JPA} to be amplified, I can cast this condition in terms of the JPA Bandwidth as:

$$BW_{\text{JPA}} \geq \Delta \gg \kappa \quad (5.7)$$

for well behaved arbitrary two-quadrature filter functions. In part because Eqn. 5.7 is not true for my heterodyne measurements, I optimized the photon generation and when performing the homodyne measurement in the next section (Section 5.3). However, I continue with heterodyne measurements to demonstrate the direct detection of the single photons, before moving on to homodyne detection and characterizing the entire experiment.

5.2.2 Comparison to qubit state

I use the JPA backed heterodyne measurements with temporal filters to directly observe photon power exiting the cavity as a result of the blue sideband pulse. As I saw in Section 2.1.3, creating the single photon state does not shift the average quadrature measurement, but does triple the noise power, or quadrature variance. Therefore, I expect to see the photon signal in $\text{var}(X_i)$. Because driving the blue sideband transition causes oscillations between the $|0, g\rangle$ and the $|1, e\rangle$ states, I expect creating a photon and exciting the qubit to be correlated. Indeed, I demonstrate that there is an increase in quadrature variance correlated with excited state probability by observing Rabi-like oscillations in $\text{var}(X_i)$ and P_e in response to a blue sideband drive.

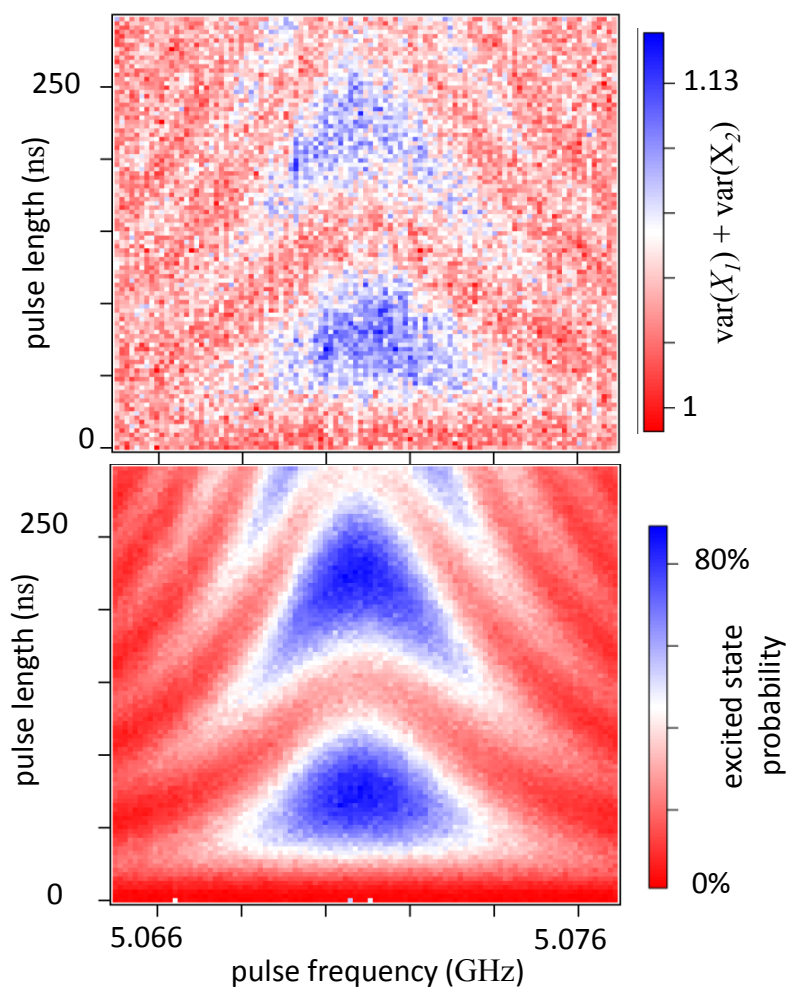


Figure 5.5: Measurement of $\text{var}(X_i)$ (above) and P_e (below) in response to a blue sideband pulse drive as the frequency and duration of the pulse is adjusted. I observe correlated, Rabi-like oscillations in $\text{var}(X_i)$ and P_e .

I implement a protocol similar to the one used to measure Rabi-like oscillation on to blue sideband. I modify this protocol by alternating between reading out the qubit and directly measuring photons exciting the cavity with the JPA (Fig. 5.5). In this measurement, I apply a fixed amplitude drive pulse for some duration, at some frequency. Then, I either perform a single shot readout on the state of the qubit, or I measure $V_m(t)$ with the JPA. From the quadrature measurements, I apply the quadrature filters (Fig. 5.4) to $V_m(t)$ in order to extract both quadrature values according to Eqn. 5.4. I repeat the protocol 30,720 times at each drive pulse frequency and length, computing the variance $\text{var}(X_1) + \text{var}(X_2)$. For the qubit measurements, I repeat the protocol 3840 times, calculating the probability of being in the excited state.

In both P_e and $\text{var}(X_1) + \text{var}(X_2)$, I see Rabi-like oscillations of the blue side band that are correlated. These measurement show I can generate and detect photons using the qubit-cavity system. The fact that the photon power oscillates correlated with P_e indicates that the measured increase in $\text{var}(X_1) + \text{var}(X_2)$ is due to single photons as the system oscillates between $|0, g\rangle$ and $|1, e\rangle$ state. That is, I directly measure single, propagating photons. Moreover, the measurements demonstrate I can simultaneously control the generation of single photons with the blue sideband while detecting the propagating mode with the JPA.

5.2.3 Density matrix reconstruction

The density matrix ρ is the most complete description of the state of a system, including both statistical and quantum uncertainty. It describes any statistical combinations of pure quantum states. To fully characterize my photon source, I want to determine the density matrix of the propagating state that the photon source creates. By analyzing the statistics of many two quadrature measurements of identically prepared photon states, I can infer the density matrix of the propagating photon state. Using this reconstructed density matrix, I can learn about the quality of my photon generation and detection.

I begin by repeatedly generating single photons. I implement a protocol where I apply a calibrated π -pulse on the blue sideband. Then, I perform a heterodyne measurement on the

state exiting the cavity with the JPA. I apply the two-quadrature filter functions (Fig. 5.4) to the measurements to get a pair of measured quadrature values (X_1, X_2) . I repeat this protocol 5,484,800 times to build up statistics on measured quadrature pairs. In Fig. 5.6, I plot the two quadrature histogram cast as a probability distribution. To act as a calibration or reference, I make two-quadrature measurements of the vacuum state. I repeat the two quadrature-heterodyne measurement 5,484,800 times without the blue sideband pulse. These non-pulsed measurements are also plotted as a histogram in Fig. 5.6. For comparison, the probability distribution for ideal measurement of a pure photon state is shown in Fig. 2.3.

As discussed in Section 2.3.4, the probability distribution of a two quadrature measurement of a state is that state's Q-function:

$$P(X_1, X_2) = Q(\alpha) = \frac{1}{\pi} \langle \alpha | \rho | \alpha \rangle. \quad (5.8)$$

Here, α is the complex coherent state amplitude ($\alpha = X_1 + iX_2$). The Q-function is a representation of the density matrix. By using Eqn. 5.8, I can use the measurements of vacuum to calibrate the x and y -axes in Fig. 5.6. With the calibrated axes, I can use Eqn. 5.8 to extract the density matrix elements for the measured photon state.

To facilitate these application of the Q-function, I can rewrite it terms of density matrix elements in a photon basis. Writing the coherent state in a photon basis $|\alpha\rangle = e^{-|\alpha|^2/2} \sum_n (\alpha^n / \sqrt{n!}) |n\rangle$, I substitute into Eqn. 5.8 getting

$$Q(\alpha) = \frac{1}{\pi} e^{-|\alpha|^2/2} \sum_{n,n'} \frac{\alpha^{*n}}{\sqrt{n!}} \langle n | \rho | n' \rangle e^{-|\alpha|^2/2} \frac{\alpha^{n'}}{\sqrt{n'!}}. \quad (5.9)$$

Writing the density matrix as a sum over density matrix elements in the photon basis $\rho = \sum_{ij} |i\rangle \rho_{ij} \langle j|$, I write the Q-function as a linear superposition of density matrix elements. The

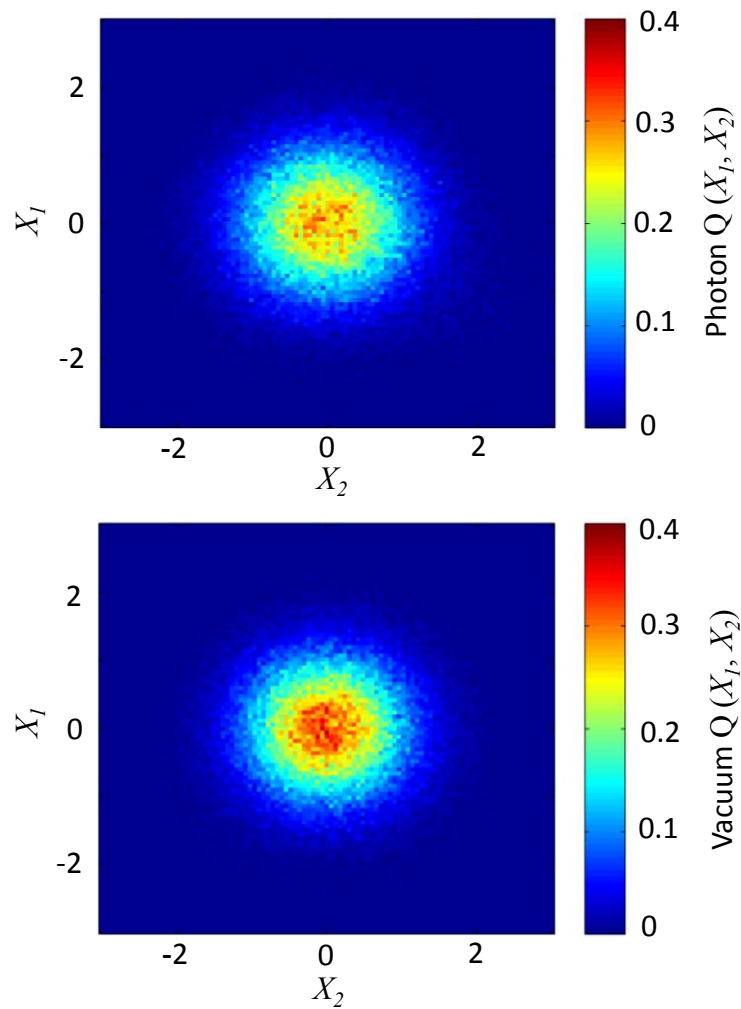


Figure 5.6: Histograms from two quadrature measurement of the photon state (top) and the vacuum state (bottom) plotted as the Q-function (probability density). The photon's distribution is slightly flattened and broadened compared to vacuum.

Q-function now becomes

$$P(X_1, X_2) = Q(\alpha) = \rho_{00} \frac{1}{\pi} e^{-|\alpha|^2} \quad (5.10)$$

$$+ \rho_{01} \frac{1}{\pi} e^{-|\alpha|^2} \alpha$$

$$+ \rho_{10} \frac{1}{\pi} e^{-|\alpha|^2} \alpha^*$$

$$+ \rho_{11} \frac{1}{\pi} e^{-|\alpha|^2} |\alpha|^2$$

$$+ \dots \quad (5.11)$$

This form of the Q-function shows that the Q-function is linear in density matrix elements ρ_{ij} . Moreover, it shows a clear mapping from density matrix elements to phase space (two-quadrature) probability density.

To calibrate the quadratures, I fit the vacuum probability distribution to the probability distribution of the vacuum state using the measurement chain's gain as the only free parameter. The vacuum state probability distribution is given by Eqn. 5.10 when $\rho_{00} = 1$ and all other elements equal zero. Specifically, the measured vacuum probability distribution is fit according to $Q_{00}(G\alpha)$ where G is gain and Q_{00} is the vacuum state probability distribution. Dividing the measured quadratures in both the vacuum and photon measurement by G calibrates the quadratures in units of quanta.

Once I have the photon probability distribution calibrated in units of quanta, I can fit the distribution to according to Eqn. 5.10 to extract the desired density matrix elements. The fitting is a linear fitting to the density matrix elements ρ_{ij} using a two photon basis (all combinations of $i = 0, 1, \text{ or } 2$ and $j = 0, 1 \text{ or } 2$). That is, I fit to both diagonal and off-diagonal elements. A two photon basis is deemed sufficient, because the two component ρ_{22} is negligible. I apply the constraint that the trace of the density matrix $\text{tr}(\rho) = 1$. A line cut through the center of the photon data and the fit are shown in Fig 5.7. The magnitude of the photon density matrix elements extracted from the fit are shown in Fig 5.8.

From measured density matrix (Fig 5.8), I can see that I have generated a state whose single photon element is $|\rho_{11}| = 0.12$. I generate and detect a mixed state which is 12% single photon

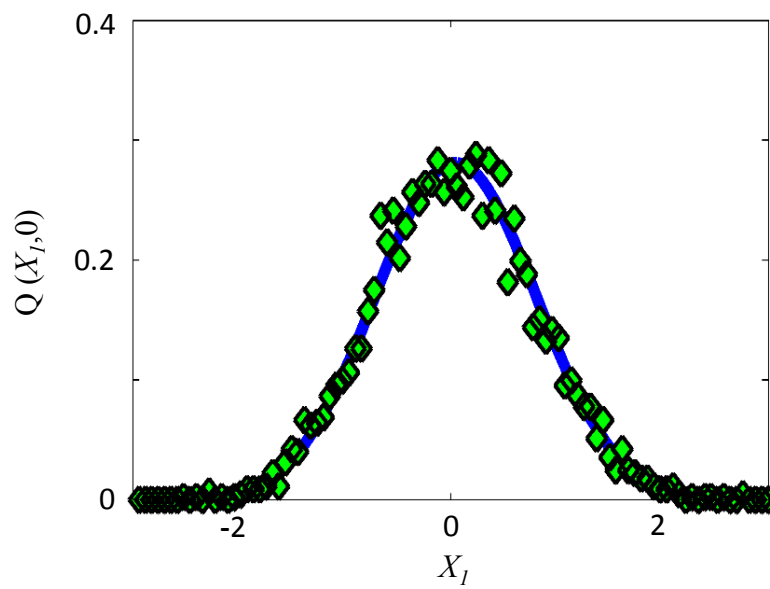


Figure 5.7: A line cut through the center of the measured single probability density (markers) with the best fit to density matrix elements (solid line).

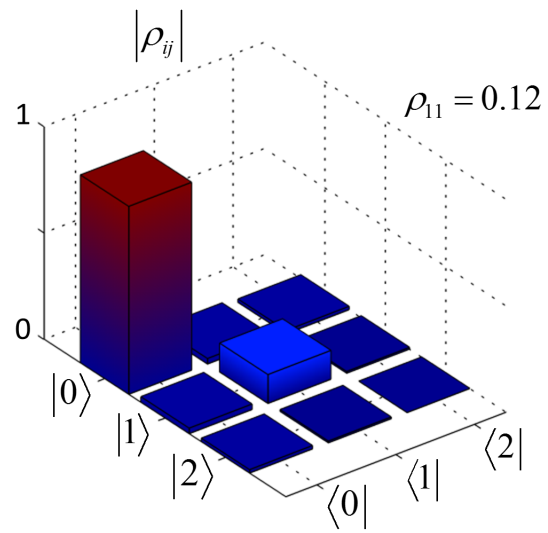


Figure 5.8: Reconstructed density matrix elements $|\rho_{ij}|$ of the measured photon state using heterodyne detection.

and remainder is vacuum. This density matrix is consistent with ideal photon generation ($\rho_{11} = 1$) that is measured with 12% efficiency (Section 2.3.5). This efficiency is relative to ideal heterodyne detection. In other words, it does not include the added vacuum noise all heterodyne detectors must add. In reality, I likely generated a propagating mixed state $\rho = (1-p)|0\rangle\langle 0| + p|1\rangle\langle 1|$ whose single photon component is some p . This mixed state is measured with some efficiency η_m (relative to ideal two quadrature detection) such that the product $p\eta_m = 0.12$.

This density matrix confirms that I have successfully generated single photons with the blue sideband of a qubit-cavity system and detected these photons with the JPA. I have measured a modest signal photon component $\rho_{11} = 0.12$. As a consequence, I want to optimize my generation and detection when I move on to homodyne detection.

5.3 Optimized photon generation and homodyne detection

I optimize my detection and operate the JPA in a homodyne detection scheme for two main reasons. One, homodyne detection adds less noise than heterodyne. Two, using one filter function in homodyne detection side steps questions of making arbitrary two-quadrature filter function present in my heterodyne detection. Similar to my heterodyne measurements, I reconstruct the density matrix ρ_m of the state I detect to characterize the photon source and detection. In addition, I independently characterize the system, compare my measurements to my expectation, and find agreement within uncertainty.

I make several changes to optimize the generation and detection. To allow for an independent characterization of the measurement efficiency, a switch can connect the amplifier chain to a thermal noise source (Fig. 5.9). I cable the experiment to minimize the loss between cavity and JPA. I move the filters, remove one circulator, and minimize microwave cable length and number of connectors to reduce the loss between the cavity and JPA to 1.6 dB as measured at room temperature. (See Appendix A for a detailed description of the photon generation and detection apparatus.) However, removing the circulator makes the qubit-cavity system less isolated from the JPA, and therefore more susceptible to amplifier backaction. Additionally, I optimize the quadrature filter function

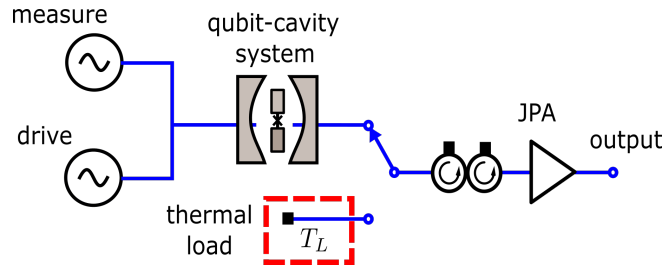


Figure 5.9: Simplified schematic for photon generation. The drive and measurement microwave generators couple to the input of the qubit cavity system where the measurement tone excites the cavity in order to infer the qubit state, and the drive tone manipulates the state of the qubit-cavity system. A switch can connect the amplifier chain to a thermal noise source allowing for an independent characterization of the measurement efficiency.

and operate the JPA as a homodyne detector. All of which should improve measurement efficiency. Lastly, I implement a more sophisticated generation protocol to improve the purity the propagating photon state.

5.3.1 Protocol

To implement efficient photon generation, I still adopt a protocol based on a blue sideband π -pulse, but with the addition of qubit measurements. The measurements allow me to select only the instances when a photon is created, thereby improving the fidelity of photon generation [72]. One measurement occurs before the blue sideband drive pulse and a second occurs after the photon has decayed [Fig. 5.11(a)]. I select on the initial measurement that project in the $|g\rangle$ state, to insure that the qubit starts in the $|g\rangle$ state as required for photon generation. This selection removes approximately 6% of the trials, which are primarily due to the steady-state excited state population of the qubit. Secondly, I select on instances when the second measurement projects the qubit into the $|e\rangle$ state. Combining both these selections ensures that the blue sideband π -pulse successfully flips the qubit from $|g\rangle$ to $|e\rangle$ and thereby creates a photon. Additionally, the second selection ensures that the photon decays at the excited state cavity frequency. The second selection removes approximately 26% of the instances, primarily due to the qubit decaying between the drive pulse and the selection. A smaller contribution is due to blue sideband pulse infidelity.

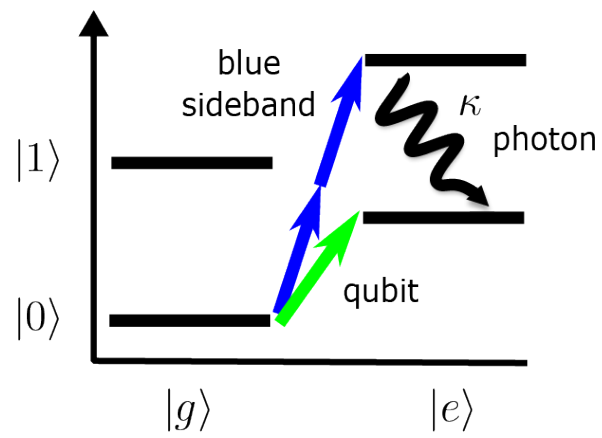


Figure 5.10: Energy level diagram for photon generation and calibration.

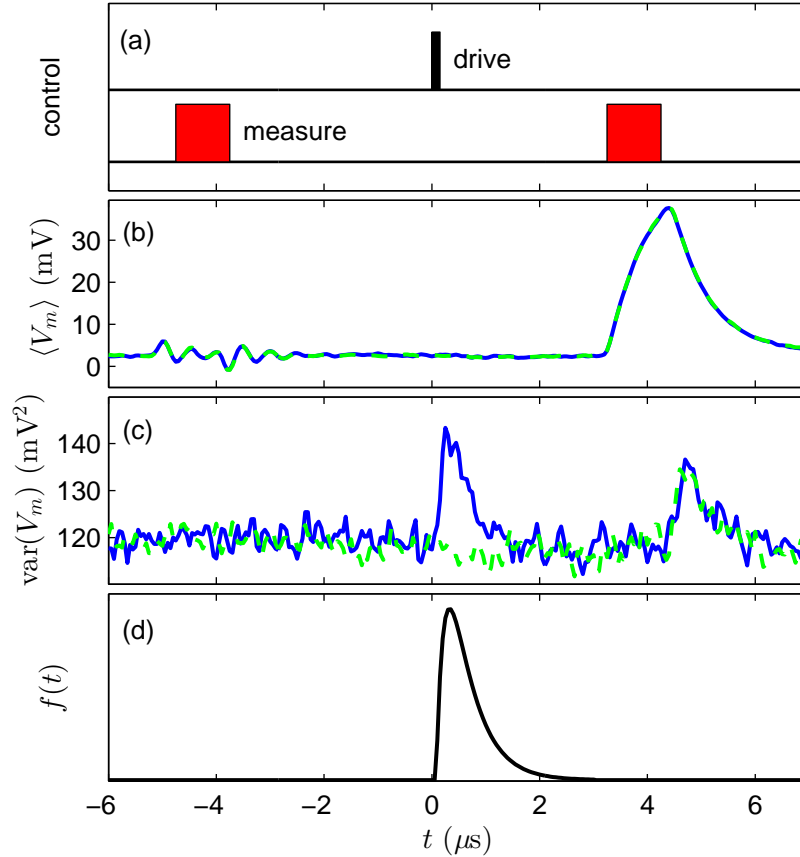


Figure 5.11: Timing diagram for the experiment. (a) A timing diagram for the photon creation and measurement sequence. The drive tone (black) either creates a photon or excites the qubit for the vacuum calibration. Qubit readout tones (red) are used before and after the drive. (b) The mean voltage $\langle V_m \rangle(t)$ measured from 7000 individual time traces with the drive at the blue sideband frequency (solid blue) or at the qubit's frequency (dashed green). (c) The variance of the individual measurements $\text{var}(V_m)(t)$ with the drive at the blue sideband frequency (solid blue) and at the qubit frequency (dashed green). In blue, the photon power can be seen following the blue sideband pulse at $t = 0 \mu\text{s}$. For the control in green, no such signal is seen. (d) The mode matching function $f(t)$ to extract the quadrature measurement of the propagating mode.

Because the qubit measurement must preserve the qubit in its ground state for photon creation, the measurement must be quantum non-demolition (QND). Furthermore, because qubit readout occurs both before and after photon detection is to take place, the qubit readout must be compatible with photon measurement. To satisfy these two requirements, I use a dispersive transmission readout with the JPA [31, 32, 63] (Section 4.1.1). I operate the JPA with its narrow-band gain centered on the qubit-excited cavity resonance frequency. This arrangement allows the JPA to be used both for qubit readout and photon homodyne measurement.

To provide an accurate calibration for the experiment, I modify the photon generation protocol the minimal amount that ensures no photons are generated. I replace the π -pulse on the blue sideband transition with a π -pulse on the qubit transition (Fig. 5.10 in green). This control sequence prepares the qubit cavity system in the $|e, 0\rangle$ state rather than the $|e, 1\rangle$ state; thus, the cavity does not emit a photon. All other aspects of the protocol, including the qubit state and the data processing procedure are common to both protocols.

5.3.2 Homodyne detection and tomography

To characterize the propagating state, I perform tomography on the output mode of the cavity to determine its density matrix ρ_m . In my tomography procedure, I measure a single quadrature of the cavity output field during the photon generation protocol. I can reconstruct the density matrix by repeating the generation and measurement protocol many times and at several different values of JPA carrier phase. Because I choose to create a single photon, which has a phase independent density matrix, I unlock the phase between the generation pulse and the JPA carrier thus sampling all phases uniformly. From a histogram made from many quadrature measurements I extract the diagonal elements of the density matrix written in the photon number basis. If there were any off-diagonal elements, these would vanish due to the phase averaging.

I operate the JPA as a homodyne detector with its gain centered on the frequency of the photon. Like the heterodyne detection, the output of the JPA is mixed down to yield a time trace $V_m(t)$. Because the JPA's gain is not detuned from the signal, then its measurement $V_m(t)$ contain

information about a single quadrature, where the phase of the quadrature is set by the JPA's pump. I form one measurement set by repeating the pulse sequence shown in Fig. 5.11(a) 7000 times (with the π -pulse applied to the blue sideband). The temporal envelope of the photon can be seen in the variance of the set $\text{var}(V_m)(t)$ at time $t = 0 \mu\text{s}$ [Fig. 5.11(c)]. As expected for a single photon, no feature is present in $\langle V_m \rangle(t)$ at $t = 0$.

5.3.2.1 Quadrature measurement

To complete the reconstruction, each $V_m(t)$ must be processed to yield a single quadrature value of the propagating mode. From this raw data, I make an estimate of one quadrature of the mode emitted by the cavity when the drive pulse is applied. I desire a mode matching function $f(t)$, that weights the time average of $V_m(t)$ to produce an optimum estimate of the quadrature value. For infinite measurement bandwidth, I expect the optimum $f(t)$ to be a decaying exponential pulse with decay constant $\kappa/2$ as defined for output mode A_{out} (Eqn. 2.7) [73] and a rise time equal to the duration of the drive pulse (150 ns). Due to the finite JPA bandwidth, I anticipate that $f(t)$ is found by convolving the infinite bandwidth optimum by the effective filter's impulse response $h(\omega_{\text{LPF}}, t)$ [74]. In practice, I write

$$f(t) = h(\omega_{\text{LPF}}, t) * \begin{cases} 0 & t < 0 \\ \cos(2\pi t/T_r) & 0 \leq t \leq T_r \\ e^{-(t-T_r)\kappa/2} & T_r < t \end{cases}$$

as a function of three parameters (rise time T_r , decay constant κ , and low pass filter cutoff $\omega_{\text{LPF}} = BW_{\text{JPA}}/2$) and adjust these to minimize the zero-photon contribution of the density matrix extracted from the data set. I perform this determination of $f(t)$ once, using photon creation and calibration data sets that are not used in subsequent analysis. As seen in Fig. 5.11(d), $f^2(t)$ looks like the photon creation variance [Fig. 5.11(c)], indicating that my optimization of $f(t)$ has produced a sensible result.

Extracting the quadrature value is complicated by the presence of a dc offset in the $V_m(t)$ which drifts during the acquisition of a full data set. To remove drifts in the dc offset from the

quadrature measurement, I perform a linear least-squares fit using a measurement of the background voltage in addition to the mode matching function. For each trace I assign an uncalibrated quadrature value V_q by minimizing

$$\mathcal{J} = \int \left[V_m(t) - (V_q f(t) + V_{dc} \tilde{b}(t)) \right]^2 dt \quad (5.12)$$

over V_q where V_{dc} is the dc voltage and $\tilde{b}(t)$ is the windowing function that defines when the dc offset is measured. The windowing function is a piecewise constant function that is nonzero during most of a $56 \mu\text{s}$ interval that includes the photon generation protocol. But during the qubit measurements, $\tilde{b}(t) = 0$. The result of the cost function minimization is an analytic expression for an individual quadrature measurement

$$V_q = \frac{\int V_m(t) f(t) dt}{\int \tilde{b}(t) f(t) dt} - V_{dc}. \quad (5.13)$$

This expression is applied to each $V_m(t)$ resulting in a set of uncalibrated quadrature measurements of the propagating mode.

A histogram of this set of measurements is shown as the narrow blue bars in Fig. 5.12. I generate a calibration data set following the same procedure as was used to generate the measurement set, but using the control protocol (π -pulse on the qubit transition). Indeed, when no photon is created, no extra variance is visible in $\text{var}(V_m)(t)$ at $t = 0$ [Fig. 5.11(c)]. Reducing each trace to quadrature values, I find the histogram shown in Fig. 5.12.

To calibrate the quadrature values, I fit the histograms of the calibration data sets to Gaussian distributions using the gain of the full measurement apparatus as the only fit parameter. But due to the fact that a small fraction of the JPA output is injected back into the cavity through the finite isolation of the circulators (determined in Section 5.3.2.2), I do not assume that the cavity is in its vacuum state. Rather, I expect to prepare the cavity in a mixed, squeezed state with $\bar{n} \ll 1$. Although the large isolation of the circulators ensures that the cavity's squeezed quadrature has almost exactly vacuum variance, the amplified quadrature can have variance measurably larger than vacuum, particularly at larger values of JPA gain. Because there is a fixed, but unknown

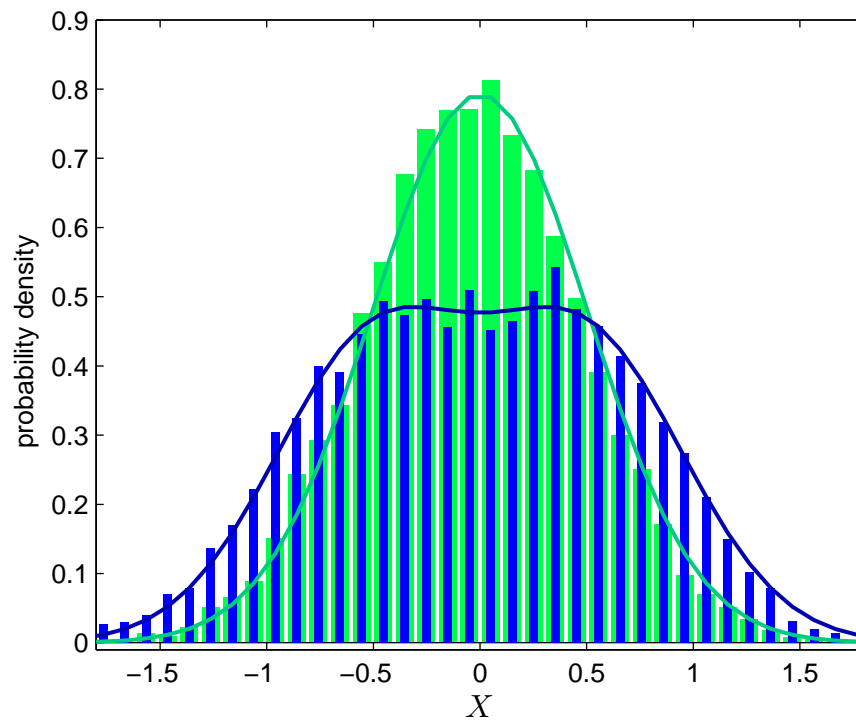


Figure 5.12: Histogram of a quadrature measurement set of single photons (narrow blue bars) and the no-photon control (wide green bars) with the JPA gain at 29 dB. The histograms are plotted as a probability density (bars) and are fit by the expected distribution for a diagonal density matrix with a 3 photon Fock basis (solid lines).

phase relationship between the quadrature I measure and the squeezed quadrature of the cavity, I calibrate assuming I measure the squeezed quadrature and assuming I measure the amplified quadrature. I use these two cases to bound the systematic uncertainty in the calibration of the vacuum variance, where I use the convention that one quadrature of a vacuum state has variance $\text{var}(X) = 1/4$.

5.3.2.2 JPA backaction

To quantify the cavity photon variance due to JPA backaction, I study the qubit dephasing [75]. As seen in the dispersive Hamiltonian for the qubit cavity system in Eqn. 2.39, the frequency of the qubit depends on the number of photons in the cavity. Therefore, a varying number of cavity photons ($\text{var}(n) > 0$) dephases the qubit. Because the qubit resonance frequency is far-detuned from the cavity, I treat the squeezed cavity field as dephasing the qubit with a thermal distribution. From Ref. [76], in the strong dispersive regime the dephasing rate when there are N photons in the cavity is

$$\Gamma_N = \kappa [(\bar{n} + 1)N + \bar{n}(N + 1)], \quad (5.14)$$

where κ is the coupling rate to a thermal bath with average number of cavity photons \bar{n} . Summing over a thermal distribution of N defined by \bar{n} (Eqn. 2.23), I calculate a photon dephasing rate

$$\Gamma = \Gamma_0 + \kappa[2\bar{n} + 2\bar{n}^2 + O(\bar{n}^4)] \quad (5.15)$$

in terms the intrinsic dephasing rate Γ_0 , \bar{n} and κ . Note that the additional dephasing rate is indeed proportional to the photon variance $\Gamma - \Gamma_0 = 2\kappa \times \text{var}(n)$ in this case (Eqn. 2.25). Measurements of the qubit dephasing rate ($\Gamma = 1/T_2^*$) over the range of JPA gains are shown in Fig. 5.13(a).

For the resulting photon distribution in the cavity, I assume that \bar{n} follows a model characterized by a single isolation parameter L , which characterizes the fraction of JPA output misdirected into the cavity as

$$\bar{n} = (1/4)L(G_{\text{JPA}} - 1), \quad (5.16)$$

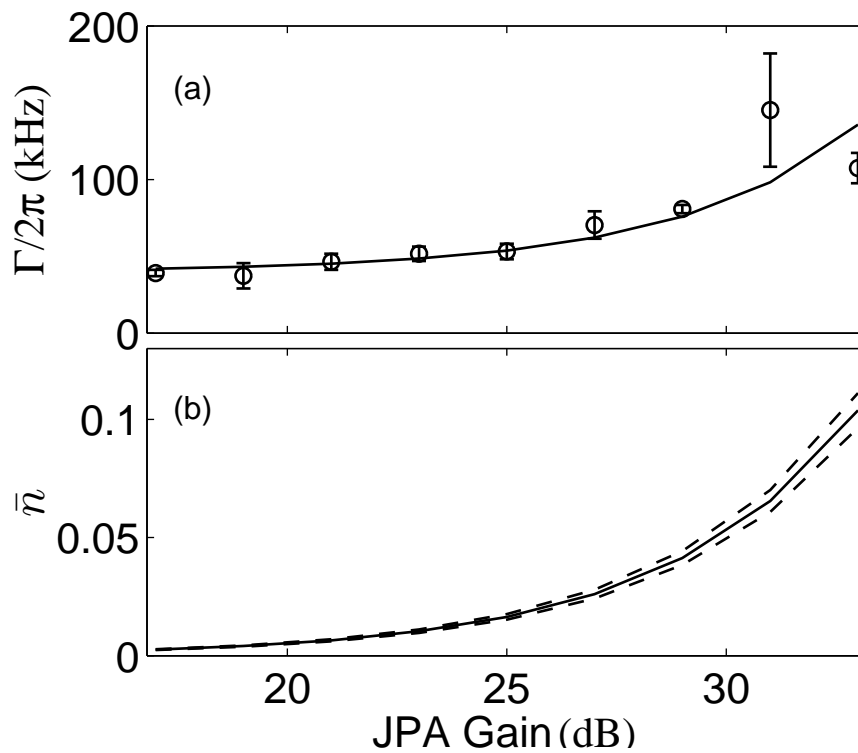


Figure 5.13: Quantifying backaction. (a) The qubit dephasing rate ($\Gamma = 1/T_2^*$) is shown (points) over a range of JPA gains along with a fit (line) to Eqn. 5.15 over the range of JPA gains (main text). (b) The solid line shows the best estimate of the average photon number in the cavity \bar{n} (uncertainty in dashed lines) due to the JPA at each gain used in the experiment.

where G_{JPA} is the JPA gain. I fit this model substituted into Eqn. 5.15 to measurements of Γ , extracting $L = (2.1 \pm 0.1) \times 10^{-4}$ (-37 dB) and $\Gamma_0/2\pi = 40 \pm 2$ kHz. The isolation is consistent with the specifications for the two commercial circulators between the cavity and the JPA (Fig. A.1). From this model, I find the average intercavity photon number due to JPA gain shown in Fig. 5.13(b) plotter over a range of JPA gains.

5.3.2.3 Reconstructing density matrix

Finally, I complete the tomography by fitting the histograms to probability distributions for diagonal elements of the density matrix in a 3 photon basis yielding one measurement of the density matrix. A 3 photon basis is sufficient because the three photon component ρ_{33} is indistinguishable from 0. Because I am restricting myself to a density matrix where the only the nonzero elements are diagonal elements ρ_{ii} , I can treat this state as a probabilistic combination of pure photon states. As a results, I can write the quadrature probability distribution as a linear combination of the probability distribution of pure photon states

$$P_{\rho_{ii}}(X) = \rho_{00}P_0(X) + \rho_{11}P_1(X) + \rho_{22}P_2(X) + \rho_{33}P_3(X). \quad (5.17)$$

I can compute the probability distribution of the pure photon states $P_n(X)$ either from the Wigner function (Sections 2.3.2 and 2.3.3), or from the wave functions of the Fock states

$$P_n(X) = \Psi_n^*(X)\Psi_n(X). \quad (5.18)$$

Written explicitly, I get

$$P_0(X) = \sqrt{\frac{2}{\pi}}e^{-2X^2} \quad (5.19)$$

$$P_1(X) = 4\sqrt{\frac{2}{\pi}}e^{-2X^2}X^2 \quad (5.20)$$

$$P_2(X) = \frac{1}{2}\sqrt{\frac{2}{\pi}}e^{-2X^2}(16X^4 - 8X^2 + 1) \quad (5.21)$$

$$P_3(X) = \frac{2}{3}\sqrt{\frac{2}{\pi}}e^{-2X^2}(16X^6 - 24X^4 + 9X^2). \quad (5.22)$$

Thus, I fit the probability distributions from each data set to Eqn. 5.17 to extract the diagonal density matrix elements.

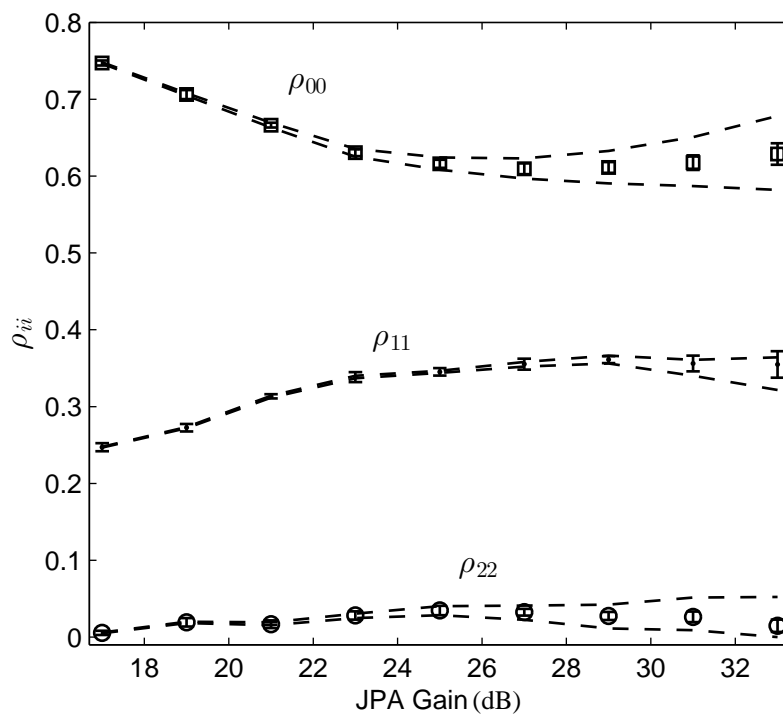


Figure 5.14: Diagonal density matrix elements determined from fitting the quadrature histogram over a range of JPA gains from 17 dB to 33 dB. The error bars are determined from the standard deviation of the mean using 8 sets of the quadrature measurements at each gain; (only 4 sets are used at 17 and 33 dB). The systemic uncertainties are indicated with dashed lines.

Each density matrix element is determined as the average value of multiple realizations of each measurement set. To optimize the photon measurement I find the density matrix elements over a range of JPA gains from 17 to 33 dB (Fig. 5.14). These density matrix elements are sensitive to all imperfection in the photon generation and detection. For ideal generation and detection, the ρ_{11} component would be 1 and all others 0. Instead, the single photon component has a peak value of $\rho_{11} = 0.361$ with ± 0.005 statistical and ± 0.005 systematic uncertainties at a JPA gain of 29 dB. However, at this gain there is a two photon component of $\rho_{22} = 0.027$ with ± 0.005 statistical and ± 0.015 systematic uncertainties. Considering the two photon generation relative to single photon generation, I have $2\rho_{22}/\rho_{11} \approx g_2(0) = 0.32 \pm 0.07$ with a 0.15 to 0.41 systematic uncertainty bound (Fig. 5.15). [For comparison, $g_2(0) = 1$ for any coherent state.] By decreasing the JPA gain to 17 dB, the two photon component becomes $\rho_{22} = 0.005 \pm 0.003$ with a single photon component dropping to $\rho_{11} = 0.247 \pm 0.004$, giving $g_2(0) = 0.15 \pm 0.08$. These results show that an increase in the JPA gain improves the measurement efficiency.

However, as I saw in Section 5.3.2.2, increasing the JPA gain also increases the measurement backaction. At my peak ρ_{11} (29 dB of JPA gain), there is an average photon $\bar{n} = 0.041 \pm 0.003$ in the cavity due to JPA backaction, likely accounting for most of the two photon component in the measured density matrix. The deleterious effects of this backaction can be seen in both the larger systematic uncertainty at larger JPA gain and the increased probability of creating two photons instead of just one.

5.3.3 Characterizing photon generation and efficient homodyne detection

To understand the limitations of single photon generation and detection, I characterize the experimental imperfections over a range of JPA gains. In particular, I characterize the internal loss of the cavity and measurement efficiency. This characterization gives a prediction for the state that I create and an expectation for how efficiently I can measure it. I compare my expectation with my measurements to validate my understanding of the photon generation process.

I make a prediction of the state I expect to measure if the photon generation protocol created

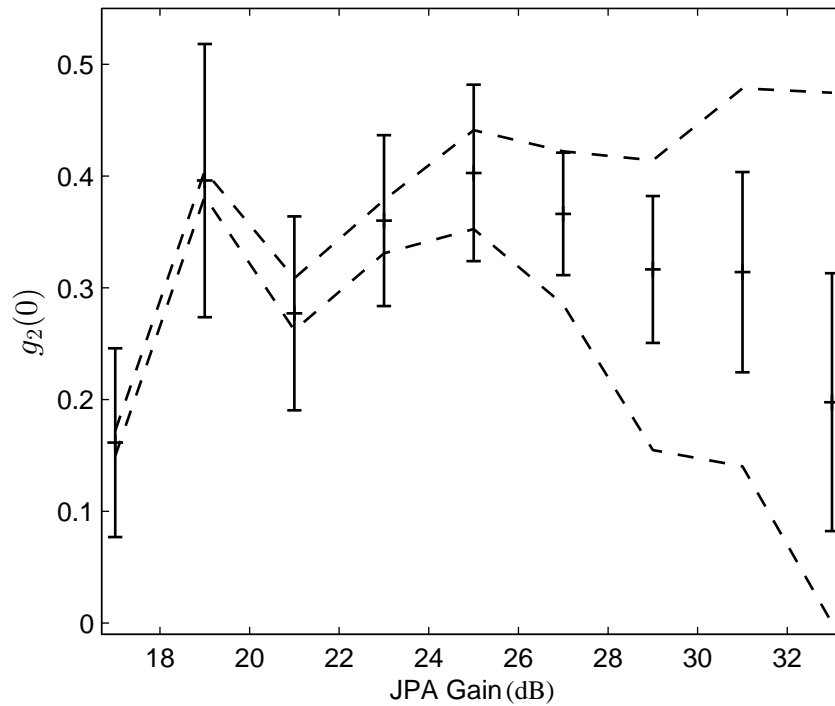


Figure 5.15: The values of $g_2(0)$ computed from the density matrix elements. Both the single standard deviation statistic uncertainty (error bars) and the systematic error bounds (dashed lines) are calculated from the uncertainties in density matrix elements. The values of $g_2(0)$ represent likelihood of detecting two photons compared to one. For a pure photon state $g_2(0) = 0$ and for a coherent $g_2(0) = 1$.

a pure single photon state in the cavity. First, I form an expression for the density matrix of the output mode ρ_{out} by accounting for the coupling of the cavity field to unmeasured ports. Due to the relative coupling rates, a cavity photon has a $\kappa_{\text{out}}/\kappa$ probability of decaying to the output port, where the coupling rate to the output port is $\kappa_{\text{out}}/2\pi = 300$ kHz and the total decay rate is $\kappa/2\pi = 410$ kHz. I would therefore expect to generate a propagating state ρ_{out} characterized by

$$\rho_{\text{out}} = \frac{\kappa - \kappa_{\text{out}}}{\kappa} |0\rangle\langle 0| + \frac{\kappa_{\text{out}}}{\kappa} |1\rangle\langle 1| \quad (5.23)$$

from Section 2.3.5 with the ratio $\kappa_{\text{out}}/\kappa$ cast as η .

5.3.3.1 Independent measurement characterization

Next, I form an expectation for how well I can measure ρ_{out} by independently characterizing the measurement inefficiency. In order to independently determine the measurement efficiency, I inject states of known variance into the measurement chain. As I adjust the input variance into the measurement chain, I determine the additional variance N_{add} introduced by the measurement. The source of known variance is a 50 Ω resistor on a variable temperature stage connected by a switch to the JPA input (Fig. A.1). I perform the determination of N_{add} at three different JPA gains— 20, 25, and 30 dB (Fig. 5.16). The data are plotted as output-noise power-spectral-density S_{out} against input power spectral density S_{in} (set by Eqns. 2.24 and 2.27). I extract N_{add} by fitting data in Fig. 5.16 to

$$S_{\text{out}} = G(S_{\text{in}} + N_{\text{add}}), \quad (5.24)$$

where G is the gain of the measurement chain [26]. These fits yield three values of N_{add} plotted as measurement efficiency

$$\eta_m = (2N_{\text{add}} + 1)^{-1} \quad (5.25)$$

[77] in Fig. 5.17 (circles).

To find N_{add} at other values of the JPA gain, I use a model that decomposes N_{add} into contributions from the JPA itself N_{JPA} and from the remaining measurement N_{HEMT} . Adopting this added noise model, I interpolate η_m over the range of JPA gains used in this experiment. In

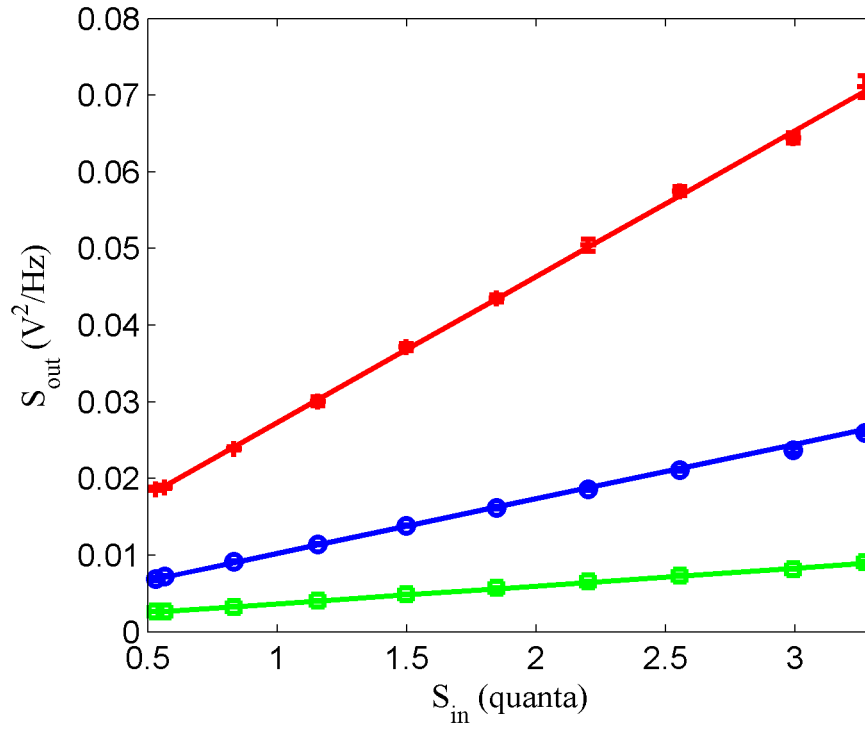


Figure 5.16: Thermal sweep data for the JPA operated at 20 (green squares), 25 (blue circles) and 30 dB (red crosses) gains. The data are fit to Eq. 5.24 (solid lines). The input noise source used in the thermal sweep is a 50Ω resistor whose temperature is adjusted from 79 mK to 900 mK. This thermal noise power is expressed in units of quanta at 5.8 GHz on the x-axis.

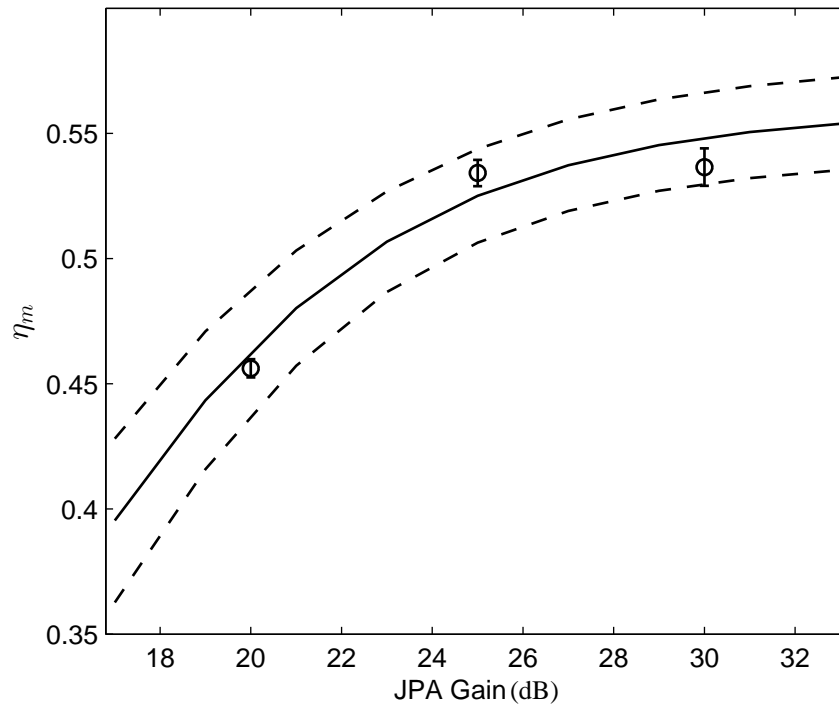


Figure 5.17: The measurement efficiency η_m is determined from a thermal sweep at three JPA gains (circles). This quantity is interpolated over the range of JPA gains by fitting the data points to Eqn. 5.27 with the uncertainty in dashed lines.

this model I assume that N_{JPA} and N_{HEMT} are both constant when referenced to their respective amplifier inputs. The output power spectral density is then

$$S_{out} = G(S_{in} + N_{\text{JPA}} + \frac{N_{\text{HEMT}}}{G_{\text{JPA}}}), \quad (5.26)$$

where G_{JPA} is the gain of the JPA. From Eqn. 5.26 the added noise can be written as

$$N_{add} = N_{\text{JPA}} + \frac{N_{\text{HEMT}}}{G_{\text{JPA}}}, \quad (5.27)$$

forming the model I use for interpolation [17]. The three added noises are fit according to Eqn. 5.27. I find $N_{\text{JPA}} = 0.39 \pm 0.03$ and $N_{\text{HEMT}} = 18 \pm 5$. Using these added noises, η_m is plotted over the range of JPA gains in Fig. 5.17 (solid line) according to Eqns. 5.25 and 5.27.

5.3.3.2 Measurement comparison

I form an expected density matrix ρ_{exp} by considering measurement efficiency and cavity loss. Following Section 2.3.5, my expectation for the density matrix I should measure for pure cavity photon generation is

$$\rho_{\text{exp}} = (1 - \frac{\kappa_{out}}{\kappa}\eta_m)|0\rangle\langle 0| + \frac{\kappa_{out}}{\kappa}\eta_m|1\rangle\langle 1|. \quad (5.28)$$

Finally, I compare my measurement to expectation by computing the fidelity¹ of ρ_m with respect to ρ_{exp} . I find that they are identical (unit fidelity) within uncertainty (Fig. 5.18). This agreement shows that I am able to accurately and independently characterize the measurement inefficiency and undesired cavity loss. (The measured two-photon component contributes negligibly to the infidelity.) For comparison, I compute the fidelity of the measured density matrix ρ_m with respect to the density matrix of a single photon (Fig. 5.18), which quantifies my combined ability to generate and detect single photons. This fidelity has a peak value of $\mathcal{F} = 0.600 \pm 0.008$ also at 29 dB JPA gain [78].

¹ The fidelity of a state A (ρ_A) with a state B (ρ_B) is $\mathcal{F} = \text{tr}(\sqrt{\sqrt{\rho_B}\rho_A\sqrt{\rho_B}})$.

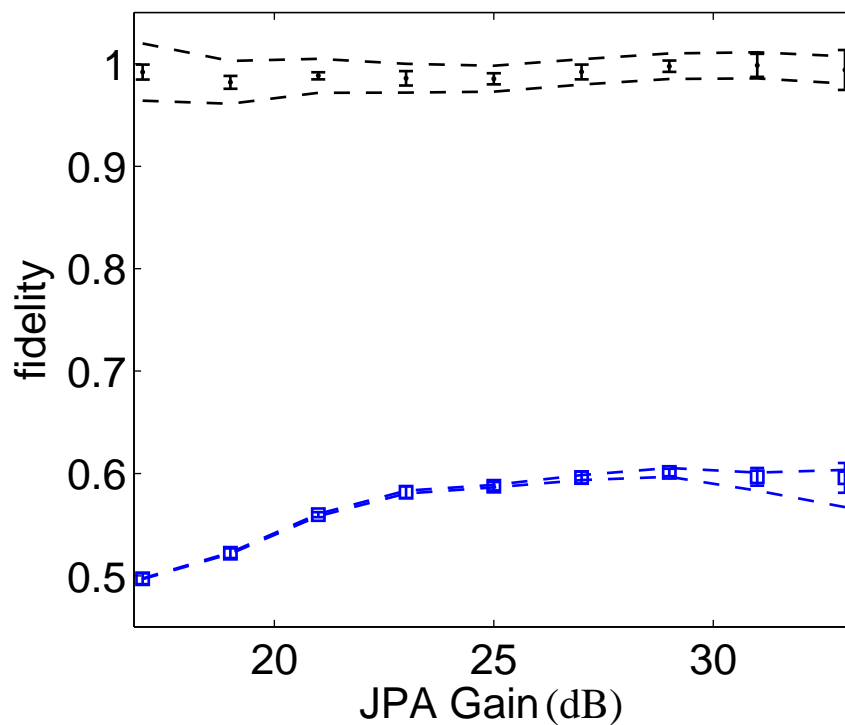


Figure 5.18: The fidelity of the measured density matrix with respect to: an ideal single photon (blue squares), and the density matrix I expect to measure given pure photon generation in the cavity (black points). Here, the statistical one-standard-deviation uncertainties are plotted as errors bars. The systematic error plotted in dashed lines is calculated from both the systematic uncertainty in η_m and in the density matrix elements.

Chapter 6

Conclusions and outlook

The protocol I have demonstrated for generating single microwave photons on demand is well suited for transferring quantum states to narrow bandwidth signal processing modules, such as certain types of electro-optic converters that are under development [20]. In particular, the compatibility of the protocol with fixed-frequency, highly coherent qubit-cavity systems ensures that the photons can be emitted into narrow frequency windows. I have characterized the photon source and its homodyne detection, and understand their imperfections. Because an ideal single photon source generates one single photon every time, and never generates two or more, the quality of the photon generation and detection can be quantified by the probability of measuring a single photon ρ_{11} (Fig. 5.14), and the probability of measuring two photons ρ_{22} , or by $g_2(0)$ (Fig. 5.15). I have independently characterized the system's measurement efficiency η_m and cavity loss $1 - \kappa_{out}/\kappa$ and find that they account for the measured photon state within uncertainty using state fidelity as the metric (Fig. 5.18). The non-unity measurement efficiency and non-zero cavity loss yield practical, but not fundamental limitations on ρ_{11} , and may be improved in future implementations of the single photon source.

These measurements highlight the compromise between backaction and measurement efficiency. My detailed characterization of the protocol reveals an undesirable backaction of the measurement apparatus onto both the qubit and the cavity. It is possible to reduce the backaction through the use of more commercial isolators (Fig. A.1), however, doing so increases the loss between the cavity and JPA. With advances in low loss isolator elements [79, 80], it may be possible

to mitigate this backaction through the use of more isolation while at the same time reducing losses in detection. Otherwise, a more complicated protocol that pulses on the JPA pumps only when the measurement is desired may minimize the backaction. Overall, the measurements presented here highlight the importance of isolator elements in quantum information processing, and provide a method to transfer information between qubit-cavity systems and itinerant microwave fields.

6.1 Outlook

There are two simple extensions of this single photon generation and detection experiment. First, one could use the qubit-cavity system to generate flying qubits or arbitrary combinations of $|0\rangle$ and $|1\rangle$. To form a flying qubit, the qubit state $A|g\rangle + B|e\rangle$ is mapped onto the propagating photon state $A|0\rangle + B|1\rangle$. Second, one could send the propagating photon state to mechanical module.

To generate a flying qubit from the system, one must employ a more complex protocol than just a single blue sideband pulse. For example, if one performed a $\pi/2$ -pulse with blue sideband, then the system would be prepared in the $\Psi = 1/\sqrt{2}(|g, 0\rangle + e^{i\phi}|e, 1\rangle)$. The photon is entangled with the qubit. As the photon decays to the output modes, this state could transmit entanglement, but does not behave like a flying qubit. If only the output mode were measured, then its reduced density matrix would be found by tracing over the qubit part of the full density matrix. (Section 2.3.5). The density matrix of the output would then be $\rho_{out} = 1/2(|0\rangle\langle 0| + |1\rangle\langle 1|)$, a maximally mixed state without any phase information.

One could implement a two step protocol to avoid this entanglement and generate a flying qubit. In the first step, the qubit state is defined. A qubit pulse prepares the qubit in the $\Psi_1 = A|g, 0\rangle + B|e, 0\rangle$ state. In the next step, a π -pulse on the blue sideband swaps the $|g, 0\rangle$ term to $|e, 1\rangle$, but leaves the $|e, 0\rangle$ unaffected. After the blue sideband π -pulse, the system is in the $\Psi_2 = A|e, 1\rangle + B|e, 0\rangle$ state. The photon then decays out as an unentangled, pure state. Because the qubit is in the $|e\rangle$ state in both terms, $|e\rangle$ can be factored out. The output state then looks like $\Psi_{out} = B|0\rangle + A|1\rangle$, a flying qubit with coefficients A and B swapped compared to the qubit state

in the first step. With this protocol, one could create a source of flying qubits to send to other qubit modules or measure directly with the JPA. However, care must be taken using a common phase reference for all pulses and any measurements.

After demonstrating the photon source (or potentially a flying qubit source), it could be used to prepare other modules, such as mechanical circuits, in nonclassical states. Through the use of coherent control tones, the state of a propagating, incident modes can be mapped onto the photon state of the a mechanical mode of the oscillator [16]. By sending a single photon into the mechanical module and using coherent control tones, a mode of the mechanics could be prepared in an $n = 1$ phonon state. Such a demonstration would be landmark achievement of quantum physics as it would prepare a macroscopic mechanical object in a profoundly nonclassical state.

Bibliography

- [1] J. Cirac and P. Zoller, “Quantum Computations with Cold Trapped Ions,” Physical Review Letters, vol. 74, pp. 4091–4094, May 1995.
- [2] C. Monroe, D. M. Meekhof, B. E. King, and D. J. Wineland, “A “Schrodinger Cat” Superposition State of an Atom,” Science, vol. 272, pp. 1131–1136, May 1996.
- [3] M. V. G. Dutt, L. Childress, L. Jiang, E. Togan, J. Maze, F. Jelezko, A. S. Zibrov, P. R. Hemmer, and M. D. Lukin, “Quantum register based on individual electronic and nuclear spin qubits in diamond.,” Science (New York, N.Y.), vol. 316, pp. 1312–6, June 2007.
- [4] D. Loss and D. P. DiVincenzo, “Quantum computation with quantum dots,” Physical Review A, vol. 57, pp. 120–126, Jan. 1998.
- [5] S. A. Wolf, D. D. Awschalom, R. A. Buhrman, J. M. Daughton, S. von Molnár, M. L. Roukes, A. Y. Chtchelkanova, and D. M. Treger, “Spintronics: a spin-based electronics vision for the future.,” Science (New York, N.Y.), vol. 294, pp. 1488–95, Nov. 2001.
- [6] A. Wallraff, D. I. Schuster, A. Blais, L. Frunzio, R.-S. Huang, J. Majer, S. Kumar, S. M. Girvin, and R. J. Schoelkopf, “Strong coupling of a single photon to a superconducting qubit using circuit quantum electrodynamics.,” Nature, vol. 431, pp. 162–167, Sept. 2004.
- [7] T. Niemczyk, F. Deppe, H. Huebl, E. P. Menzel, F. Hocke, M. J. Schwarz, J. J. Garcia-Ripoll, D. Zueco, T. Hümmer, E. Solano, A. Marx, and R. Gross, “Circuit quantum electrodynamics in the ultrastrong-coupling regime,” Nature Physics, vol. 6, pp. 772–776, July 2010.
- [8] B. Schumacher, “Quantum coding,” Phys. Rev. A, vol. 51, pp. 2738–2747, Apr. 1995.
- [9] M. Hofheinz, H. Wang, M. Ansmann, R. C. Bialczak, E. Lucero, M. Neeley, A. D. O’Connell, D. Sank, J. Wenner, J. M. Martinis, and A. N. Cleland, “Synthesizing arbitrary quantum states in a superconducting resonator,” Nature, vol. 459, pp. 546–549, 2009.
- [10] G. Kirchmair, B. Vlastakis, Z. Leghtas, S. Nigg, H. Paik, E. Ginossar, M. Mirrahimi, L. Frunzio, S. M. Girvin, and R. J. Schoelkopf, “Observation of quantum state collapse and revival due to the single-photon Kerr effect,” Nature, vol. 495, pp. 205–209, 2013.
- [11] H. J. Kimble, “The quantum internet,” Nature, vol. 453, pp. 1023–1030, 2008.
- [12] J. Majer, J. M. Chow, J. M. Gambetta, J. Koch, B. R. Johnson, J. A. Schreier, L. Frunzio, D. I. Schuster, A. A. Houck, A. Wallraff, A. Blais, M. H. Devoret, S. M. Girvin, and R. J. Schoelkopf, “Coupling superconducting qubits via a cavity bus.,” Nature, vol. 449, pp. 443–7, Sept. 2007.

- [13] L. Steffen, Y. Salathe, M. Oppliger, P. Kurpiers, M. Baur, C. Lang, C. Eichler, G. Puebla-Hellmann, A. Fedorov, and A. Wallraff, “Deterministic quantum teleportation with feed-forward in a solid state system,” Nature, vol. 500, no. 7462, p. 319, 2013.
- [14] N. Roch, M. E. Schwartz, F. Motzoi, C. Macklin, R. Vijay, A. W. Eddins, A. N. Korotkov, K. B. Whaley, M. Sarovar, and I. Siddiqi, “Observation of Measurement-Induced Entanglement and Quantum Trajectories of Remote Superconducting Qubits,” Phys. Rev. Lett., vol. 112, p. 170501, Apr. 2014.
- [15] J. D. Teufel, T. Donner, D. Li, J. W. Harlow, M. S. Allman, K. Cicak, a. J. Sirois, J. D. Whittaker, K. W. Lehnert, and R. W. Simmonds, “Sideband cooling of micromechanical motion to the quantum ground state.,” Nature, vol. 475, pp. 359–363, July 2011.
- [16] T. A. Palomaki, J. W. Harlow, J. D. Teufel, R. W. Simmonds, and K. W. Lehnert, “Coherent state transfer between itinerant microwave fields and a mechanical oscillator.,” Nature, vol. 495, pp. 210–214, Mar. 2013.
- [17] M. A. Castellanos-Beltran, K. D. Irwin, G. C. Hilton, L. R. Vale, and K. W. Lehnert, “Amplification and squeezing of quantum noise with a tunable Josephson metamaterial,” Nat. Phys., vol. 4, pp. 929–931, Oct. 2008.
- [18] H. Paik, D. I. Schuster, L. S. Bishop, G. Kirchmair, G. Catelani, a. P. Sears, B. R. Johnson, M. J. Reagor, L. Frunzio, L. I. Glazman, S. M. Girvin, M. H. Devoret, and R. J. Schoelkopf, “Observation of High Coherence in Josephson Junction Qubits Measured in a Three-Dimensional Circuit QED Architecture,” Phys. Rev. Lett., vol. 107, p. 240501, Dec. 2011.
- [19] R. W. Andrews, A. P. Reed, K. Cicak, J. D. Teufel, and K. W. Lehnert, “Quantum-enabled temporal and spectral mode conversion of microwave signals,” eprint arXiv:1506.02296, p. 15, June 2015.
- [20] R. W. Andrews, R. W. Peterson, T. P. Purdy, K. Cicak, R. W. Simmonds, C. A. Regal, and K. W. Lehnert, “Bidirectional and efficient conversion between microwave and optical light,” Nature Physics, vol. 10, no. 6159, pp. 321–326, 2014.
- [21] A. Blais, R.-S. Huang, A. Wallraff, S. M. Girvin, and R. J. Schoelkopf, “Cavity quantum electrodynamics for superconducting electrical circuits: An architecture for quantum computation,” Phys. Rev. A, vol. 69, p. 62320, June 2004.
- [22] A. Wallraff, D. I. Schuster, A. Blais, J. M. Gambetta, J. Schreier, L. Frunzio, M. H. Devoret, S. M. Girvin, and R. J. Schoelkopf, “Sideband Transitions and Two-Tone Spectroscopy of a Superconducting Qubit Strongly Coupled to an On-Chip Cavity,” Phys. Rev. Lett., vol. 99, p. 50501, July 2007.
- [23] P. J. Leek, S. Filipp, P. Maurer, M. Baur, R. Bianchetti, J. M. Fink, M. Göppl, L. Steffen, and A. Wallraff, “Using sideband transitions for two-qubit operations in superconducting circuits,” Phys. Rev. B, vol. 79, p. 180511(R), 2009.
- [24] B. Yurke, L. Corruccini, P. Kaminsky, L. Rupp, A. Smith, A. Silver, R. Simon, and E. Whittaker, “Observation of parametric amplification and deamplification in a Josephson parametric amplifier,” Phys. Rev. A, vol. 39, pp. 2519–2533, Mar. 1989.

- [25] A. A. Clerk, M. H. Devoret, S. M. Girvin, F. Marquardt, and R. J. Schoelkopf, “Introduction to quantum noise, measurement, and amplification,” Rev. Mod. Phys., vol. 82, pp. 1155–1208, Apr. 2010.
- [26] F. Mallet, M. A. Castellanos-Beltran, H. S. Ku, S. Glancy, E. Knill, K. D. Irwin, G. C. Hilton, L. R. Vale, and K. W. Lehnert, “Quantum State Tomography of an Itinerant Squeezed Microwave Field,” Phys. Rev. Lett., vol. 106, p. 220502, June 2011.
- [27] E. Flurin, N. Roch, F. Mallet, M. H. Devoret, and B. Huard, “Generating Entangled Microwave Radiation Over Two Transmission Lines,” Phys. Rev. Lett., vol. 109, p. 183901, Oct. 2012.
- [28] T. A. Palomaki, J. D. Teufel, R. W. Simmonds, and K. W. Lehnert, “Entangling mechanical motion with microwave fields,” Science, vol. 342, pp. 710–713, Nov. 2013.
- [29] H. S. Ku and Others, “Generating and verifying entangled itinerant microwave fields with efficient and independent measurements,” Phys. Rev. A, vol. 91, p. 42305, 2015.
- [30] B. Abdo, F. Schackert, M. Hatridge, C. Rigetti, and M. Devoret, “Josephson amplifier for qubit readout,” Appl. Phys. Lett., vol. 99, no. 16, p. 162506, 2011.
- [31] R. Vijay, D. H. Slichter, and I. Siddiqi, “Observation of Quantum Jumps in a Superconducting Artificial Atom,” Phys. Rev. Lett., vol. 106, p. 110502, 2011.
- [32] D. Ristè, C. C. Bultink, K. W. Lehnert, and L. DiCarlo, “Feedback Control of a Solid-State Qubit Using High-Fidelity Projective Measurement,” Phys. Rev. Lett., vol. 109, p. 240502, Dec. 2012.
- [33] M. D. Schroer, M. H. Kolodrubetz, W. F. Kindel, M. Sandberg, J. Gao, M. R. Vissers, D. P. Pappas, A. Polkovnikov, and K. W. Lehnert, “Measuring a Topological Transition in an Artificial Spin-1/2 System,” Phys. Rev. Lett., vol. 113, p. 50402, 2014.
- [34] N. Boulant, G. Ithier, P. Meeson, F. Nguyen, D. Vion, D. Esteve, I. Siddiqi, R. Vijay, C. Rigetti, F. Pierre, and M. Devoret, “Quantum nondemolition readout using a Josephson bifurcation amplifier,” Phys. Rev. B, vol. 76, p. 14525, July 2007.
- [35] K. W. Murch, S. J. Weber, C. Macklin, and I. Siddiqi, “Observing single quantum trajectories of a superconducting quantum bit,” Nature, vol. 502, pp. 211–214, Oct. 2013.
- [36] Y. Yin, Y. Chen, D. Sank, P. J. J. O’Malley, T. C. White, R. Barends, J. Kelly, E. Lucero, M. Mariantoni, A. Megrant, C. Neill, A. Vainsencher, J. Wenner, A. N. Korotkov, A. N. Cleland, and J. M. Martinis, “Catch and Release of Microwave Photon States,” Phys. Rev. Lett., vol. 110, p. 107001, 2013.
- [37] J. Wenner, Y. Yin, Y. Chen, R. Barends, B. Chiaro, E. Jeffrey, J. Kelly, A. Megrant, J. Y. Mutus, C. Neill, P. J. J. O’Malley, P. Roushan, D. Sank, A. Vainsencher, T. C. White, A. N. Korotkov, A. N. Cleland, and J. M. Martinis, “Catching Time-Reversed Microwave Coherent State Photons with 99.4% Absorption Efficiency,” Phys. Rev. Lett., vol. 112, p. 210501, May 2014.
- [38] A. A. Houck, D. I. Schuster, J. M. Gambetta, J. A. Schreier, B. R. Johnson, J. M. Chow, L. Frunzio, J. Majer, M. H. Devoret, S. M. Girvin, and R. J. Schoelkopf, “Generating single microwave photons in a circuit,” Nature, vol. 449, p. 328, 2007.

- [39] C. Eichler, D. Bozyigit, C. Lang, L. Steffen, J. Fink, and A. Wallraff, “Experimental State Tomography of Itinerant Single Microwave Photons,” Phys. Rev. Lett., vol. 106, p. 220503, June 2011.
- [40] J. J. Sanchez-Mondragon, N. B. Narozhny, and J. H. Eberly, “Theory of Spontaneous-Emission Line Shape in an Ideal Cavity,” Phys. Rev. Lett., vol. 51, pp. 550–553, Aug. 1983.
- [41] M. Pechal, L. Huthmacher, C. Eichler, S. Zeytino, A. A. Abdumalikov, S. Berger, A. Wallraff, and S. Filipp, “Microwave-Controlled Generation of Shaped Single Photons in Circuit Quantum Electrodynamics,” Phys. Rev. X, vol. 4, p. 41010, Oct. 2014.
- [42] C. Gerry and P. Knight, Introductory Quantum Optics. Cambridge University Press, 2005.
- [43] C. Gardiner and M. Collett, “Input and output in damped quantum systems: Quantum stochastic differential equations and the master equation,” Phys. Rev. A, vol. 31, pp. 3761–3774, June 1985.
- [44] D. I. Schuster, Circuit Quantum Electrodynamics. PhD thesis, Yale University, 2007.
- [45] A. Blais, J. Gambetta, A. Wallraff, D. I. Schuster, S. M. Girvin, M. H. Devoret, and R. J. Schoelkopf, “Quantum-information processing with circuit quantum electrodynamics,” Phys. Rev. A, vol. 75, p. 32329, 2009.
- [46] T. V. Duzer and C. W. Turner, Principles of Superconductive Devices and Circuits. Prentice Hall, 1999.
- [47] M. H. Devoret, A. Wallraff, and J. M. Martinis, “Superconducting Qubits: A Short Review,” eprint arXiv:cond-mat/0411174, Nov. 2004.
- [48] J. M. Martinis, M. H. Devoret, and J. Clarke, “Energy-Level Quantization in the Zero-Voltage State of a Current-Biased Josephson Junction,” Phys. Rev. Lett., vol. 55, pp. 1543–1546, Oct. 1985.
- [49] E. Il’ichev, N. Oukhanski, A. Izmalkov, T. Wagner, M. Grajcar, H.-G. Meyer, A. Y. Smirnov, A. van den Brink, M. H. S. Amin, and A. M. Zagoskin, “Continuous Monitoring of Rabi Oscillations in a Josephson Flux Qubit,” Phys. Rev. Lett., vol. 91, p. 97906, Aug. 2003.
- [50] J. Clarke and F. K. Wilhelm, “Superconducting quantum bits.,” Nature, vol. 453, pp. 1031–42, June 2008.
- [51] B. Josephson, “The discovery of tunnelling supercurrents,” Rev. Mod. Phys., vol. 46, pp. 251–254, Apr. 1974.
- [52] V. Bouchiat, D. Vion, P. Joyez, D. Esteve, and M. H. Devoret, “Quantum Coherence with a Single Cooper Pair,” Physica Scripta, vol. T76, no. 1, p. 165, 1998.
- [53] D. P. Divincenzo, “The Physical Implementation of Quantum Computation,” Fortschritte der Physik, vol. 48, pp. 771–783, 2000.
- [54] R. Schutjens, F. A. Dagg, D. J. Egger, and F. K. Wilhelm, “Single-qubit gates in frequency-crowded transmon systems,” Phys. Rev. A, vol. 88, p. 52330, Nov. 2013.

- [55] Y. Nakamura, Y. A. Pashkin, and J. S. Tsai, “Coherent control of macroscopic quantum states in a single-Cooper-pair box,” vol. 398, pp. 786–788, Apr. 1999.
- [56] B. S. Palmer and Others, “Steady-state thermodynamics of nonequilibrium quasiparticles in a Cooper-pair box,” Phys. Rev. B, vol. 76, p. 54501, 2007.
- [57] J. Koch, T. M. Yu, J. Gambetta, A. A. Houck, D. I. Schuster, J. Majer, A. Blais, M. H. Devoret, S. M. Girvin, and R. J. Schoelkopf, “Charge-insensitive qubit design derived from the Cooper pair box,” Phys. Rev. A, vol. 76, p. 42319, 2007.
- [58] J. A. Schreier and Others, “Suppressing charge noise decoherence in superconducting charge qubits,” Phys. Rev. B, vol. 77, p. 180502(R), 2008.
- [59] J. B. Chang, M. R. Vissers, A. D. Corcoles, M. Sandberg, J. Gao, D. W. Abraham, J. M. Chow, J. M. Gambetta, M. Beth Rothwell, G. A. Keefe, M. Steffen, and D. P. Pappas, “Improved superconducting qubit coherence using titanium nitride,” Applied Physics Letters, vol. 103, p. 012602, July 2013.
- [60] I. Siddiqi, R. Vijay, M. Metcalfe, E. Boaknin, L. Frunzio, R. J. Schoelkopf, and M. H. Devoret, “Dispersive measurements of superconducting qubit coherence with a fast latching readout,” Physical Review B, vol. 73, p. 054510, Feb. 2006.
- [61] R. Bianchetti, S. Filipp, M. Baur, J. M. Fink, M. Göppl, P. J. Leek, L. Steffen, A. Blais, and A. Wallraff, “Dynamics of dispersive single-qubit readout in circuit quantum electrodynamics,” Physical Review A, vol. 80, p. 043840, Oct. 2009.
- [62] A. Wallraff, D. I. Schuster, A. Blais, L. Frunzio, J. Majer, M. H. Devoret, S. M. Girvin, and R. J. Schoelkopf, “Approaching Unit Visibility for Control of a Superconducting Qubit with Dispersive Readout,” Phys. Rev. Lett., vol. 95, p. 60501, Aug. 2005.
- [63] R. Vijay, C. Macklin, D. H. Slichter, S. J. Weber, K. W. Murch, R. Naik, a. N. Korotkov, and I. Siddiqi, “Stabilizing Rabi oscillations in a superconducting qubit using quantum feedback.,” Nature, vol. 490, pp. 77–80, Oct. 2012.
- [64] M. D. Reed, L. DiCarlo, B. R. Johnson, L. Sun, D. I. Schuster, L. Frunzio, and R. J. Schoelkopf, “High-Fidelity Readout in Circuit Quantum Electrodynamics Using the Jaynes-Cummings Nonlinearity,” Physical Review Letters, vol. 105, p. 173601, Oct. 2010.
- [65] O. Astafiev, Y. A. Pashkin, T. Yamamoto, Y. Nakamura, and J. S. Tsai, “Single-shot measurement of the Josephson charge qubit,” Physical Review B, vol. 69, p. 180507, May 2004.
- [66] F. Mallet, F. R. Ong, A. Palacios-Laloy, F. Nguyen, P. Bertet, D. Vion, and D. Esteve, “Single-shot qubit readout in circuit quantum electrodynamics,” Nat. Phys., vol. 5, pp. 791–795, Sept. 2009.
- [67] K. Geerlings, Z. Leghtas, I. M. Pop, S. Shankar, L. Frunzio, R. J. Schoelkopf, M. Mirrahimi, and M. H. Devoret, “Demonstrating a Driven Reset Protocol for a Superconducting Qubit,” Physical Review Letters, vol. 110, p. 120501, Mar. 2013.
- [68] D. Vion, A. Aassime, A. Cottet, P. Joyez, H. Pothier, C. Urbina, D. Esteve, and M. H. Devoret, “Rabi oscillations, Ramsey fringes and spin echoes in an electrical circuit,” Fortschritte der Physik, vol. 51, no. 4-5, pp. 462–468, 2003.

- [69] D. I. Schuster, A. A. Houck, J. A. Schreier, A. Wallraff, J. M. Gambetta, A. Blais, L. Frunzio, J. Majer, B. Johnson, M. H. Devoret, S. M. Girvin, and R. J. Schoelkopf, “Resolving photon number states in a superconducting circuit.,” Nature, vol. 445, pp. 515–8, Feb. 2007.
- [70] H. Wang, M. Hofheinz, M. Ansmann, R. C. Bialczak, E. Lucero, M. Neeley, A. D. O’Connell, D. Sank, J. Wenner, A. N. Cleland, and J. M. Martinis, “Measurement of the Decay of Fock States in a Superconducting Quantum Circuit,” Phys. Rev. Lett., vol. 101, p. 240401, Dec. 2008.
- [71] J. Gambetta, A. Blais, D. I. Schuster, A. Wallraff, L. Frunzio, J. Majer, M. H. Devoret, S. M. Girvin, and R. J. Schoelkopf, “Qubit-photon interactions in a cavity: Measurement-induced dephasing and number splitting,” Physical Review A, vol. 74, p. 042318, Oct. 2006.
- [72] J. E. Johnson, C. Macklin, D. H. Slichter, R. Vijay, E. B. Weingarten, J. Clarke, and I. Siddiqi, “Heralded State Preparation in a Superconducting Qubit,” Phys. Rev. Lett., vol. 109, p. 50506, Aug. 2012.
- [73] C. Eichler, Experimental Characterization of Quantum Microwave Radiation and its Entanglement with a Superconducting Qubit. PhD thesis, ETH Zurich, 2013.
- [74] B. P. Gibbs, Advanced Kalman Filtering, Least-Squares and Modeling: A Practical Handbook. John Wiley and Sons, 2011.
- [75] K. W. Murch, S. J. Weber, K. M. Beck, E. Ginossar, and I. Siddiqi, “Reduction of the radiative decay of atomic coherence in squeezed vacuum.,” Nature, vol. 499, pp. 62–5, July 2013.
- [76] A. P. Sears, A. Petrenko, G. Catelani, L. Sun, H. Paik, G. Kirchmair, L. Frunzio, L. I. Glazman, S. M. Girvin, and R. J. Schoelkopf, “Photon shot noise dephasing in the strong-dispersive limit of circuit QED,” Phys. Rev. B, vol. 86, p. 80504(R), 2012.
- [77] U. Leonhardt and H. Paul, “High-Accuracy Optical Homodyne Detection with Low-Efficiency Detectors: ”Preamplification” from Antisqueezeing,” Phys. Rev. Lett., vol. 72, pp. 4086–4089, June 1994.
- [78] W. F. Kindel, M. D. Schroer, and K. W. Lehnert, “Generation and efficient measurement of single photons from fixed frequency superconducting qubits,” eprint arXiv:1510.00663, p. 9, Oct. 2015.
- [79] J. Kerckhoff, K. Lalumière, B. J. Chapman, A. Blais, and K. Lehnert, “On-Chip Superconducting Microwave Circulator from Synthetic Rotation,” Physical Review Applied, vol. 4, p. 034002, Sept. 2015.
- [80] K. M. Sliwa, M. Hatridge, A. Narla, S. Shankar, L. Frunzio, R. J. Schoelkopf, and M. H. Devoret, “Reconfigurable Josephson Circulator/Directional Amplifier,” Physical Review X, vol. 5, p. 041020, Nov. 2015.

Appendix A

Description of photon generation and homodyne detection apparatus

The experimental details for the optimized photon generation and homodyne detection (Section 5.3) are summarized by the microwave schematic (Fig. A.1). The experiment is conducted in an Oxford Triton 200 dilution refrigerator with the qubit-cavity system anchored to the ($T < 25$ mK) base temperature region. The qubit-cavity system is controlled and measured via injecting tones shown on the left. The strongly coupled output on the right leads to a switch, which either connects the qubit-cavity system or the thermal load to the measurement chain.

After the switch, circulators route signals into the JPA. The JPA is a nonlinear lumped element LC resonator pumped by rf power injected using a 20 dB directional coupler. It is operated with a signal gain from 17 to 33 dB and with an approximate gain bandwidth product of 43 MHz. The JPA is pumped with two tones in the so called double pump method by modulating a 5.806 GHz carrier by 240 MHz using an IQ mixer. The carrier is suppressed by the modulation and is further reduced by a notch cavity filter. The output of the JPA is routed into a HEMT amplifier and room temperature amplifiers before being mixed down by a second IQ mixer. A copy of the JPA carrier is used as this mixer's local oscillator and phase shifted so that the JPA's amplified quadrature exits the I-port of the mixer. This output is then further amplified and then digitized. An arbitrary waveform generator determines the protocol timing by triggering the drive tone, the measurement's tone, and the digitizer.

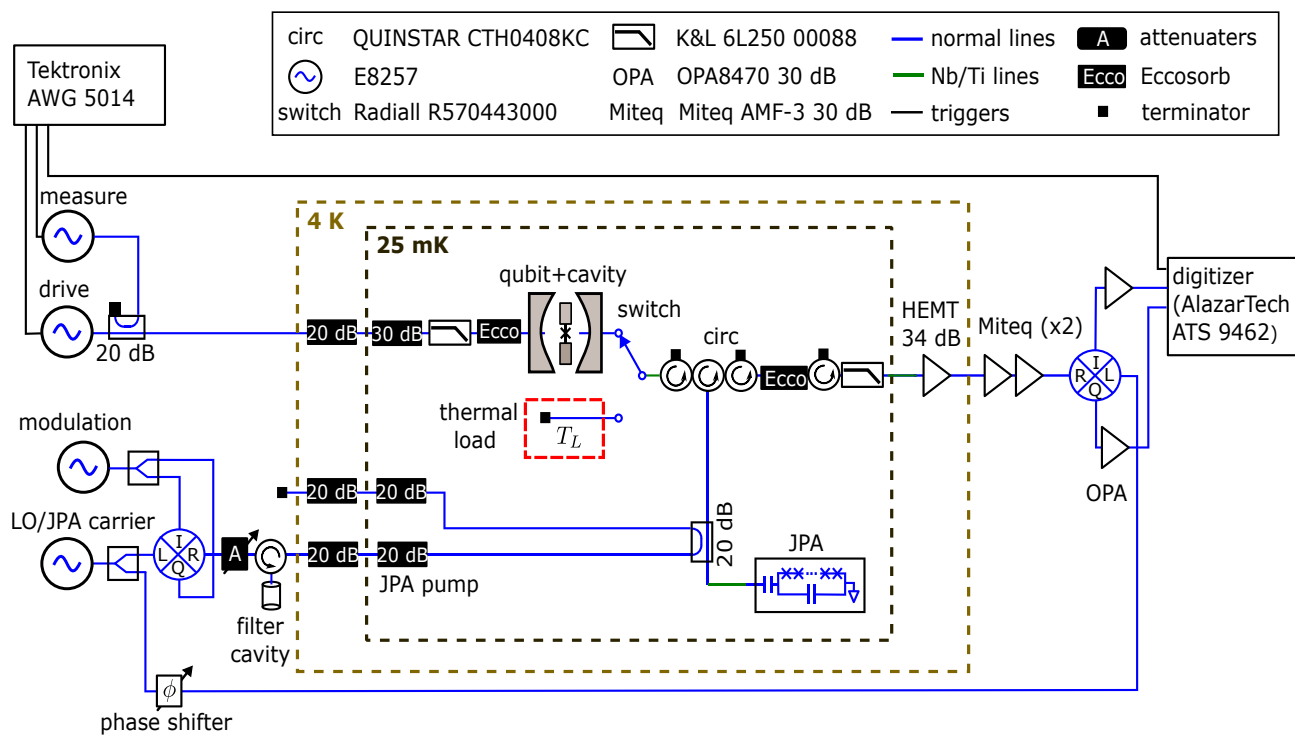


Figure A.1: The microwave schematic for the experiment.